VICTORIA
UNIVERSITY
OF TECHNOLOGY

# Atomic Beam Techniques in a

# Rubidium Vapour Cell

by

## Christopher John Vale

Submitted for the degree of

## Doctor of Philosophy

School of Communications and Informatics

Victoria University of Technology

Australia

For John, Ira, Stacey and Irena

# ABSTRACT

## Atomic Beam Techniques in a Rubidium Vapour Cell

by Christopher John Vale

Principal Supervisor:

*Dr. Peter Farrell*

This thesis presents a study on the realisation of a usable rubidium atomic beam inside a sealed vapour cell. A velocity selective optical pumping scheme was implemented to enable the detection of atoms of a particular velocity class travelling between two separated laser beams. This represents a new spectroscopic technique, the usefulness of which has been demonstrated through its applications. In the present work, the vapour cell atomic beam has been used to measure Larmor precession of polarised atoms in a magnetic field and one-dimensional laser cooling.

To perform the experiments it was necessary to construct lasers suitable for the measurements. To this end two types of external cavity diode laser were constructed and locked to features of the rubidium $D_2$ line. Once locked the lasers were seen to have short term linewidths of less than $1\,MHz$ and long term stability to within $2\,MHz$.

These lasers then formed an important part of the optical pumping scheme used to create the vapour cell atomic beam. One laser was used to label a particular velocity group of atoms while the other detected labelled atoms in another position in the cell. By modulating the labelling, and detecting with a lock-in amplifier, atomic beams with transverse velocity widths of $6\,m/s$ were clearly observed in both $^{85}Rb$ and $^{87}Rb$.

The first measurement performed with this scheme was the observation of Larmor precession of free atoms in a magnetic field. One laser was used to produce an ensemble of polarised atoms and the second laser measured the polarisation state of

the atoms at various distances from the first laser. Scans showed a dependence on the applied magnetic field and beam separation which followed the expected trends.

A second application for the vapour cell atomic beam technique was the measurement of laser cooling. Atoms were cooled (and heated) before entering the labelling and detection lasers resulting in a significant increase (decrease) in the number of atoms in the zero transverse velocity group. A detailed theoretical model of the laser cooling scheme was developed and the predictions of this agreed well with the experimental results for the cooling laser intensities and detunings used. The model also provided a means to separate the effects of optical pumping from true laser cooling.

I, Christopher John Vale, declare that the thesis entitled

**"Atomic beam techniques in a rubidium vapour cell"**

is my own original work, except where specific reference to other authors has been made, and has not been submitted previously, in whole or part, in respect of any other academic award.

Signature ███████████████████
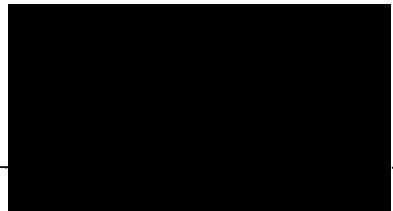
Date _____20/4/2000_____

# ACKNOWLEDGMENTS

In the course of my studies I have been very fortunate to receive assistance and support from many people to whom I would like to express my thanks.

Firstly, I would like to thank my supervisor Peter Farrell for his ideas and intuition which formed the foundations of this work (he's not a bad bloke either). I also wish to thank Robert Scholten for his hospitality and generosity in the Atom Optics laboratory at the University of Melbourne. Many thanks also to Mirek Walkiewicz for help with much of the work described in this thesis and for the loan of a laser.

I would also like to thank the technical staff of the Optical Technology Research Laboratory of Victoria University. In particular, Mark Kivenen and Donald Ermel for their excellent mechanical work on components for the laser systems and Alex Shelamoff for his infallible assistance with many of the electronic circuits constructed for the lasers.

During my postgraduate studies I have made many friends whom have assisted in instances too numerous to mention both in and often out of the lab. I would especially like to thank Scott Wade, Ian Mitchell, Darol Garchev, Mikhail Vasiliev and Greg Baxter for their friendship and support over a number of years. More generally, I would like to thank all of the members of the Optical Technology Research Laboratory of Victoria University and Optics Group of the University of Melbourne for making my postgraduate years most enjoyable.

Finally, I would like to thank those who have endured me at my worst over the last few years (don't all put your hands up). My parents Ira and John Vale and my girlfriend Stacey Williams. Sincerest love and thanks.

# CONTENTS

# LIST OF FIGURES

# Chapter 1

# INTRODUCTION

Atomic beams are extremely useful for performing many types of high resolution atomic physics experiments [1, 2]. An atomic beam is simply a stream of atoms travelling in a well defined direction. The atoms originate from a source, usually an oven, which has a small aperture through which the atoms escape. Typically a second aperture, at some distance downstream, allows only those atoms travelling in the required direction to pass through into a vacuum chamber, forming a collimated beam in the chamber.

Atomic beams have successfully been used to study many interesting physical phenomena. These include atomic collisions, high resolution spectroscopy, atomic clocks, and laser cooling [1]. Two of the most attractive features of atomic beams are their high flux and high degree of collimation. For experiments with alkali metals, beam sources usually consist of an oven operated at high temperature (eg. 200°C for rubidium ovens) so that the vapour pressure inside the oven will also be high, resulting in a high density of atoms in the beam. This feature means that high signal to noise ratios can be achieved in atomic beam experiments.

Additionally, the degree of collimation of an atomic beam can be defined by the size and position of the apertures. With small apertures (with diameters of $\approx 1\,\mathrm{mm}$) separated by a large distance (of order $1\,\mathrm{m}$), very high degrees of collimation can be obtained and the spread of velocities in one or two dimensions becomes very narrow. Probing the atomic beam with laser light perpendicular to the beam enables the Doppler broadening to be minimised, as the atoms are all travelling with a very small velocity component in the direction of laser propagation (often less than the

1

natural linewidths of transitions being probed). Thus atomic beams are highly useful when performing experiments which require sub-Doppler resolution.

There are, however, many problems and difficulties associated with operating and maintaining an atomic beam system. Firstly, high to ultra-high vacuum conditions are required, as the chamber through which the beam flows should contain a negligible amount of background gas ensuring that the beam will not be significantly affected by collisions with other atoms or molecules. Thus a high vacuum enclosure, equipped with high vacuum pumps, are a necessity. Secondly, an *in vacuo* beam source (oven) is required to heat heat a reservoir containing the atoms which form the beam. Realising such an oven in high vacuum can be a difficult task [3]. A final disadvantage is that the high vacuum requirements make the atomic beam system bulky and weighty, generally confining them to a well equipped laboratory setting.

Laser-atom interactions can also be studied in atomic vapour cells, which provide a for more user-friendly alternative. An atomic vapour cell is simply a sealed and evacuated glass container, which contains a low pressure background gas of a particular element. After manufacture, vapour cells do not require any high vacuum equipment for maintenance or operation and they are small and easily transportable. It is also possible to introduce elements (e.g. electric field plates) into a vapour cell at the time of manufacture to increase their versatility (see for example Macgillivray *et al.* [4]). Vapour cells are considerably cheaper to purchase and for more quickly applied than an atomic beam system. Thus, wherever possible, it is desirable to use vapour cells instead of atomic beams.

The main disadvantage of performing experiments in a vapour cell is that atoms inside the cell are moving in all directions, according to the Maxwellian velocity distribution [5]. This introduces considerable Doppler broadening to observed spectra as the velocity distribution is typically much broader than the natural linewidth of the transitions being investigated (approximately two orders of magnitude for rubidium at room temperature). Whilst the techniques of saturated absorption [1] and polarisation spectroscopy [6] overcome the Doppler broadening limitations, they do

not allow one to study the time evolution or projection of atoms within the cell as can be done with an atomic beam.

In this thesis, a technique is developed which allows one to study certain physical phenomena, which have previously required an atomic beam, within a sealed glass vapour cell. This is achieved by passing two spatially separated laser beams, co-propagating parallel to each other, through a cell, and detecting atoms which travel from one laser beam to the other. One laser is used to apply a signature or label to the desired velocity group of atoms, and the other selectively detects the labelled atoms. Generally, this will be atoms travelling at right angles to, and in the plane of, both laser beams, forming a parallel atomic beam.

To achieve this, a velocity selective optical pumping scheme was employed. This scheme enabled us to label only those atoms travelling with a specific velocity relative to the direction of laser propagation. A similar velocity selective detection technique was used to detect the labelled atoms.

This study was performed using rubidium, a group I element of the periodic table. There were several reasons for doing this. Firstly, optical transitions in rubidium are easily accessible by commonly available diode lasers. Rubidium also has an energy level structure which allows a simple optical pumping scheme to be employed for the labelling and detection. Additionally, rubidium has only one outer shell electron, making it similar in nature to hydrogen, so its behaviour is relatively well understood theoretically.

The following chapters describe in detail how the vapour cell atomic beam (VCAB) was realised and illustrate the usefulness of this technique. To perform the experiments, suitable lasers were required for the labelling and detection of the atoms. External cavity diode lasers were chosen as these had been reported to provide the desired operating characteristics [7, 8]. The design, construction, characterisation and frequency stabilisation of these lasers is described in chapter 2.

In chapter 3, a detailed account of the concept of the VCAB, and the techniques used to realise it in rubidium, is provided. Several authors have reported similar

schemes and the method described here incorporates some of these ideas. An analysis of the properties and limitations of the VCAB is also given.

The remaining chapters describe and study the implementation of the vapour cell atomic beam in experiments which have generally required a conventional atomic beam. The VCAB scheme was used to measure the Larmor precession of free atoms in a magnetic field (chapter 4). Chapter 5 illustrates experimentally how the VCAB was used to study one-dimensional laser cooling, in a similar way to cooling of real atomic beams. In chapter 6, a theoretical model of the laser cooling experiment is developed and compared to the experimental findings. The concluding chapter summarises and discusses the main findings and discusses some possibilities for extending the work and improving on the techniques.

# Chapter 2

# LASER DIODES

In order to perform the vapour cell atomic beam experiments we required lasers with narrow linewidth, a good frequency tuning range, good long term frequency stability and output powers up to tens of milliWatts. External cavity laser diodes (ECLD) were chosen as they possess the above features and can be constructed from relatively cheap and simple components. Additionally, laser diodes are available at wavelengths suitable for probing the rubidium $D_2$ transition at 780 nm which is the transition used in the experimental work.

In this chapter, a review of some of the important developments in laser diode technology and the impact these have had on atomic physics research is provided. A description of the basic principles of operation of external cavity lasers which use grating feedback follows. The ECLDs designed and constructed in the present work are then discussed in some detail. The lasers were used for saturated absorption measurements of the hyperfine transitions of the rubidium $D_2$ line. Finally, the lasers were locked using two techniques and their stability and linewidth characteristics studied to ensure they could operate reliably at the frequencies required for later experiments.

## 2.1   Introduction and review

Laser diodes are small semiconductor devices capable of producing laser output at a variety of wavelengths. They are found in many everyday devices such as compact disc players, barcode readers, printers and laser pointers. The laser itself is a small chip consisting of several layers of semiconductor material, for example AlGaAs.

5

Laser light is generated by sending an electrical current through an active region, within the semiconductor chip, which is located between $n$-type and $p$-type cladding layers. Electrons and holes are produced which recombine in the active region, resulting in the emission of photons. The front and end faces of the chip define the laser cavity and these are typically around 250 $\mu$m apart. Diodes are usually housed in metal cans with an antireflection coated output window. The cans are typically several millimetres in diameter and similar in length making them very compact and practical devices.

During the past two decades, laser diodes have revolutionised experimental atomic physics. They are low cost, easy to use, available at a range of wavelengths, have narrow linewidth and good stability making them preferable to dye and titanium-sapphire lasers in many applications. Two excellent reviews by Camparo, 1985 [9] and Wieman and Hollberg, 1991 [8] cover in detail the history and major developments of laser diodes and their various applications to atomic physics. Much of the following paragraphs is a brief synopsis of these extensive reviews.

The first application of laser diodes in atomic physics took place in 1968 by Bölger and Diels [10] who used a GaAs diode, cooled to liquid nitrogen temperature, to observe multiple photon echoes in caesium. The first real spectroscopic measurements using laser diodes was reported in 1969 by Siahatgar and Hochuli [11] and Hochuli, Halderman and Siahatgar [12]. In both of these experiments, a GaAs diode operating at 77 K was used to probe the caesium $D_2$ transition at 852 nm. A current pulse, with a duration of the order of several microseconds, was used to sweep the laser frequency across the atomic transition in both an atomic vapour [11] and an atomic beam [12].

Further diode laser spectroscopic studies followed on the noble gases with Pine *et al.* measuring the absorption spectrum of the 6s-6p transition in xenon [13]. A pressure tuned GaAs diode was used and the hyperfine structure and influence of other isotopes were resolved. However, diodes at this stage were still quite awkward to operate as they could only be used at liquid nitrogen temperature.

The advent of room temperature InGaAsP and AlGaAs diodes drastically increased the usefulness of laser diodes. In 1983, Camparo and Klimcak used a room temperature continuous wave (c.w.) AlGaAs diode to measure the hyperfine structure of the rubidium $D_1$ line [14]. The laser wavelength was controlled and scanned by combined adjustment of the operating current and temperature. The fluorescence spectra of the $D_1$ line was recorded as the laser was scanned across the transition. Using a simple atomic beam they were able to resolve each of the hyperfine transitions and measure an isotope shift of 81 MHz with an uncertainty of $\pm 5.0$ MHz. This highlighted how easy it was becoming to perform high resolution laser spectroscopy using relatively simple and cheap apparatus.

By the mid 80s, laser diodes were becoming widespread in atomic physics. A summary of the various elements studied by this time, using diode laser spectroscopy, can be found in [9]. The spectral characteristics of laser diodes however, were not yet fully optimised. The linewidths of the diodes used in these experiments were of the order of 10 to 100 MHz, substantially broader than the majority of spectral features being studied which are typically of the order of several MHz.

The solution to this problem came with the development of external cavity laser diodes [8]. The principle of operation of ECLDs is described in some detail in section 2.2. Briefly though, an external cavity laser diode uses feedback from an external wavelength selective element to control the lasing frequency of the diode. The advancements brought about by using laser diodes in the external cavity configuration are significant. A drop in the linewidth from tens of MHz down to below 1 MHz meant that lasers were now spectrally narrower than nearly all of the features they were used to investigate. Thus, the laser was no longer the limiting factor to experimental resolution. In addition, tuning a laser with external feedback provides an alternative to tuning with the injection current or operating temperature, making the laser more versatile.

It has since been shown that ECLDs can be constructed in a variety of ways using relatively simple and inexpensive means, see for example [7, 15, 16, 17, 18, 19].

ECLDs are now used in a plethora of different applications ranging from basic spectroscopy to laser cooling and trapping. Some examples of more recent applications which are relevant to the vapour cell atomic beam concept are mentioned below.

High resolution spectroscopy of alkali elements using ECLDs is a popular and well established field of research. As an example of this type of work Bowie *et al.* [20] and Lee *et al.*[21] performed saturated absorption spectroscopy, with external cavity laser diodes, to study the Zeeman effect in rubidium. In both cases, various magnetic fields were applied to the Rb vapour and saturated absorption spectra were recorded. The resolution of their systems enabled them to observe Zeeman energy level shifts in fields as low as 1 mT.

Atomic clocks have also been the beneficiary of ECLD technology. In 1991, Monroe *et al.* use light from laser diodes to cool caesium atoms and use these cooled atoms to observe the atomic clock transition [22]. They also discuss the possibility of using an atomic fountain of cooled atoms to improve the accuracy of the clock. This has since been demonstrated by Clairon *et al.* and is currently being used to create the most accurate atomic clocks to date [23].

More recently, the field of laser cooling has gained considerable attention and many experiments have used external cavity laser diodes to cool and trap a variety of atoms, see for example [24, 25, 26]. They are now a standard component of most laser cooling experiments in which the cooling transition is accessible by a laser diode. One of the most notable achievements in this area was the realisation of Bose-Einstein condensation in rubidium in 1995 by the JILA group [27].

It is expected that, with the current world-wide interest in using laser diodes in atomic physics, new developments and innovations, in both the technology and applications of laser diodes, will continue well into the future.

## 2.2   External Cavity Diode Lasers

It has already been noted that free running laser diodes are usually not stable enough or sufficiently narrow in linewidth to perform high resolution spectroscopy. There are however, some simple measures which can be employed to narrow the linewidth and stabilise the frequency to a level which makes them far more useful. With the addition of an external cavity and precision temperature control and current supply, laser diodes can be forced to operate single mode with very narrow linewidth ($< 1\,$MHz). The frequency of the diode can be scanned precisely over a large fraction of its gain bandwidth by relatively simple adjustments of the cavity alignment, operating temperature or injection current. Because of this, the most common use of diode lasers in atomic physics is in the external cavity configuration.

External cavities take advantage of the fact that laser diodes are highly sensitive to optical feedback. An external wavelength selective element is used to provide optical feedback to the diode and control its operating wavelength. Typically, a diffraction grating [8] and/or Fabry Perot cavity [28] are used as the external element(s), and it has also been shown [29] that simpler reflective elements can be used. Additionally, laser diodes generally require a precision current supply and temperature control system to ensure stable single mode operation.

The usable gain bandwidth of laser diodes is typically of the order of 20 nm centred around the nominal operating wavelength. (This number, 20 nm, is accurate for 780 nm laser diodes. Diodes which operate at other wavelengths, for example 1550 nm, can have gain bandwidths of up to 100 nm). A free running diode will preferably operate very close to its centre wavelength. However, using the feedback from a diffraction grating, it is relatively easy to force the laser to operate single mode, over its entire gain bandwidth, with minor adjustments to the grating angle.
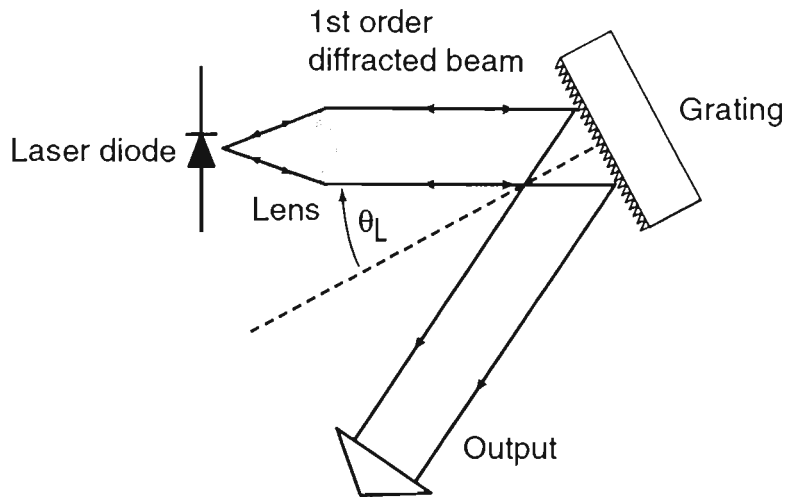
**Figure 2.1**: Schematic diagram of a Littrow configuration external cavity laser diode. Light from the laser is collimated and then incident on a diffraction grating oriented at the Littrow angle, $\theta_L$. Part of the light is diffracted back into the diode and part of it is reflected out. The feedback controls the wavelength of the laser.

## 2.2.1 The Littrow configuration

The simplest design for an ECLD which utilises feedback from a diffraction grating is the Littrow configuration. Figure 2.1 shows a schematic of this arrangement. Light from a laser diode is collimated and directed onto a diffraction grating, oriented at the Littrow angle, $\theta_L$, to the normal to the grating surface, given by:

$$\sin \theta_L = \frac{\lambda}{2d} \tag{2.1}$$

where, $\lambda$ is the wavelength of the light, and $d$ is the distance between rulings on the grating. In this configuration, the first order diffracted beam is sent back along the same path as the incident beam and refocussed into the laser diode. The zeroth order specular reflection off the grating forms the output of the external cavity. Optical feedback into the diode forces it to operate at the wavelength of the feedback. Small adjustments of the grating angle, with respect to the incident beam, alter the wavelength which is diffracted back into the diode, according to 2.1. The laser cavity is defined by the back of the diode facet (end mirror) and the diffraction grating (output coupler). However, to some extent, the allowable diode facet modes (defined

by the length of the diode chip) also determine the wavelengths at which lasing will be allowed.

Despite its simplicity there are some problems with the Littrow design. As the angle of the grating is changed, the direction of the output beam also shifts. This can lead to problems as the alignment of the output into an experiment will change if it is required to shift the wavelength. Additionally, unless the axis about which the grating angle rotates is positioned in precisely the right location [30], there will be regular mode hops as the laser frequency is scanned. This is due to the number of wavelengths, $N$, in the laser cavity changing. As the grating angle is changed, the cavity length should also change in such a way to keep $N$ constant. To achieve this with the Littrow configuration a bulky and more awkward design is required.

## 2.2.2 Littman-Metcalf configuration

A design which has overcome these problems is the Littman-Metcalf external cavity configuration (figure 2.2). In this arrangement, the angle between the laser and diffraction grating remains fixed. The first order diffracted beam is directed onto a mirror, mounted on a rotating arm. As the arm rotates about the pivot point, the wavelength of the light which travels the complete cavity path (ie. laser diode, diffraction grating, mirror, diffraction grating and back into the diode) changes accordingly.

There are four main advantages of this design, the first being that the direction of the output beam is fixed as both the grating and laser diode do not move. Another feature is that the wavelength selectivity is more precise as the grating is now oriented close to grazing incidence, meaning that more lines are illuminated. Also, one complete path around the cavity involves diffraction from the grating twice which leads to better wavelength selectivity. Finally, by appropriately positioning the pivot point, the laser can easily scan over a large wavelength range without mode hopping.

Most commercially available ECLD systems are based on this design as its per-
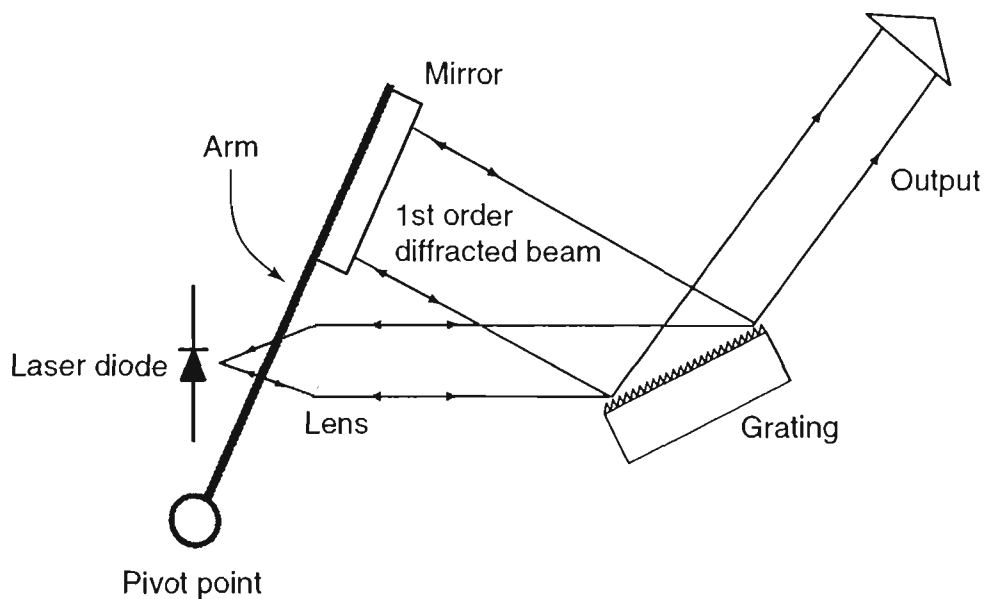
**Figure 2.2**: Schematic diagram of a Littman-Metcalf configuration external cavity laser diode. Light from the laser is collimated and then incident on a diffraction grating. Part of the light is diffracted onto a rotating mirror and part of it is reflected out. The light diffracted onto the mirror reflects back onto the grating to be diffracted once again into the laser diode.

formance and operating characteristics are superior to Littrow configuration lasers.

## 2.3 External cavity laser diodes constructed

In the present work, two types of ECLDs have been constructed. These are described in detail in the following sections and are based on the designs presented in references [7] and [19], both of which are Littrow configuration lasers. Given the disadvantages described above, Littman-Metcalf may seem the preferable choice, however, these particular Littrow configuration lasers are far simpler mechanically, and therefore can be made with relative ease. They also possess all of the operating characteristics (namely narrow linewidth and a sufficiently large mode hop free scan range) required for the experiments described in this thesis.

## 2.3.1 Macadam Laser

The laser described in this section is based on a modified version of the design of Macadam *et al.* [7]. A schematic diagram showing the main components of this laser is given in figure 2.3. The primary components of this ECLD are a laser diode, collimating lens, diffraction grating, mirror mount, piezoelectric disc, an Invar baseplate and an aluminium mounting block.

The laser diode fits snugly in a tube which is held in an aluminium mounting block. A collimating lens ($f = 5$ mm, NA $= 0.45$) is mounted in a separate threaded tube which screws into that of the laser. This allows the distance between the lens and the diode to be easily and precisely adjusted to obtain the optimum laser collimation. Both tubes sit in the aluminium mounting block. All of these components (laser diode, collimating tube and aluminium mounting block) are in good thermal contact with each other and also the Invar baseplate.

Light from the laser is collimated and directed onto a diffraction grating (Edmunds Scientific A43847 gold coated, 1200 lines/mm, 750 nm blaze), which is oriented at the Littrow angle ($\theta_L = 27.9°$ for this grating at 780 nm). The diffraction grating is glued onto a mirror mount (New Focus 9806) which allows the vertical and horizontal alignment of the grating angle to be independently adjusted. The adjustment screws on the mount are used for coarse alignment and wavelength selection. A PZT disc located between the plate which the grating is attached to, and one of the adjustment screws of the mirror mount, is used for fine control of the grating angle. This allows the laser wavelength to be controlled very precisely via an electronic signal, which is important when scanning the laser over an atomic transition or locking to a transition peak.

The cavity should be thermally stable so that the distance between laser diode and grating remain steady. If this length varies, it will lead to cavity mode jumps causing wavelength instability. Additionally, it is important to keep the laser diode itself at a stable temperature so that, (i) it does not overheat, and (ii) its operating wavelength remains stable. Fluctuations in the temperature of the diode and the
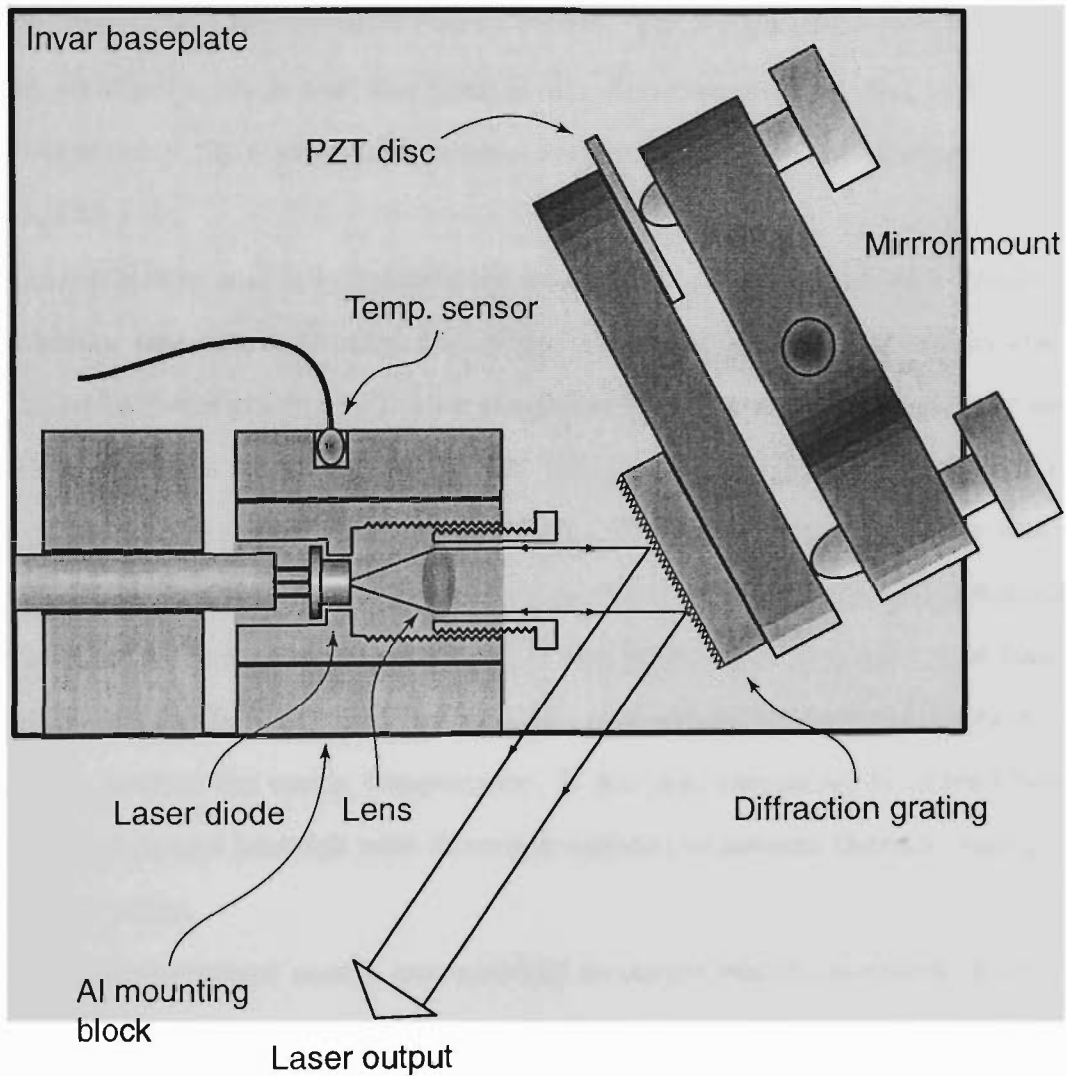
**Figure 2.3**: Schematic diagram of the ECLD, based on the design of [7]. The laser diode and collimating lens are held coaxially in two threaded tubes. Light from the diode is collimated and then incident on the diffraction grating at the Littrow angle (28°). The grating is glued to a mirror mount attached to the baseplate. The angle of the grating is adjusted by the screws of the mount and the PZT disc.

cavity result in frequency drifts at a rate of 4 GHz/°C and 7 GHz/°C respectively for this type of laser [7].

Invar was chosen as the baseplate material because of its extremely low thermal expansion coefficient. The Invar baseplate is temperature controlled by two Peltier coolers driven by a temperature control circuit. The temperature sensor is mounted in the aluminium block near the laser diode. A circuit diagram and explanation of the operation of the temperature control system constructed for this laser are given in Appendix A.

Once the laser was fully constructed and aligned, it was placed in a Perspex box to minimise air currents through the cavity. This improves the temperature stability and helps keep the grating and other components free from dust. As already stated, the Peltier coolers were attached to the bottom of the Invar baseplate. The other side of the Peltiers were attached to a large aluminium heatsink. This was then attached to a larger mild steel base which provided a massive and stable foundation for the laser system. The thermal mass of the Al heatsink and mild steel base was far greater than that of the laser and its components so that the Peltiers could efficiently control the cavity temperature. It was also important to ensure that the laser baseplate and heatsink were thermally isolated to prevent thermal leakage from one to the other.

A precision current source was essential to ensure stable operation of the laser. Instabilities in the operating current translate into instabilities in the operating frequency of the laser (200 MHz/mA) [7]. The laser diode was driven by a Newport 505 current driver operated in constant current mode. An attractive feature of this current supply is that it has the option to apply modulation from an external source to the laser diode which was particularly useful for locking the laser.

The laser diodes used for this ECLD were Sharp LTO25MD diodes which have a nominal operating wavelength of 780 nm and output power of 30 mW (free running). In the external cavity configuration however, the operating characteristics are substantially altered and the threshold current for the diode was seen to drop

by around 10%.

In the present system, the grating was blazed in the direction of the feedback, to provide maximum optical feedback to the laser diode. This was done to maximise control of the diode using grating feedback. However, it did mean that the power inside the cavity was substantially higher than the output coming off the grating. Typically, with $\approx 20\,\text{mW}$ of laser power in the cavity, $5\,\text{mW}$ would be coupled into the output.

## 2.3.2 Arnold laser

The laser described in this section is based on the design of Arnold *et al.* [19]. The essential features of this laser are the same as for the previous laser however, now all components fit neatly onto a mirror mount. A schematic of this ECLD is given in figure 2.4.

The laser diode and lens ($f = 4.5\,\text{mm}$, $NA = 0.55$) were once again located in a collimating tube (ThorLabs LT230P-B). This tube was attached to the back plate of a Newport U100-P mirror mount. The front plate was machined away to allow space for the laser beam to pass. A small aluminium block was attached to the front plate of the mount with one side machined away at 45°. A PZT disc was glued onto this surface, and a diffraction grating (Richardson Grating Laboratory, gold-coated holographic, 1800 lines/mm) was glued to the other side of the PZT ($\theta_L = 44.6°$ for this grating at 780 nm). This created an external cavity which is shorter and simpler and has less scope for mechanical creep. The mirror mount was attached to an aluminium baseplate which was temperature stabilised by a Peltier cooler. It was not necessary to use an Invar baseplate for this laser as the cavity length is determined by the mirror mount, which operates independent of the baseplate. The Peltier was driven by a commercial temperature controller (Newport 325) and the temperature sensor was located in the collimating tube near the laser diode.

The grating/laser were aligned coarsely using the adjustment screws on the mirror mount. For fine adjustments of the laser wavelength, two PZTs are available.
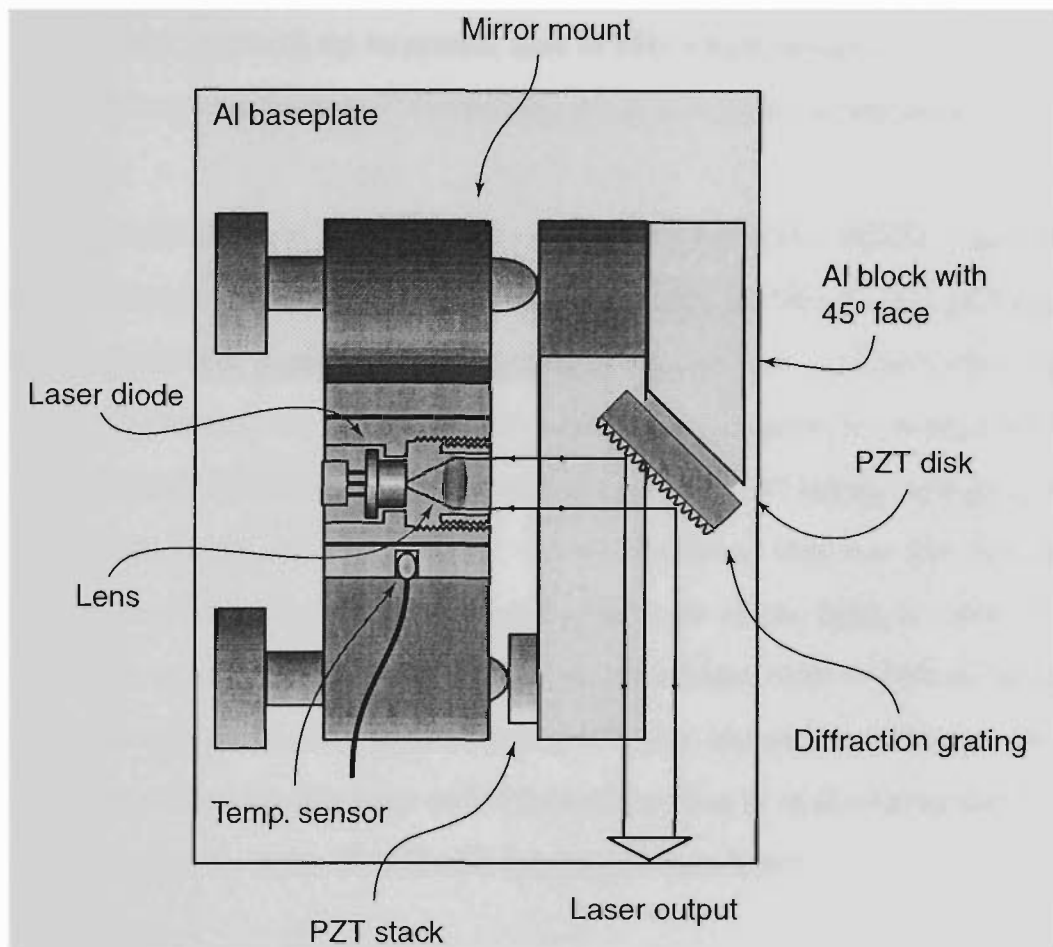
**Figure 2.4**: Schematic diagram of the ECLD, based on the design of [19]. The laser diode and collimating lens are held coaxially in a tube attached to a mirror mount. Light from the diode is collimated and then incident on the diffraction grating at the Littrow angle for this grating (45°). The grating is glued to a PZT disc which is glued to an aluminium block. This block is attached to the mirror mount which is screwed to the baseplate. The angle of the grating is adjusted by the screws of the mount and the PZT disc.

One, a PZT stack, is located between the front plate of the mirror mount and the ball end of the adjustment screw. This is used for scanning the wavelength over a large range and its response is not particularly quick (up to several tens of Hz). The other, a PZT disc located between the grating and 45° aluminium block, is used to quickly scan the cavity length and hence the laser frequency over short ranges. It has a frequency response up to several tens of kHz which means it can be used for fast modulation and frequency corrections when locking to a transition peak (see section 2.5).

A Spectra Diode Labs SDL-5401 laser diode was used in this ECLD. These diodes nominally provide 50 mW output power at a wavelength of 780 nm. The grating used in this laser provides significantly less feedback than the one used with the previous laser. As a consequence, the threshold current only dropped by around 5% with feedback aligned. However, this reduced feedback was still strong enough to force the diode into single mode operation. An advantage of this was the substantial increase in the output power off the grating as more of the light is reflected out. Typically, the power coming out of the cavity was between 50% to 55% of the power in the cavity compared with approximately 25% for the previous design. Normal operating conditions for this laser would have about 45 mW in the cavity and 23 mW output, substantially more than 5 mW for the previous laser.

## 2.4 Saturated absorption measurements

With construction and alignment of the lasers completed, it was necessary to assess their performance. This required adjusting the operating conditions (temperature, injection current and grating alignment), so that the lasers could be scanned over the $D_2$ transition in rubidium. At a preliminary stage, this involved passing the lasers through a rubidium vapour cell and viewing the cell with an infrared camera, looking for fluorescence. Once seen, the laser was known to be tuned to one of the Doppler broadened atomic transitions. Next, a saturated absorption measure-

ment was performed to examine how well the rubidium atomic transitions could be resolved.

A saturated absorption measurement provides a good indication of the linewidth and mode-hop-free scan range of the lasers. With a suitable laser, it is possible to resolve and scan continuously over all of the features of the saturated absorption spectrum of the rubidium $D_2$ transitions. This was particularly important here as the lasers were to be locked to these features.

Saturated absorption spectroscopy has long been used as a means to obtain spectroscopic information with sub-Doppler resolution [1]. A schematic of the experimental arrangement used for the saturated absorption measurements is given in figure 2.5.

Output from an ECLD was split into two beams, one was used in the saturated absorption measurement and the other was sent to a spectrum analyser (with 300 MHz free spectral range and finesse greater than 150). The spectrum analyser monitored the relative frequency of the laser as it was scanned across a transition.

The beam for the saturated absorption experiment was then further split into three beams using a thick glass beam splitter. Two weak beams, the reference and probe, were reflected from the front and back surfaces of the beam splitter respectively. Both of these beams co-propagated parallel to each other through a vapour cell and onto photodiodes. The transmitted beam (pump) was reflected around and through the cell in the opposite direction to the probe and reference. It overlapped the probe beam at approximately 180° and did not cross the reference beam.

When the laser frequency lies within a Doppler broadened absorption profile, but not precisely on an atomic resonance, the pump laser excites a different velocity group of atoms to the probe and reference lasers. This is due to the opposite Doppler shift for the counter propagating lasers. In this situation, the probe and reference beams experience the same absorption and therefore give rise to essentially the same photodiode signals.
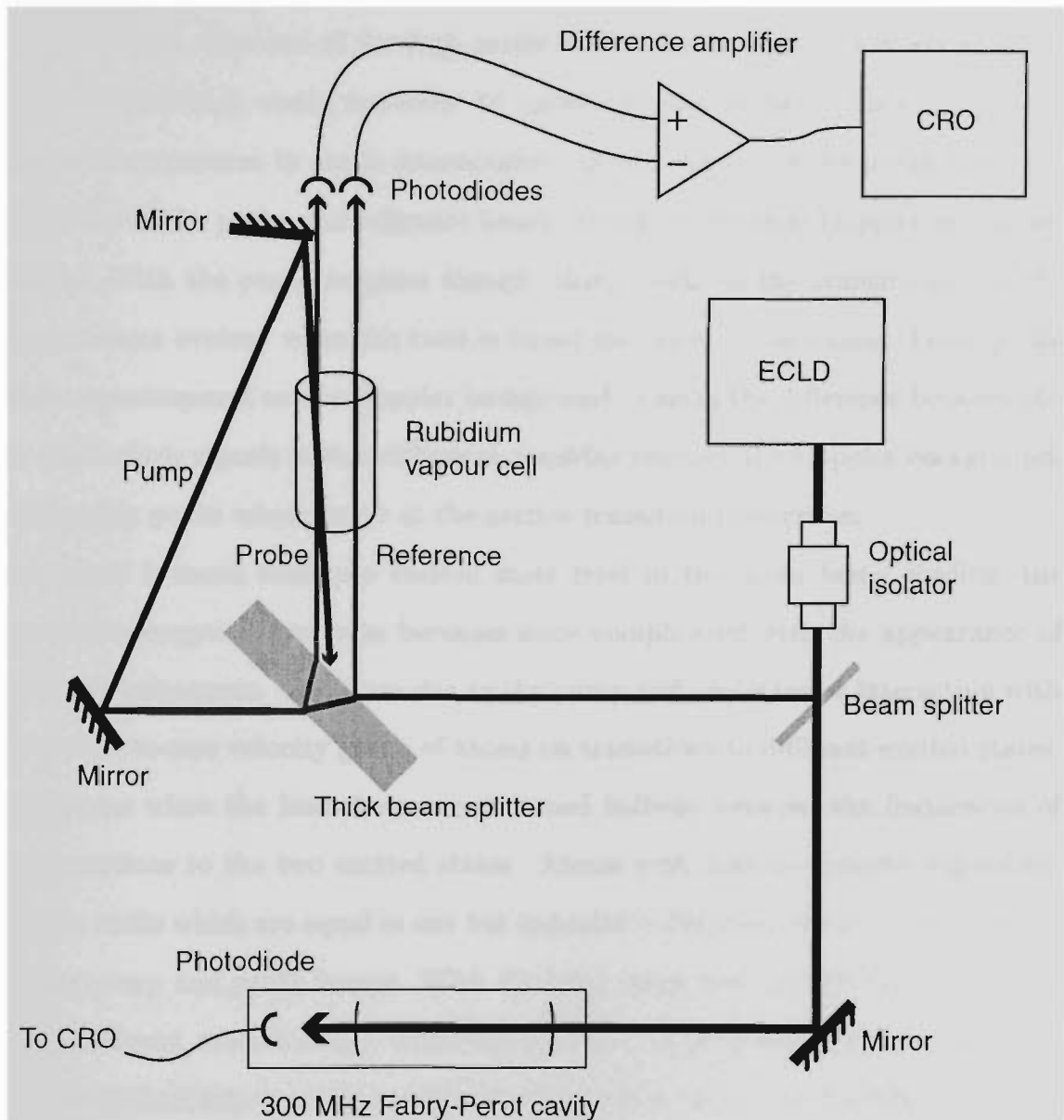
**Figure 2.5**: Schematic of the experimental arrangement for saturated absorption spectroscopy. The laser is split into two beams, one is used in the saturated absorption measurement and the other is sent to a spectrum analyser. The saturated absorption beam is then further split into three beams; the pump, probe and reference beams. The probe and reference beams co-propagate parallel to each other through the cell and onto two photodiodes. The pump propagates in the opposite direction and overlaps the probe beam. A difference amplifier is used to subtract the Doppler background and leave only the signal due the saturation induced by the pump. A 300 MHz confocal Fabry-Perot spectrum analyser was used to monitor the laser frequency.

If however, the laser frequency is tuned precisely to an atomic resonance (i.e. for zero velocity atoms), all three laser beams will be exciting the same velocity group of atoms. Because of the high power in the pump beam, it will excite many of the atoms which would normally be excited by the probe. This results in an on-resonance increase in probe transmission. In the absence of the pump laser, the absorption of the probe and reference beams would be identical Doppler broadened profiles. With the pump in place though, sharp peaks in the transmission of the probe become evident when the laser is tuned precisely on resonance. These peaks will be superimposed on the Doppler background. Taking the difference between the two photodiode signals with a difference amplifier removes the Doppler background, leaving only peaks which occur at the precise transition frequencies.

If there is more than one excited state level in the atom being studied, the saturated absorption spectrum becomes more complicated with the appearance of cross-over resonances. These are due to the pump and probe lasers interacting with the same non-zero velocity group of atoms on transitions to different excited states. They occur when the laser frequency is tuned halfway between the frequencies of the transitions to the two excited states. Atoms with nonzero velocity experience Doppler shifts which are equal in size but opposite in direction, for the counter propagating pump and probe beams. With the laser tuned halfway between transitions to two different excited states, there will be one velocity group of atoms which are Doppler shifted into resonance with one laser beam to one of the excited states. And, this same velocity group will be Doppler shifted into resonance with the other laser on the transition to the other excited state. As both lasers are interacting with the same velocity group of atoms, the pump laser is again removing atoms which could normally absorb probe radiation. Therefore, the probe transmission will also show sharp peaks when the laser frequency is tuned halfway between two excited states as well as when it is tuned to a true hyperfine transition (a more detailed discussion can be found in [1]).

Saturated absorption scans of the four Doppler broadened transitions of the

rubidium $D_2$ line were obtained using the ECLDs described above. The intensities of the probe, reference and pump beams were approximately $1\,mW/cm^2$, $1\,mW/cm^2$ and $5\,mW/cm^2$, respectively. Figure 2.6 shows saturated absorption scans from the $F' = 2$ and $F' = 3$ ground states in $^{85}$Rb. Scans for both ground states of $^{87}$Rb are shown in figure 2.7. The frequency scales were derived from the transmission of a 300 MHz confocal Fabry-Perot spectrum analyser. Transitions to the true excited state hyperfine levels have been labelled by the hyperfine quantum number, F, of the excited state. Crossover peaks have been labelled (in brackets) with the hyperfine quantum numbers of the two excited state levels involved. All of the expected features in these spectra are present and clearly resolved.

These traces indicate that the linewidth of the laser is narrow enough to resolve the spectroscopic features we will study in later experiments. During the course of these measurements, the mode hop free scan range of the lasers was observed to be typically of the order of 3 GHz. This in itself is not particularly critical, however, it is larger than the width of the Doppler broadened transitions indicating that the frequency can be scanned continuously across the ranges required for typical experiments.

## 2.5 Laser Stabilisation Schemes

External cavities greatly improve the spectral stability and linewidth of laser diodes. However, due to factors such as mechanical creep and temperature and injection current fluctuations, their stability is still not optimal. With the grating feedback, the short-term (100 ms) linewidth is reduced to a few hundred kilohertz. There is however, substantial jitter and long term drift which increase the linewidth to tens, or even hundreds, of megahertz over a period of several hours.

For many applications, including the present work, it is necessary to further stabilise the laser frequency to eliminate these long term drifts. One way to achieve this is to use electronic feedback to lock the laser frequency to a well defined atomic
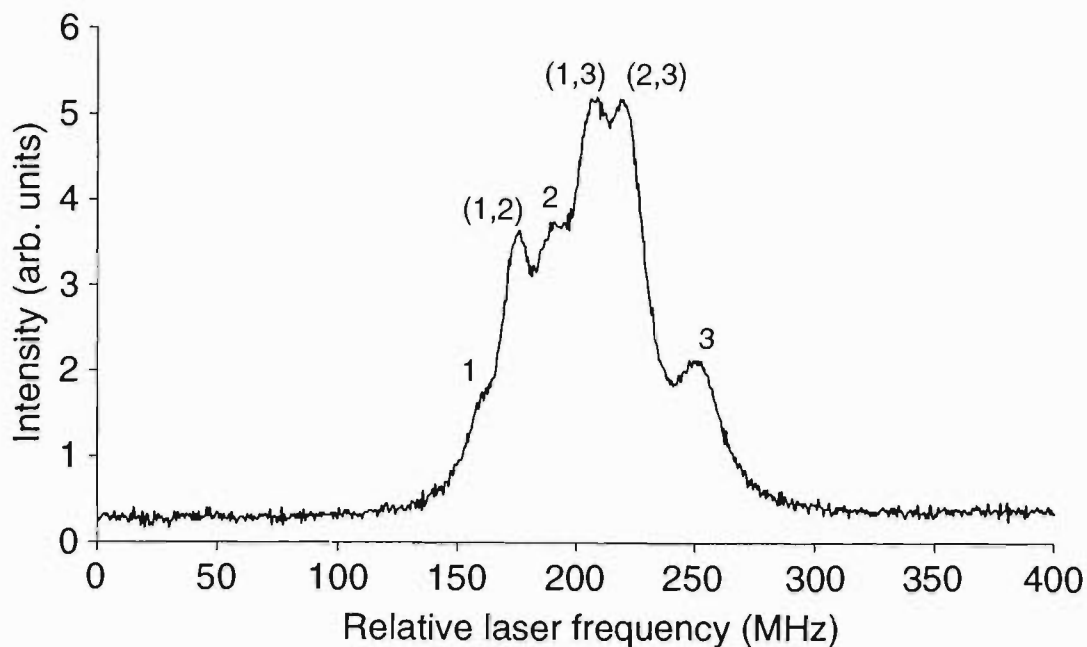
(a) Saturated absorption scans for $^{85}$Rb, $F' = 2$ to $F = 1, 2$ and $3$
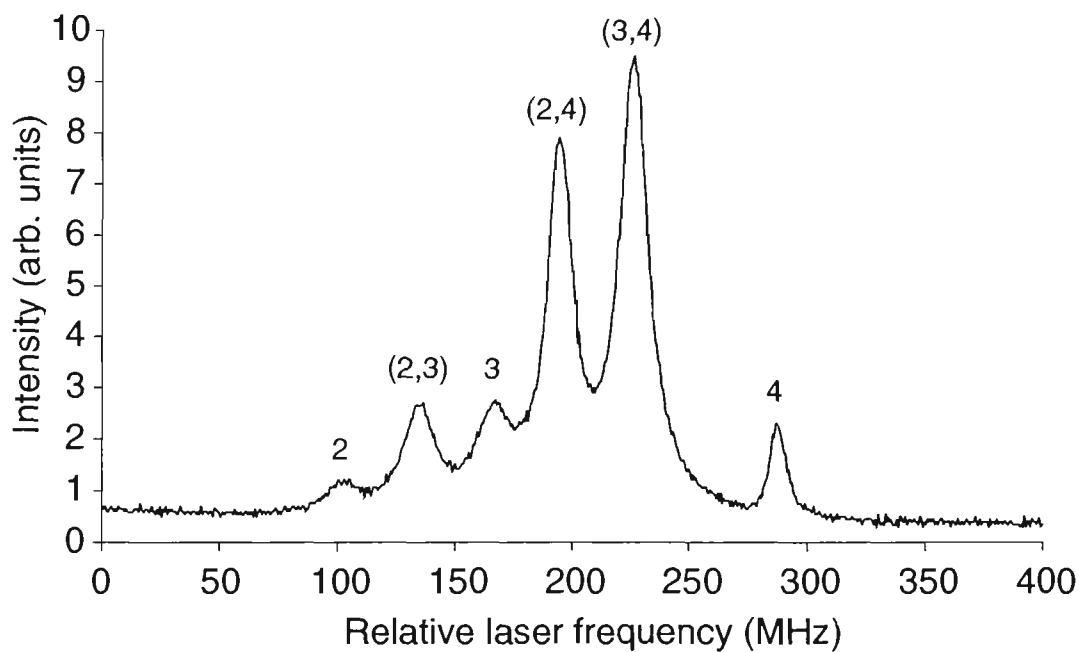


(b) Saturated absorption scans for $^{85}$Rb, $F' = 3$ to $F = 2, 3$ and $4$

**Figure 2.6**: Saturated absorption scans for the $5S_{\frac{1}{2}}$ to $5P_{\frac{3}{2}}$ levels of $^{85}$Rb. Transitions to true excited state hyperfine levels are labelled with the excited state hyperfine quantum number, F, and crossover resonances are labelled (in brackets) by the two excited state involved.
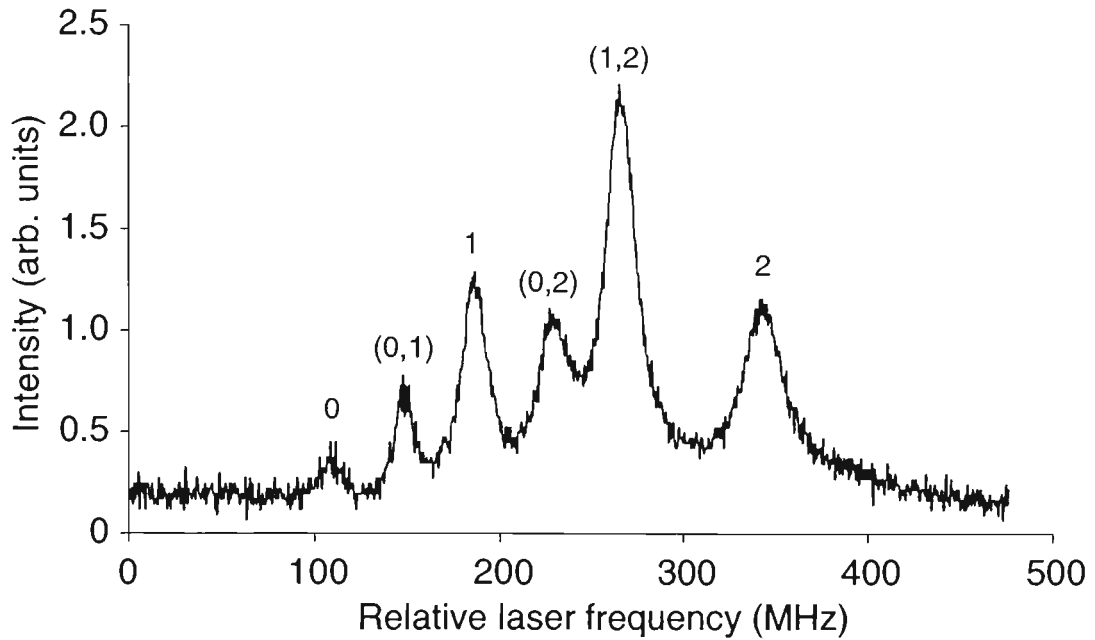
(a) Saturated absorption scans for $^{87}$Rb, F$'$ = 1 to F = 0, 1 and 2
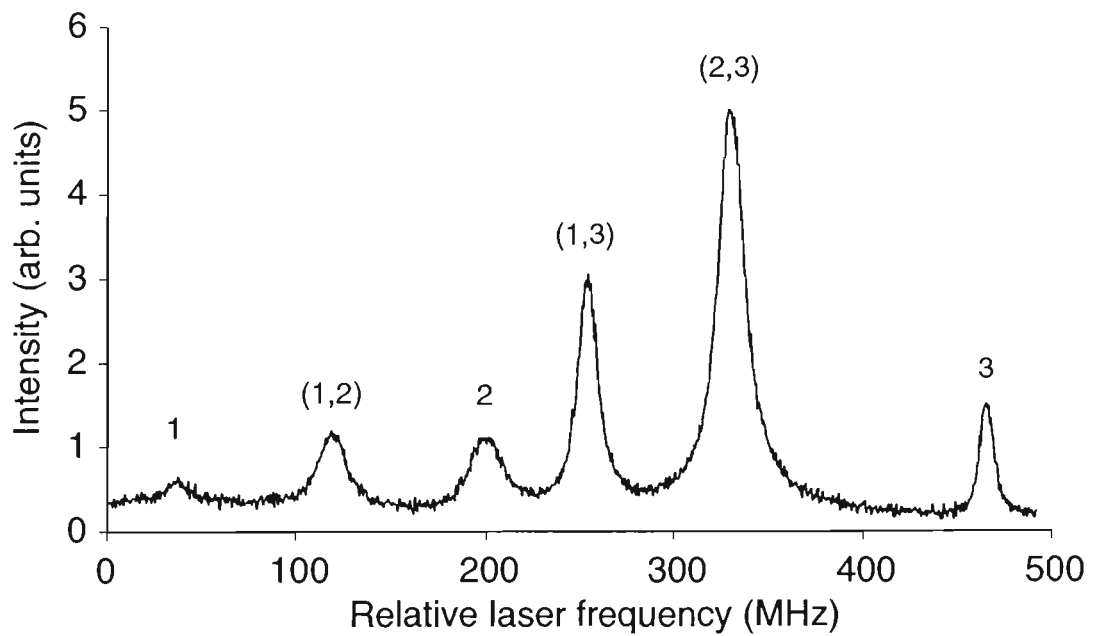


(b) Saturated absorption scans for $^{87}$Rb, F$'$ = 2 to F = 1, 2 and 3

**Figure 2.7**: Saturated absorption scans for the $5S_{\frac{1}{2}}$ to $5P_{\frac{3}{2}}$ levels of $^{87}$Rb. Transitions to true excited state hyperfine levels are labelled with the excited state hyperfine quantum number, F, and crossover resonances are labelled (in brackets) by the two excited state involved.

spectral feature.

Several methods for locking lasers this way have been reported, see for example [7, 31, 32, 33]. In these techniques, a photodiode signal, based on resonant absorption, provides a stable frequency reference to which the laser is locked. This photodiode signal is sent into a feedback circuit which drives the frequency selective elements of the ECLD, bringing the laser back to the desired lock point. The feedback signal generated can be sent to the PZT element(s) and/or the laser diode injection current. Typically, the response of a PZT is far slower than that of the injection current but the injection current can only be used to scan the laser over a small range. For this reason, the PZT stack is used for slow ($<$ 100 Hz) corrections to the laser frequency and the injection current or PZT disc are used for fast, small amplitude corrections.

In the present work, two locking techniques have been applied and tested . These are the dichroic-atomic-vapour laser lock (DAVLL) described by Corwin *et al.* [32] and the AC lock described by Dinneen *et al.* [31]. These two methods were selected as they are robust and able to lock lasers to the frequencies we required for later experiments. Both of these methods have been shown to stabilise ECLDs to better than 1 MHz over a period of several hours. They also allow the lock point to be scanned over a range of frequencies around resonance.

An electronic circuit, which takes the signal from a photodiode, processes it, and then uses this to drive both the fast (injection current/PZT disc) and slow (PZT stack) frequency selective elements to keep the laser at the desired lock point, was developed. A diagram and brief description of this circuit is given in appendix B.

## 2.5.1  Dichroic-atomic-vapour laser locking

The DAVLL technique uses the Zeeman shift to generate an asymmetric signal about a Doppler-broadened atomic transition [32]. This asymmetric signal provides a slope, with a zero crossing, to which the laser frequency is locked. The lock point can be continuously scanned over a large portion of the Doppler profile, encompassing all of the hyperfine transitions making this a versatile locking scheme.

A diagram of the setup used for DAVLL locking is given in figure 2.8. A fraction of the laser output is taken off a beam splitter and sent through a rubidium vapour cell. Permanent ring magnets are placed around the cell to provide a longitudinal magnetic field of approximately 10 mT. Light from the laser which enters the cell is linearly polarised. Linear polarisation can be considered as equal amounts of left and right handed circularly polarised light. In the absence of any magnetic fields, both of these circular polarisation components, $\sigma^+$ and $\sigma^-$, experience the same absorption as the laser frequency is scanned across an atomic transition. However, with a longitudinal field applied, the Zeeman shift changes the resonant frequency in opposite directions for the two polarisation components. This shifts the absorption profiles for each of the polarisations in opposite directions.
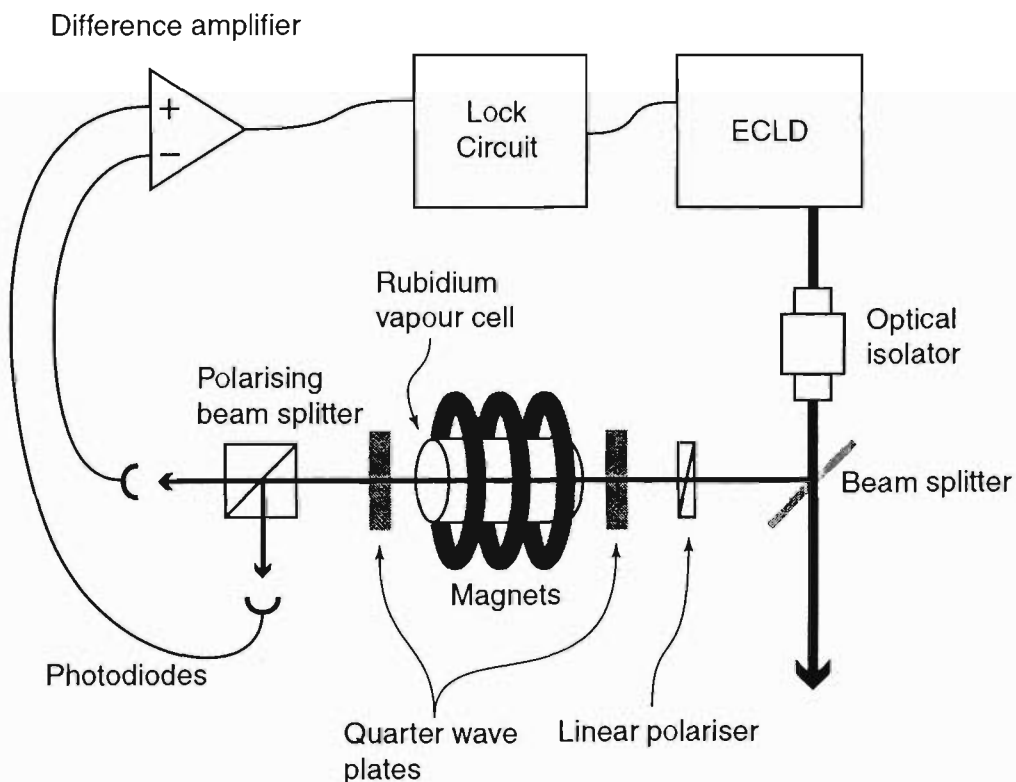


**Figure 2.8**: Schematic diagram of the experimental arrangement for DAVLL locking, after [32]. Light from the laser passes through a linear polariser, and then through a vapour cell. Permanent magnets around the cell provide a DC magnetic field of $\approx$ 10 mT in the cell. After passing through the cell, a quarter-wave plate splits the light into its polarisation components which are incident on two photodiodes. The difference of the PD signals give the DAVLL signal which is sent to the locking circuit to lock the laser.

After passing through the cell, the two circularly polarised components are converted into two orthogonal linear components by a quarter wave plate with its optic axis oriented at 45° to the initial linear polarisation. These are then separated by a polarising beam splitter and directed onto two photodiodes. Taking the difference between the absorption of the two beams (the photodiode signals) gives a curve which is asymmetric about the frequency of the atomic resonance. The difference of the photodiode signals gives the DAVLL signal used to lock the laser.

Figure 2.9 shows a typical DAVLL signal when the laser was scanned over the $^{85}$Rb $F' = 3$ to $F = 2, 3$ and 4 transition, along with a saturated absorption scan for frequency reference. The lock point, circled on the trace, occurs where the dispersion signal crosses zero. By adjusting either the angle of the quarter wave plate or the voltage offset applied to the DAVLL signal, the lock point could be easily scanned over a continuous range of approximately 250 MHz, centred around the hyperfine transition peaks.

The linewidth of lasers locked using this technique was measured by beating two locked lasers together and monitoring the beat note on an RF spectrum analyser. The short term linewidth of the lasers was found to be approximately 1 MHz. However, over a longer period, a slow drift in the laser frequency of approximately 10 - 20 MHz per hour was observed. This was attributed to temperature fluctuations in the experimental setup. It has been suggested that small variations in the temperature of optical components such as the polarising beam splitter and quarter wave plate, combined with temperature changes in the vapour cell, reduce the long term stability of this locking technique [32]. It is believed, that these factors, and possibly instabilities in the reference voltages of the locking electronics, led to the long term drift.

It may have been possible to overcome this problem by enclosing the setup in a temperature controlled environment. However, as the locking setup was already enclosed in a Perspex box (to shield it from stray air currents), it seemed as though a lot of effort would be required to achieve the necessary stability.
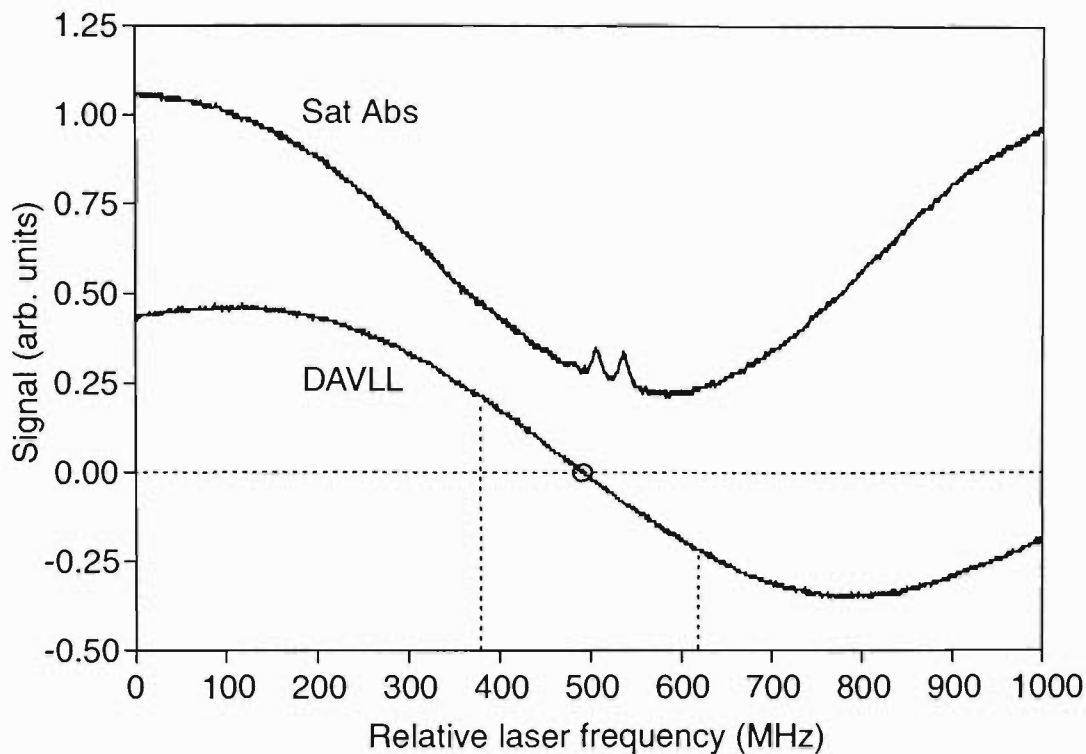
**Figure 2.9**: Dispersion signal for DAVLL locking. Top trace shows a saturated absorption scan of the $^{85}$Rb F' = 3 to F = 2, 3 and 4 D$_2$ transition (only the two large crossover peaks are visible). Bottom trace shows the DAVLL signal to which the laser can be locked. By adjusting the voltage offset the laser lock point (circled) could be shifted anywhere over the range of approximately 250 MHz as indicated.

This meant that the DAVLL technique would be of limited use for some of our desired applications so we were forced to use another locking scheme.

## 2.5.2 AC locking

The AC locking technique, overcomes the slow drift problems encountered with the DAVLL method by locking to the peak of one of the hyperfine or crossover resonances like those shown in figures 2.6 and 2.7. These peaks are insensitive to drifts in laser intensity or the temperature of the cell or other optical components, making this method more reliable. This technique is based on that described in [31].

A diagram of the experimental arrangement used for AC locking is given in figure 2.10. Part of the output of an ECLD is taken into a single beam saturated absorption setup. A low amplitude frequency modulation is added to the laser at 24 kHz. This

frequency was chosen to avoid resonances in the PZT disc which could make the laser behave erratically. The modulation is achieved by applying a dither to either the injection current or PZT disc of the laser. The amplitude of the modulation was small, less than 1 MHz peak to peak in terms of optical frequency, to avoid any undesired line broadening.

The signal from the photodiode which monitors the saturated absorption is taken into a lock-in amplifier tuned to the frequency of the modulation (24 kHz). The lock-in amplifier extracts the information at this frequency from the total photodiode signal. This yields a signal with dispersion shaped features at the frequencies of the hyperfine transition peaks and crossover resonances.

This scheme has also been realised on the $D_2$ line in rubidium. Figure 2.11 shows a typical dispersion signal produced by the lock-in, along with the saturated absorption scan (which is simply the total photodiode signal) for frequency reference. The dispersion signal crosses zero at positions corresponding to the top of the hyperfine or crossover peaks. These are the positions at which the laser can be locked.

Lasers locked using this technique generally remained locked for periods of several hours. Because the laser is now locked to a much narrower spectral feature, the linewidth and long term stability are both significantly better than for the DAVLL technique. A beat signal between two AC locked ECLDs monitored on a RF spectrum analyser showed a short term width of less than 1 MHz. Over a period of approximately one hour, the beat note was stable to within 2 MHz of its initial frequency.

Also shown in figure 2.10 is a solenoid surrounding the vapour cell. This is so that a variable strength DC magnetic field can be applied to the cell. Note also that there are two quarter wave plates located on either side of the cell, so that both the incident and return beams of the saturated absorption setup have the same handed circular polarisation (ie. both $\sigma^+$ or both $\sigma^-$).

When a current is supplied to the solenoid a longitudinal magnetic field is created in the cell. This induces a Zeeman shift in the energies of the magnetic sublevels of
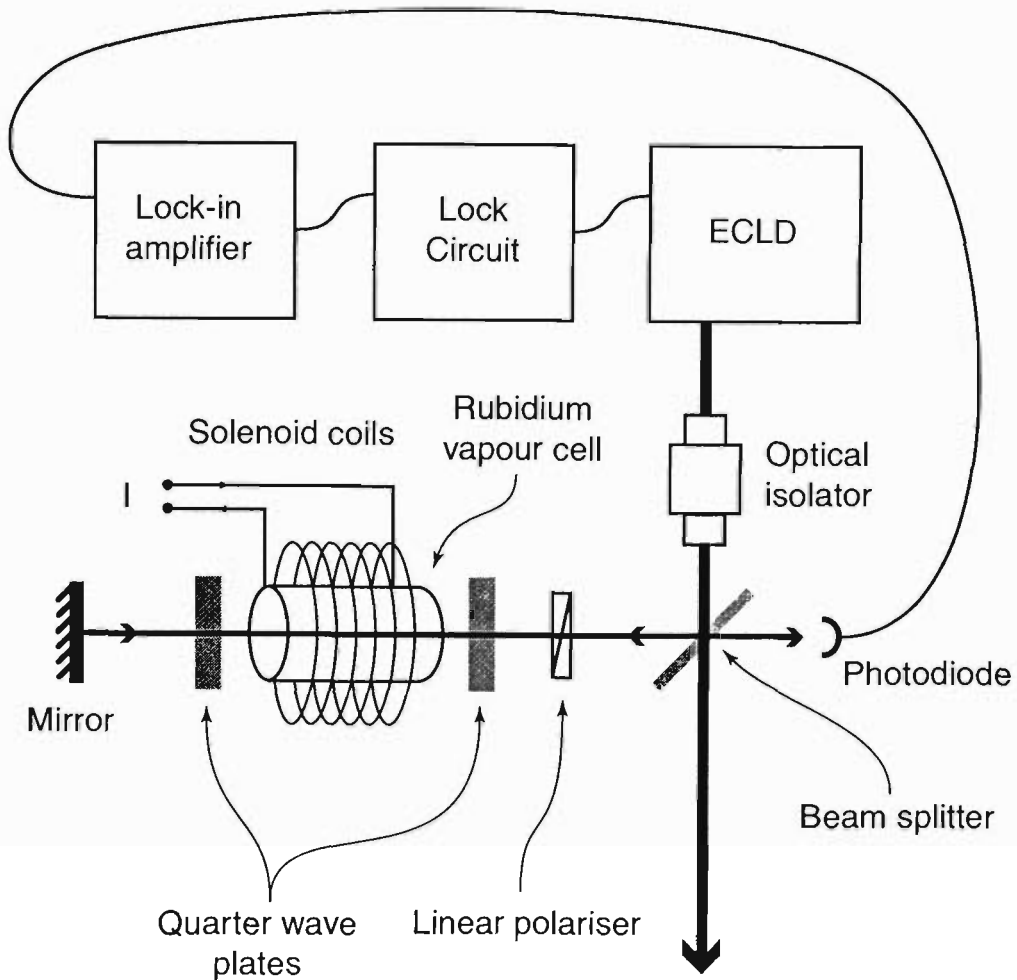
**Figure 2.10**: Schematic diagram of the experimental arrangement for AC locking, after Dinneen *et al.* [31]. Modulated light from the laser diode is sent into a single beam saturated absorption setup. This is measured on a photodiode and this signal is sent to a lock-in amplifier. The lock-in extracts the information which occurs at the modulation frequency, yielding a dispersion curve to be used by the locking circuit to lock the laser.

the atoms. Using either $\sigma^+$ or $\sigma^-$ light, we optically pump atoms so that essentially only the extreme magnetic sublevels of the ground and excited states are involved in the transition. The Zeeman shifts in these ground and excited sublevels are opposite in direction, and hence will result in an apparent shift of the atomic resonance frequency. By controlling the magnetic field applied to the cell, we can control the shift in resonance frequency and hence tune the position of the lock point.

With the application of suitable magnetic fields, the lock point could be continuously scanned over a range of about $-20$ MHz below to about $+30$ MHz above the
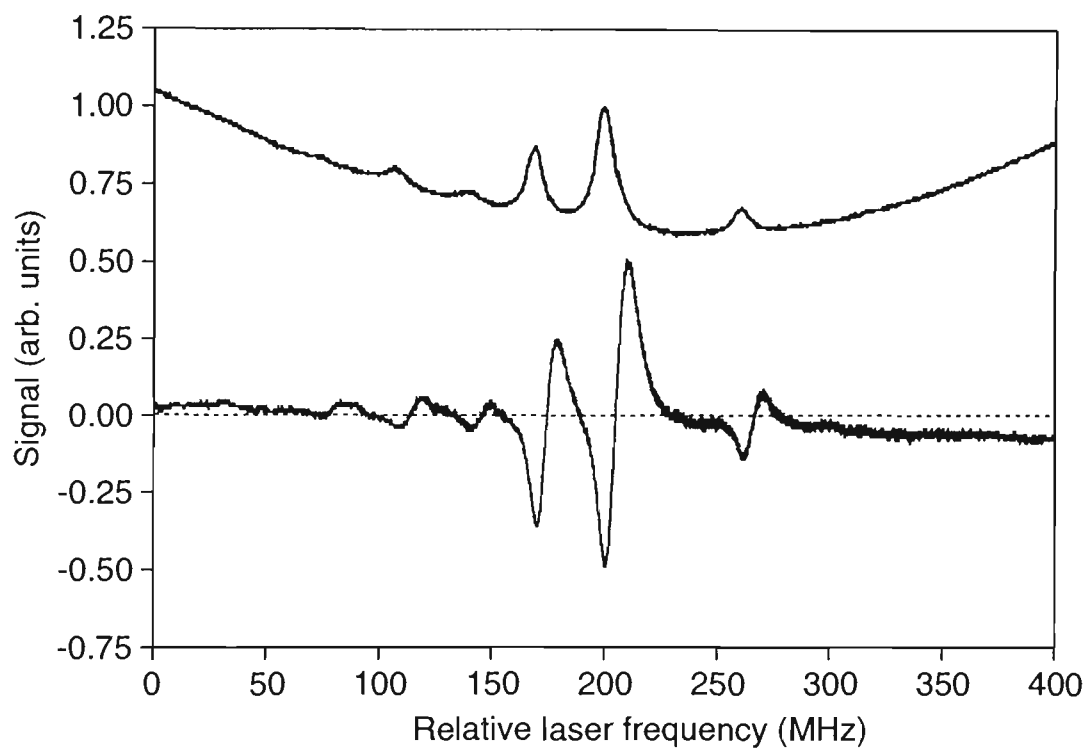
**Figure 2.11**: Dispersion signal for AC locking. Top trace shows a saturated absorption scan of the $^{85}$Rb F' = 3 to F = 2, 3 and 4 $D_2$ transition. Bottom trace shows the signal from the lock-in amplifier to which the laser can be locked. The laser can be locked to any of the hyperfine transition peaks where the dispersion signal crosses zero.

zero field resonance. Later, in the laser cooling studies (chapter 5), it was necessary to precisely scan the frequency of a laser over a small range around the $F' = 2$ to $F = 3$ transition in $^{87}$Rb. This locking technique allowed us to do so quite simply through the application of suitable magnetic fields.

## 2.6 Conclusions

In this chapter, the history of the development of laser diodes and their applications to atomic physics has been briefly reviewed. A discussion of the principles of operation of external cavity diode lasers has been given along with a detailed description of the lasers built for the present study. Upon testing these lasers using a saturated absorption experiment, it was seen that the lasers had linewidth and tunability which enabled them to be locked to atomic spectral features. Frequency stabilisation schemes suitable for our requirements were developed and tested. The lasers were found to perform well once AC locked to an atomic transition. These locked ECLDs form a major tool required to perform the vapour cell atomic beam experiments described in subsequent chapters.

# Chapter 3

# THE VAPOUR CELL ATOMIC BEAM

Creating an atomic beam in a vapour cell involved the development of a velocity selective optical pumping scheme which used two spatially separated lasers. One laser was used to label a particular velocity group of atoms, and another laser detected these atoms in a different position in the cell. In this chapter, a description of the vapour cell atomic beam system is provided along with an analysis of some of the important physical properties of the beam.

In section 3.1 a review of related vapour cell work using spatially separated lasers is presented. A general description of the labelling and detection mechanism is then given. A detailed explanation of the optical pumping scheme used to select and detect the right velocity groups of atoms with the $D_2$ transition in rubidium, is provided in section 3.3. The transverse velocity distribution of the VCAB is then calculated and compared to a real atomic beam. A discussion of the results and some limitations of the present scheme are provided in section 3.5.

## 3.1  Review of separated laser beam experiments

Vapour cell experiments utilising spatially separated laser beams have been reported by several groups. These techniques can be traced back to the early 1970's when Letokhov *et al.* proposed that separated pump and probe beams could be used to observe saturated absorption features, provided the lifetime of the excited state was longer than the average time taken for atoms to travel from one laser beam to the next [34].

This suggestion was realised experimentally by Baba in 1981 [35] in a methane cell

(resonance $\lambda = 3.39$ $\mu$m). The lifetime of the methane excited state was estimated to be about 10 ms, substantially longer than the time taken for the majority of atoms to travel the distance between the two laser beams. Lamb dips in the absorption of one of the beams were observed and found to be due to atoms excited by the other laser beam. In another report, Baba *et al.* extended this technique to the measurement of optical Ramsey resonances [36].

Phillips *et al.* proposed a velocity selective optical pumping scheme which used the Doppler shift to select and measure molecules with a specific velocity [37]. They demonstrated that it would be possible to measure molecules which have been involved in collisions with a background gas, by scanning the laser frequency across the Doppler profile. The velocity resolution they reported was comparable to what could be obtained using a conventional molecular beam. Later, in 1978, they used this technique to measure the angular scattering distribution of sodium atoms after collisions with argon [38].

In 1980 Nakayama *et al.* used polarisation spectroscopy to measure the Larmor precession of sodium atoms as they travelled between two adjacent laser beams [39]. Their scheme consisted of one laser split into a strong circularly polarised pump beam and a weaker linearly polarised probe beam. These beams were spatially separated and propagated antiparallel to each other through a vapour cell. The probe laser passed through a set of crossed polarisers on either side of the vapour cell so that under normal conditions no signal was measured. Atoms which passed through the pump beam were spin polarised. Any of these atoms which crossed the path of the probe would alter its polarisation and lead to some transmission through the crossed polarisers. An external magnetic field was applied which caused the spin polarised atoms to precess and this would "unwrite" the polarisation induced by the pump.

The probe laser transmission was measured as a function of the magnetic field for various beam separations. As the separation of the lasers was increased, the field required to unwrite the spin polarisation was seen to decrease. This is because at larger laser separations, the atoms had more time to evolve in the magnetic field.

Similar results to these were observed with the present VCAB as detailed in chapter 4.

A somewhat questionable report on the observation of atom collimation in a standard gas vapour cell was given by Wang *et al.* in 1993 [40]. They claim to have observed channelling of atoms through the nodes of an intense standing wave field. As stated in their paper however, their experiment did not have the resolution required to properly observe laser cooling, nor did they adequately consider the optical pumping processes. What they claim to be laser cooling appears to be better explained by optical pumping. As will be shown later, it is necessary to go to some lengths to attain the resolution required to observe laser cooling and then separate this from optical pumping. The resolution of their system was approximately two orders of magnitude worse than what we found to be suitable (chapter 5).

More recently, Skalla *et al.* have used separated beams in a vapour cell to perform Ramsey-type spectroscopy in sealed glass cells [41]. The pump laser in their case was pulsed, with a pulse duration much shorter than the Larmor period. Atoms were probed by a weaker laser at various positions in different shaped cells. The absorption of the probe was monitored as a function of time after the pump pulse and the spin signals were observed as periodic oscillations in the absorption signal. They also propose a novel scheme for the measurement of the Aharonov-Casher phase using their vapour cell atomic beam system.

In summary, experiments with spatially separated laser beams have proven to be useful in a number of applications ranging from simple spectroscopy, to more complex polarisation studies. The potential for further development of these techniques is clear providing much of the impetus for the present work.

## 3.2 Basic Arrangement for VCAB Experiments

The essential components required for the VCAB system described here are a vapour cell, two lasers, one (chopped) to label the appropriate atoms and another (probe) to
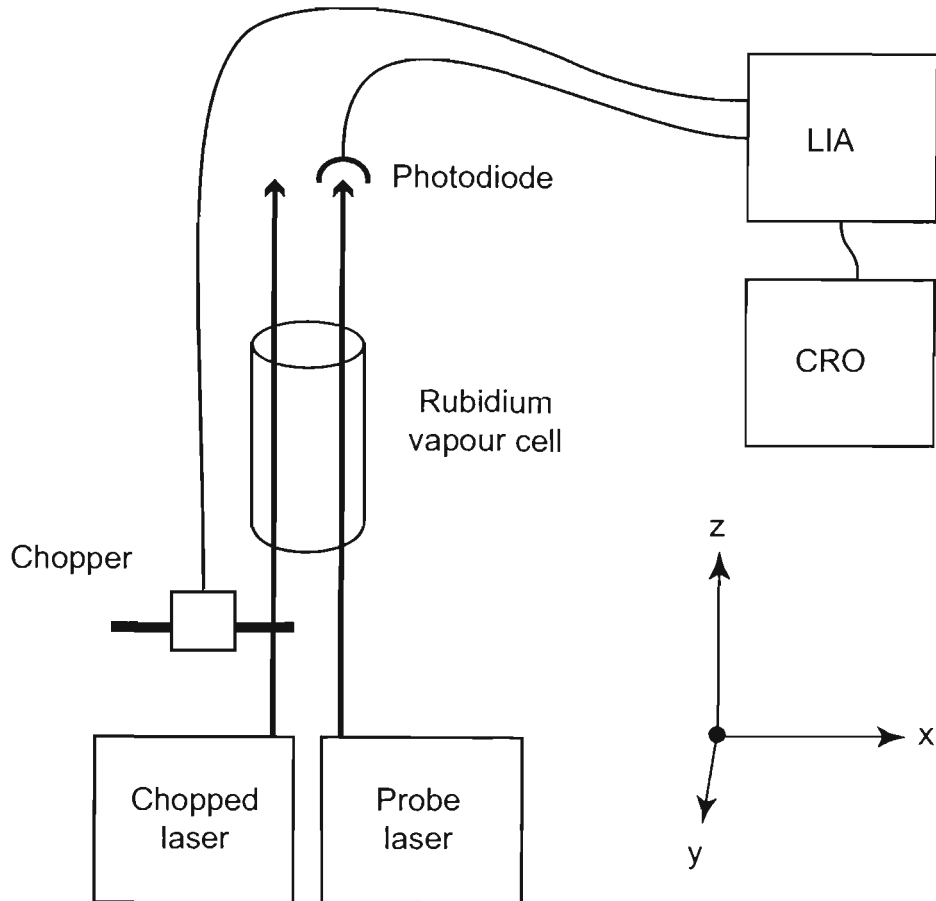
**Figure 3.1**: Experimental arrangement for observation of a vapour cell atomic beam. Two separated lasers travel parallel to each other through a Rb vapour cell. One is chopped at a frequency of approximately 2 kHz. The other (probe) is monitored on a photodiode and the photodiode signal is sent to a lock-in amplifier tuned to the frequency of the chopper. LIA = lock-in amplifier, CRO = oscilloscope. Both lasers propagate in the z-direction.

detect the labelled atoms (figure 3.1). A photodiode, chopper and lock-in amplifier are needed for signal detection.

The chopped laser is used to label to the desired velocity group of atoms (i.e. those travelling perpendicular to the two laser beams). This is achieved by optically pumping these atoms into a state which is not resonant with the probe laser. That is, the chopped laser modifies the atomic ground state population distribution. The chopped laser passes through a mechanical chopper which blocks and unblocks the laser at a frequency of approximately 2 kHz. Thus the labelling (modulation of the ground state populations) also occurs with this periodicity.

The probe laser copropagates, spatially separated and parallel to the chopped

laser, and its transmission is monitored on a photodiode. The absorption it experiences is dependent on (among other things) the number of atoms in the ground state it is resonant with. Any modulation of the number of atoms in this ground state (caused by the chopped laser) will show up as a modulation in the absorption of the probe.

The number of atoms which interact with the chopped laser and then contribute to the total absorption of the probe is relatively small. (A simple geometric calculation predicts that with 1 mm diameter beams, separated by 5 mm, only 3% of the atoms absorbed by the probe laser will have intersected the shopped laser path). Thus a lock-in amplifier, tuned to the frequency of the chopper, is used to extract any signal which occurs at that frequency. It follows that any signal observed on the lock-in must be due to atoms which have traversed both lasers, since the chopped laser is the only source of any 2 kHz modulation.

The vapour cell atomic beam appears as in figure 3.2. Atoms travelling perpendicular to both lasers, from the chopped to the probe, form a "ribbon" of atoms that constitute the beam.

## 3.3 VCAB in a rubidium cell

A scheme based on the ideas of section 3.2 has been realised using the $D_2$ transition in both $^{87}$Rb and $^{85}$Rb and could easily be replicated in many other elements or molecules. For the purpose of simplicity this description of the energy levels and optical pumping involved will be restricted to $^{87}$Rb. An analogous description could be made for $^{85}$Rb, the only difference being that the set of energy levels involved have different hyperfine quantum numbers due to the different nuclear spin ($I = \frac{5}{2}$ for $^{85}$Rb and $I = \frac{3}{2}$ for $^{87}$Rb). As the schemes in the two isotopes are so similar, only a brief outline for $^{85}$Rb will be provided. Before doing this however, some preliminary considerations need to be addressed.
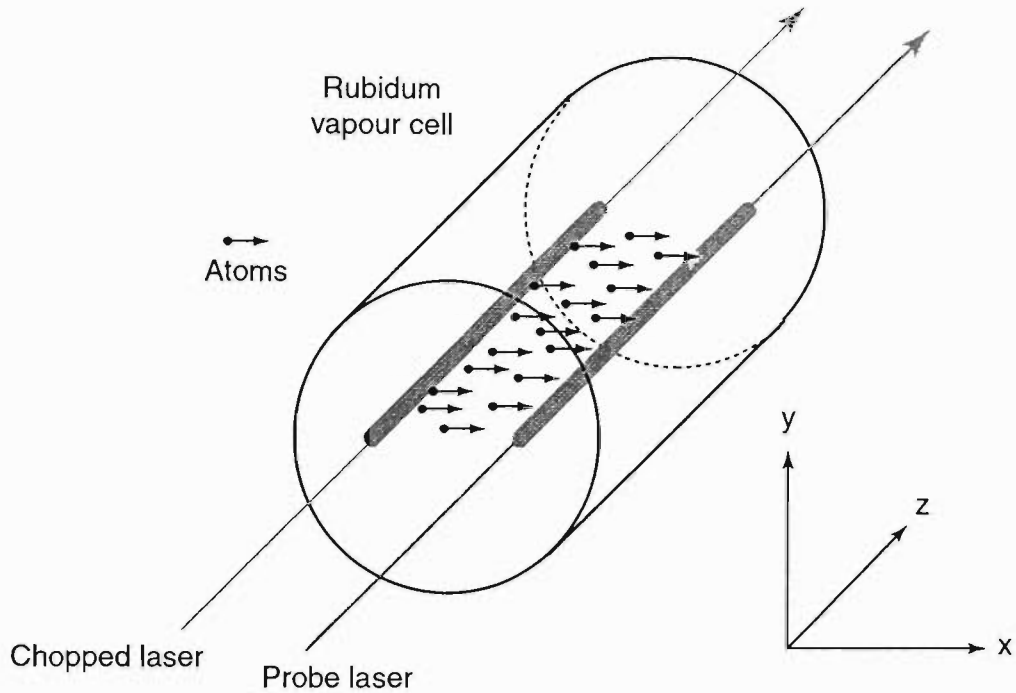
**Figure 3.2**: The vapour cell atomic beam. Atoms travelling from the chopped laser to the probe form a ribbon beam of atoms. Spectroscopic velocity selection detects only those atoms travelling perpendicular to both laser beams and these atoms constitute an atomic beam in a vapour cell.

## 3.3.1 Preliminary considerations

A rubidium vapour cell is an evacuated glass cell with several small droplets of rubidium metal placed inside. The vapour pressure of the rubidium droplets provides a low pressure gas of atoms in the cell. Atoms in the gas travel in all directions with a Maxwellian distribution of velocities. From this gas we wish to select only those atoms travelling in a specific direction. It is important then that other atoms in the cell do not interfere with the selected atoms via collisions. This means that the mean free path of atoms between collisions needs to be substantially greater than the distance between the two lasers.

At room temperature (20 °C), the vapour pressure of rubidium is approximately $2.3 \times 10^{-5}$ Pa ($1.6 \times 10^{8}$ atoms/cm$^3$) [42]. This is expected to be the main contribution to pressure in the cell. From this pressure we can calculate the mean free path,

$\lambda_{\text{mfp}}$, of rubidium atoms between collisions, given by [5]

$$\lambda_{\text{mfp}} = \frac{1}{\sqrt{2}n\sigma_0}$$ (3.1)

where $n$ is the number density of atoms, $\sigma_0 = \pi d^2$ is the total scattering cross section and $d$ is the diameter of a Rb atom, equal to 495 pm [43]. For rubidium atoms at room temperature, $\lambda_{\text{mfp}} \approx 150$ m. This is far greater than the dimensions of the cell and therefore it can be concluded that the effects of interatomic collisions will be negligible.

## 3.3.2 VCAB in $^{87}$Rb

In order to realise the VCAB in $^{87}$Rb two separate lasers of slightly different frequency were required to select and detect the desired velocity group of atoms. Figure 3.3 is a partial energy level diagram for $^{87}$Rb which shows the hyperfine transitions of the chopped and probe lasers.

The chopped laser frequency is tuned so that atoms with zero velocity component along the direction of laser propagation ($z$-axis) will be resonant on the F' = 2 to F = 2 transition. Once excited to the F = 2 state, these atoms can relax back down to either the F' = 1 or F' = 2 ground states. As resonant atoms traverse this laser field, they may experience many cycles of excitation and relaxation, after which a readily measurable number of atoms will have been optically pumped into the F' = 1 ground state. It should be emphasised at this point that only atoms moving perpendicular to the chopped laser will be excited to the F = 2 state. Atoms with a velocity component along the direction of laser propagation which Doppler shifts them out of saturated line profile, and hence will not be pumped out.

Some of the atoms which have interacted with the chopped laser will then cross the path of the probe laser. The probe laser frequency is tuned so that atoms travelling perpendicular to it (i.e. $v_z = 0$ atoms) are resonant on the F' = 2 to F = 3 transition. This is the same velocity group that was excited by the chopped laser

F = 3

267.2 MHz

F = 2

157.1 MHz

F = 1

72.3 MHz

F = 0

5P$_{3/2}$

Chopped laser          Probe laser

F′ = 2

6834.7 MHz

5S$_{1/2}$

F′ = 1
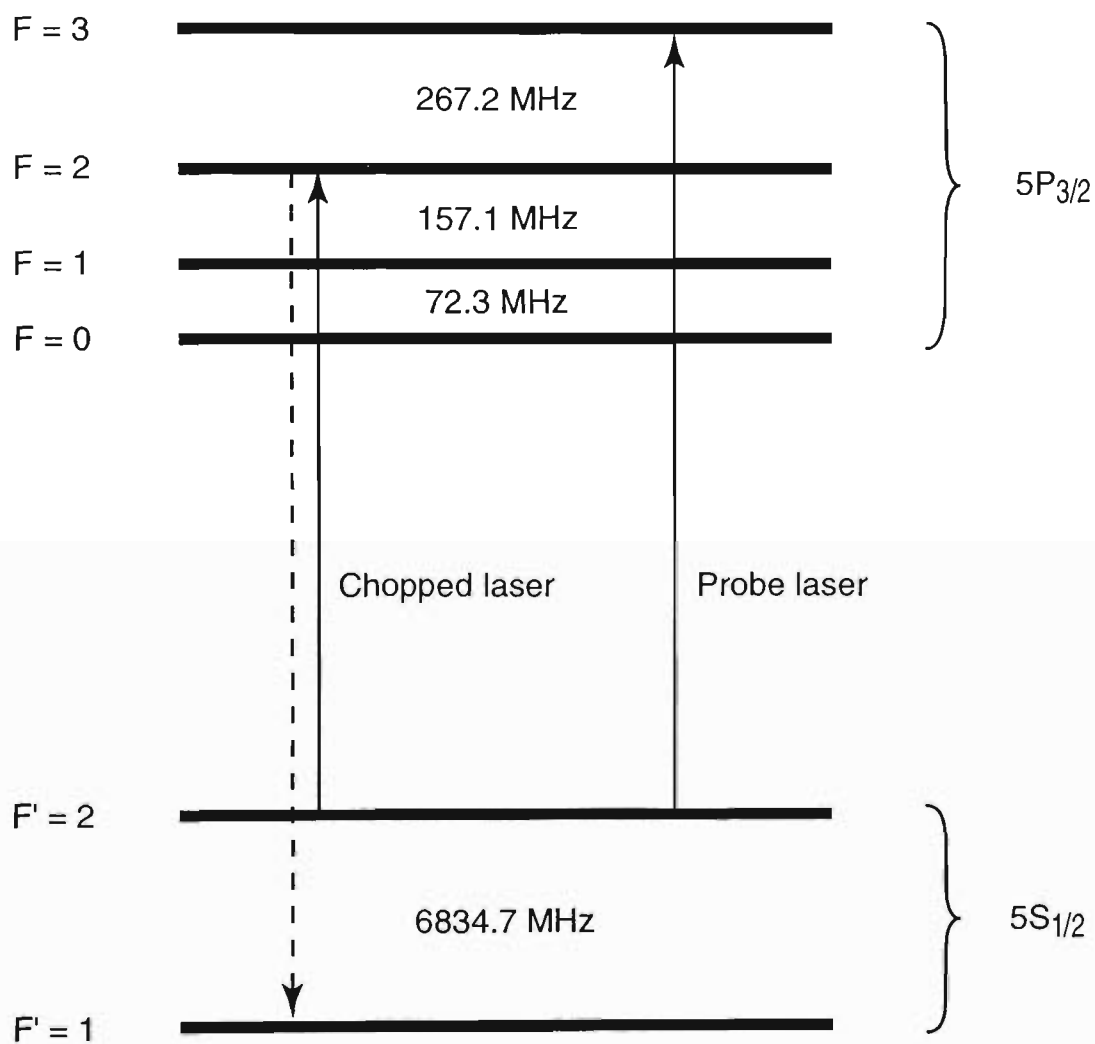
**Figure 3.3**: Partial energy level diagram of $^{87}$Rb, showing the chopped and probe laser hyperfine transitions. The chopped laser pumps atoms from the F′ = 2 ground state to the F′ = 1 ground state. The probe is tuned to the F′ = 2 to F = 3 transition and its absorption depends on the number of atoms which have been pumped by the chopped laser.

on the $F' = 2$ to $F = 2$ transition. The $F' = 2$ to $F = 3$ transition was selected for the probe because it is the strongest one available and will therefore be most sensitive to small changes in the number of absorbers. Atoms with non-zero $z$-velocities will again be Doppler shifted out of resonance with the probe.

Absorption of the probe laser depends upon the number of atoms in the $F' = 2$ ground state. Therefore any change in the population of this ground state due to the action of the chopped laser will be reflected in the absorption of the probe. The photodiode and lock-in amplifier detection system selects and amplifies features from the total photodiode signal at the frequency of the chopper, yielding a signal which only contains information about atoms which have travelled from the chopped laser to the probe.

Similar effects would be seen if the chopped and/or probe lasers were tuned to transitions from the $F' = 1$ ground state. However, transitions from the $F' = 2$ state are generally stronger, giving rise to more optical pumping and hence larger signals.

Atoms travelling with $z$-velocities such that other hyperfine transitions are Doppler shifted into resonance may also be excited by either laser (section 3.3.2.1). This leads to signals arising from other velocity groups of atoms. This makes the signal observed on the lock-in quite complicated. It can be shown however, that when the probe and chopped lasers are tuned resonant with the transitions described above, only atoms travelling perpendicular to the lasers are detected. The case when the frequency of the probe laser is scanned to detect atoms with nonzero transverse velocities is considered in section 3.3.2.2.

### 3.3.2.1 Atomic velocity groups in the VCAB with both lasers locked

First let us consider the excitations which arise from the chopped laser. Atoms travelling perpendicular to the chopped laser (ie. $v_z = 0$ atoms) will be excited to the $F = 2$ excited state. However, both the $F = 1$ and $F = 3$ levels are separated from the the $F = 2$ state by energies significantly less than the width of the Doppler profile ($\approx 510\,\mathrm{MHz}$ at room temperature). As a consequence there will still be a substantial

number of atoms with velocities that bring them resonant with the chopped laser on these other transitions.

For an atom to be excited to the F = 1 excited state, it must experience a Doppler shift, $\Delta\nu$, of 157 MHz. The Doppler shift is given by

$$\Delta\nu = kv_z \tag{3.2}$$

where $v_z$ is the velocity component of the atom in the direction of laser propagation and $k = \frac{2\pi}{\lambda}$ is the wavenumber of the light. Thus, atoms with a small range of velocities around 122 m/s in the z-plane will be excited to the F = 1 state. From there, they may relax back to either the F' = 1 or F' = 2 ground states. The result of this will be a net population transfer to the F' = 1 state similar to that which occurs for $v_z = 0$ atoms.

Atoms with a velocity of 208 m/s toward the laser (i.e. $v_z = -208$ m/s) will experience a Doppler shift of +276 MHz and be excited to the F = 3 state. However, the dipole transition selection rules ($\Delta F = 0, \pm 1$) forbid any transitions from this excited state to the F' = 1 ground state. Therefore these atoms will all relax back down to the F' = 2 state and no appreciable population transfer can be detected. However, depending on the polarisation of the lasers, there is some pumping of atoms among the ground state magnetic sublevels, which can affect the absorption of the probe. Using linearly polarised lasers (where the quantisation axis defined by the polarisation direction) atoms tend to get pumped into the middle ($m_F = 0$) magnetic substate [44]. With many of the atoms in this state the probe absorption will again be affected giving rise to a smaller signal for this velocity group of atoms.

Now that the velocity groups of atoms excited by the chopped laser have been established, let us examine which atoms will be excited by the probe. As stated earlier, the probe is tuned to the F' = 2 to F = 3 transition for atoms with $v_z = 0$ m/s. Using equation 3.2, atoms with $v_z = 208$ m/s and 330 m/s will be excited to the F = 2 and F = 1 states, respectively. Figure 3.4 shows the possible excited states accessible

to the important velocity groups of atoms.



$v_z = 122$ m/s (157 MHz)  1
$v_z = 0$ m/s (0 MHz)  2
$v_z = -208$ m/s (-267 MHz)  3

1  $v_z = 330$ m/s (424 MHz)
2  $v_z = 208$ m/s (267 MHz)
3  $v_z = 0$ m/s (0 MHz)

Chopped laser    Probe laser
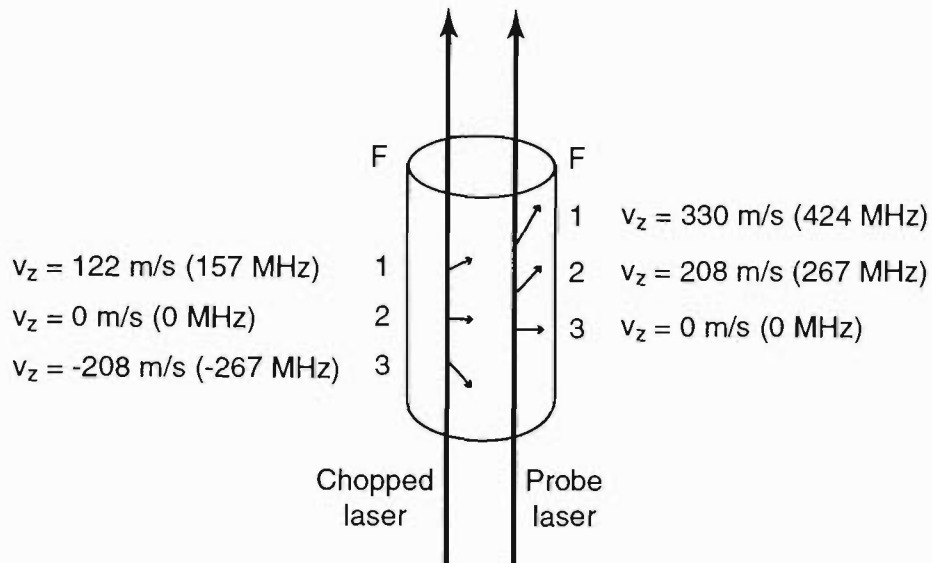
**Figure 3.4**: Atomic trajectories excited by the pump and probe lasers. The velocities given refer to the velocity groups excited to the various excited state hyperfine levels labelled

This figure shows the three velocity groups labelled, and the three velocity groups which can be detected. There is, however, only one velocity group which is resonant with both lasers and that is the $v_z = 0$ m/s group. This means that with both lasers tuned as shown in figure 3.3, the only signal that will be observed on the lock-in will be due to atoms travelling perpendicular to both lasers. With this combination of lasers then, the vapour cell atomic beam consists only of atoms travelling perpendicular to both lasers.

### 3.3.2.2 Atom velocities in the VCAB when the probe laser is scanned

With the lasers tuned as above, it is quite clear which atoms will be detectable with the lock-in. However, when the frequency of one of the lasers is scanned, other velocity groups will also contribute to the measured signal. With the chopped laser locked to the $F' = 2$ to $F = 2$ transition and the probe laser scanned over the Doppler profile, there are nine possible combinations which will give rise to observable signals. These correspond to the three velocity groups of atoms excited by the chopped laser

being detected on each of the three possible hyperfine transitions that the probe can excite.

When measuring this situation experimentally, the situation is simplified by two factors. Firstly, the relative strengths of the probe transitions are not the same. Probe excitation to the F = 3 excited state occurs far more readily than excitation to the other states. Thus the absorption on this transition yields the largest signal. Secondly, the other velocity groups of atoms are at some velocity away from the centre of the Doppler profile. Therefore, there will be fewer atoms involved, again reducing the size of observed signals for atoms on these other transitions.

### 3.3.2.3 $^{87}$Rb Results

The setup of figure 3.1 was realised with the chopped laser locked to the F' = 2 to F = 2 transition and the probe laser frequency was scanned around the F' = 2 to F = 3 resonance. The lock-in amplifier signal, recorded as a function of probe laser detuning, is shown in figure 3.5. The frequency scale was derived from the saturated absorption scan shown on the trace which had been calibrated with a Fabry-Perot spectrum analyser as in section 2.4. The intensities of the lasers were 5.0 mW/cm² and 4.5 mW/cm² for the chopped and probe lasers respectively. The laser beams were separated by 4.1 ± 0.1 mm and the spot sizes were small compared to this separation (see section 3.4 for more detail).

There are two traces shown in this figure, the top trace is a saturated absorption scan of the probe laser over the F' = 2 to F = 1, 2 and 3 states, with the hyperfine peaks labelled. This provides a reference so that the probe detuning could be precisely monitored.

The lock-in amplifier signal is given in the bottom trace. Two large peaks, occurring at probe detunings of zero and approximately 157 MHz, are clearly seen. These correspond to atoms pumped by the chopped laser via the F = 2 and F = 1 excited states respectively, being detected on the strongest probe transition (F' = 2 to F = 3). There is also a small peak visible at a probe detuning around -267 MHz.
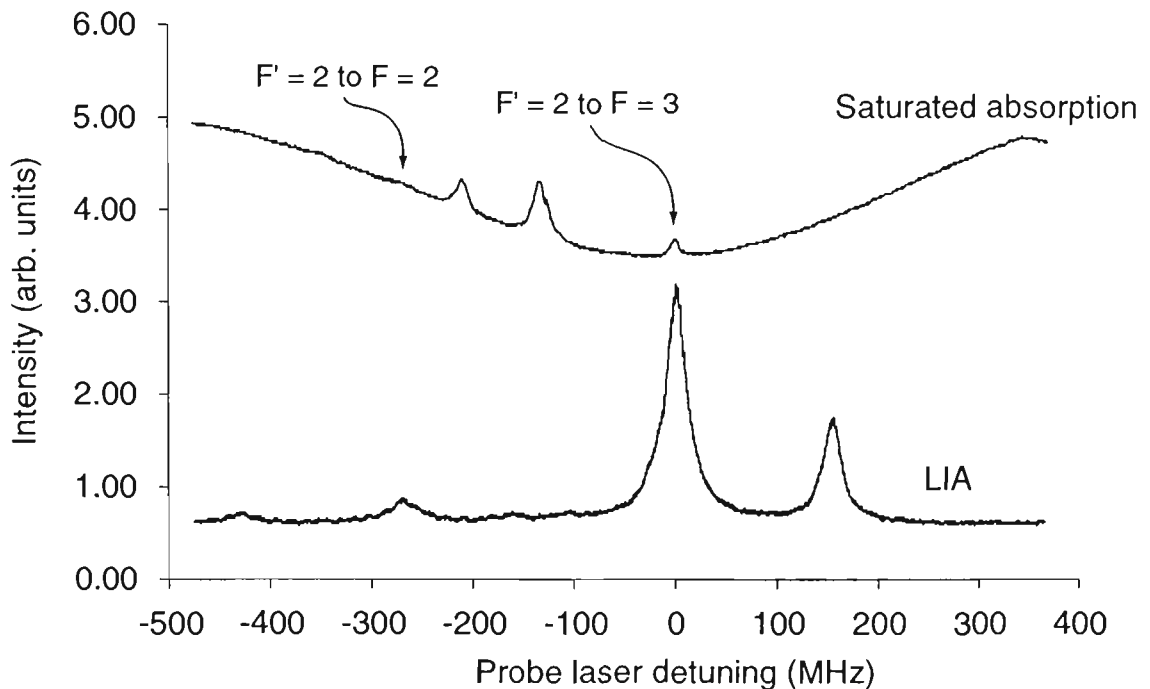
**Figure 3.5**: Plot of VCAB signal vs probe laser detuning using the apparatus shown in figure 3.1. The chopped laser was locked on the $F' = 2$ to $F = 2$ transition. Top trace shows saturated absorption scan of the $F' = 2$ to $F = 1, 2$ and $3$ levels of $^{87}$Rb. Bottom trace shows the corresponding lock-in amplifier signal.

This corresponds to chopped laser excitation on the $F' = 2$ to $F = 3$ transition and probe laser detection on this same transition.

In terms of atomic beams, these peaks represent the three different $z$-velocity groups labelled by the chopped laser (as in figure 3.4). The largest peak, at zero detuning, arises from atoms travelling perpendicular to the two lasers (ie. atoms with zero velocity component in the direction of laser propagation). The peak shifted by 157 MHz corresponds to atoms with a velocity component of approximately 122 m/s in the direction of laser propagation. The other small peak at -267 MHz is due to atoms with a velocity component at approximately 208 m/s antiparallel to the direction of laser propagation.

There are also some other peaks evident in figure 3.5 at far red (below resonance) detunings which arise from probe transitions to other excited states. These are much smaller than those due to the $F' = 2$ to $F = 3$. Peaks due to these transitions will occur with the same separation as above, but, they are shifted (to lower frequencies)

by amounts equal to the excited state hyperfine splittings, relative to the F = 3 level. That is, for probe excitation to the F = 2 excited state the set of three peaks are shifted to the left by 267 MHz and for the F = 1 excited state, the shift is 424 MHz. There are some sets of peaks which will overlap, but none overlap at zero probe detuning which is the peak of primary interest.

The peak at zero detuning represents the only situation which can truly be interpreted as an atomic beam. For instance, atoms resonant at a probe detuning of 157 MHz have a transverse velocity component, $v_z$, of 122 m/s but they may have any longitudinal velocity component, $v_x$. Therefore, the atom trajectories which contribute to the peak at 157 MHz will be moving at a range of angles with respect to the laser beams. The peak at zero detuning is the only case in which the transverse and longitudinal velocity components are independent.

### 3.3.3 VCAB in $^{85}$Rb

Until now, we have only been concerned with $^{87}$Rb atoms. The ideas described above can also be applied using the other rubidium isotope, $^{85}$Rb. The transitions to which the chopped and probe lasers are tuned are different, as shown in figure 3.6. The energy levels involved have different hyperfine quantum numbers, F, due to the different nuclear spins of the $^{85}$Rb and $^{87}$Rb isotopes, but the basic structure of the system is the same. Apart from this, and the fact that the energy levels separations are smaller in $^{85}$Rb, there is very little difference between realising the scheme in the two isotopes.

In $^{85}$Rb, the chopped laser excites atoms from the F' = 3 ground state to the F = 3 excited state. These atoms can relax back into either the F' = 3 or F' = 2 ground states. Once again, as atoms travel through the chopped laser they can experience many cycles of excitation and relaxation. After an ensemble of resonant atoms travel through the chopped laser, a significant number of them will emerge in the F' = 2 ground state. This method for labelling the desired velocity group of atoms is completely analogous to that used in $^{87}$Rb.
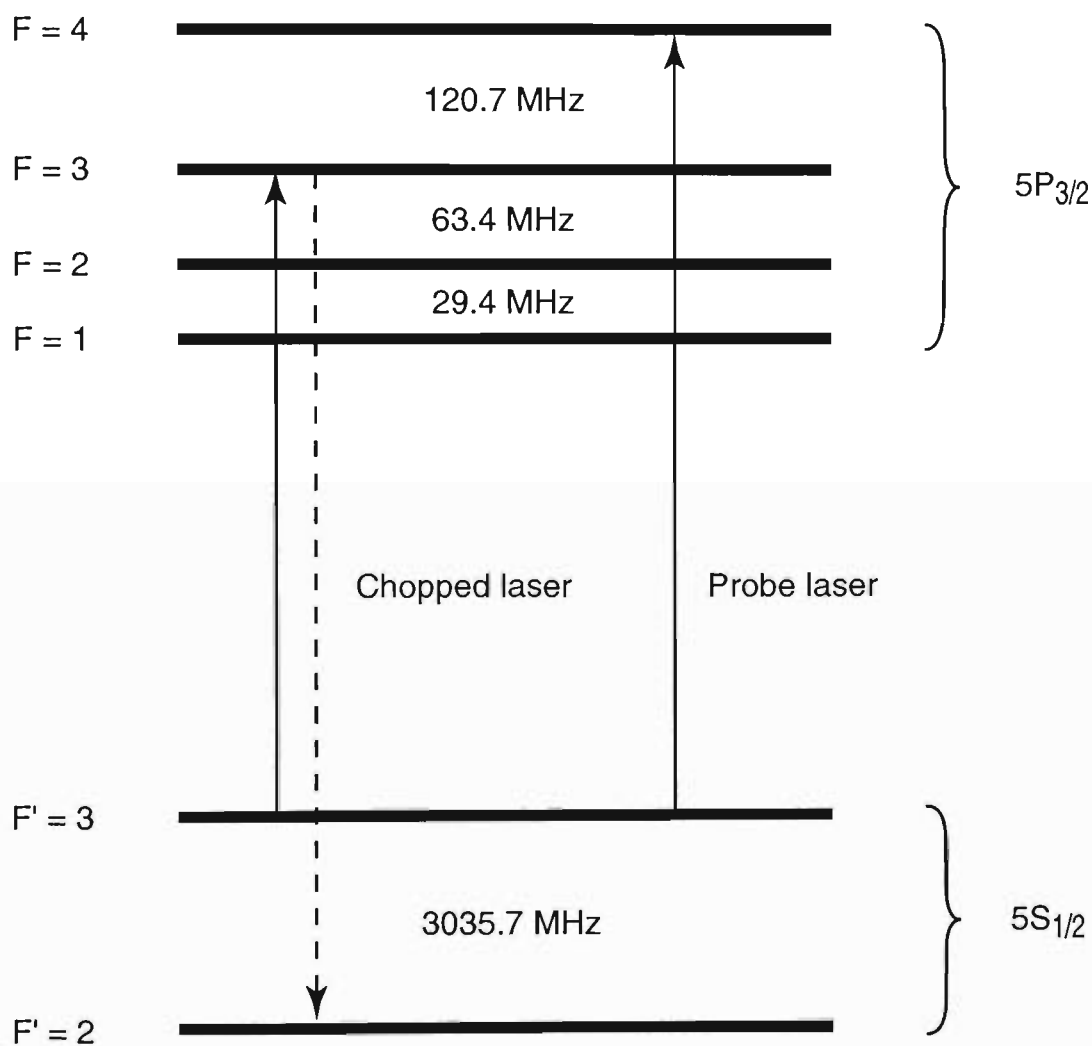
**Figure 3.6**: Partial energy level diagram of $^{85}$Rb, showing the chopped and probe laser hyperfine transitions.

Again the probe laser is tuned to the strongest transition (this time the $F' = 3$ ground state to $F = 4$ excited state transition) for maximum sensitivity. The absorption of this laser is once again monitored using a photodiode and lock-in amplifier. With these detunings, we once again detect only those atoms travelling perpendicular to the two laser beams.

If the frequency of the probe laser is scanned around resonance, then other velocity groups will be detected on multiple transitions, as before. These correspond to atoms excited on other transitions which are Doppler shifted by an amount such that they become resonant.

The experiment shown in figure 3.1 was also performed on $^{85}$Rb. Figure 3.7 shows a trace of the lock-in amplifier signal as the frequency of the probe laser was scanned around resonance, along with a saturated absorption scan for reference. This scan was obtained using the same experimental conditions as for the $^{87}$Rb scan. As can be seen, there is a large peak when the probe laser is tuned precisely to the $F' = 3$ to $F = 4$ transition. This corresponds to atoms travelling perpendicular to the lasers, excited on the $F' = 3$ to $F = 3$ transition by the chopped laser. There is also a smaller peak, at a detuning of around 63 MHz, which arises from atoms excited to the $F = 2$ state by the chopped laser. These atoms have a velocity component of approximately 47 m/s in the direction of laser propagation so that they are Doppler shifted into the $F' = 3$ to $F = 2$ resonance. The probe sees these atoms on the $F' = 3$ to $F = 4$ transition.

Another small peak at around -120 MHz probe detuning is also evident. This corresponds to the velocity group of atoms which are resonant on the $F' = 3$ to $F = 4$ transition for both the chopped and probe lasers. Once again, a small signal is expected here as some weak optical pumping among the $m_F$ sublevels still occurs.

### 3.3.4   Comparison of $^{87}$Rb and $^{85}$Rb results

Comparing the VCAB (lock-in amplifier) signals of figures 3.5 and 3.7, we can see that they contain essentially the same features, the only difference being the fre-
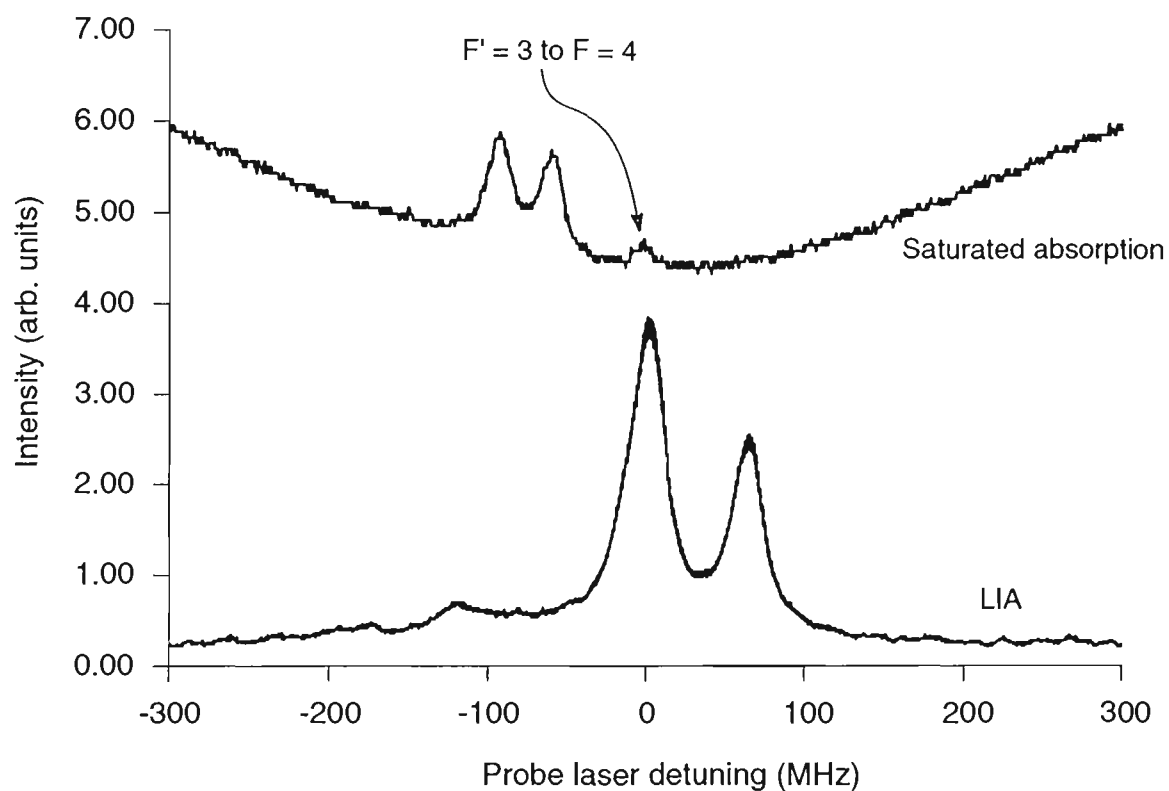
**Figure 3.7**: Plot of VCAB signal vs. probe laser detuning for the experimental arrangement of figure 3.1. The chopped laser was tuned to the $F' = 3$ to $F = 3$ transition. Top trace shows saturated absorption scan of the $F' = 3$ to $F = 2, 3$ and $4$ levels of $^{85}$Rb. Bottom trace shows the corresponding lock-in amplifier signal.

quency detunings at which the features occur.

In both traces there is a large peak at zero probe detuning corresponding to atoms with a $z$-velocity component of zero. These occur for chopped laser excitation to the second highest excited state hyperfine level and probe excitation to the highest hyperfine level. Both traces also have a smaller peak at a positive probe detuning equal to the splitting between the middle two excited state hyperfine levels. These correspond to atoms travelling away from the lasers with a Doppler shift equal to this energy difference. Similar comparisons apply to the smaller peaks at negative detunings.

One of the important differences between the two isotopes is the relative isotopic abundances of $^{87}$Rb and $^{85}$Rb. A naturally occurring sample of rubidium contains 72.17% of $^{85}$Rb and 27.83% of $^{87}$Rb [45] . This means that stronger signals will be observed using $^{85}$Rb as there are about three times more atoms. However, the peaks are better resolved for $^{87}$Rb because of the larger energy separations between the excited state hyperfine levels. Thus each isotope has its advantages.

Experiments using both isotopes are reported in later chapters. Sometimes it may be preferable to use one isotope over another but in general, what can be achieved in one can also be achieved in the other. The transverse velocity characterisation given in section 3.4 is valid for both isotopes.

## 3.4 Calculation of the transverse velocity distribution

Let us now consider only the velocity group of atoms which travel perpendicular to the two laser beams. This is the "vapour cell atomic beam" which will be used in later experiments. Essentially, this consists of a sheet of atoms moving in the $x$-direction with a Maxwellian distribution of $x$-velocities. It is also of interest to know the velocity distributions in the $y$ and $z$ planes as these define the resolution of the system. In the $y$-direction, the velocity distribution is defined by the spot sizes
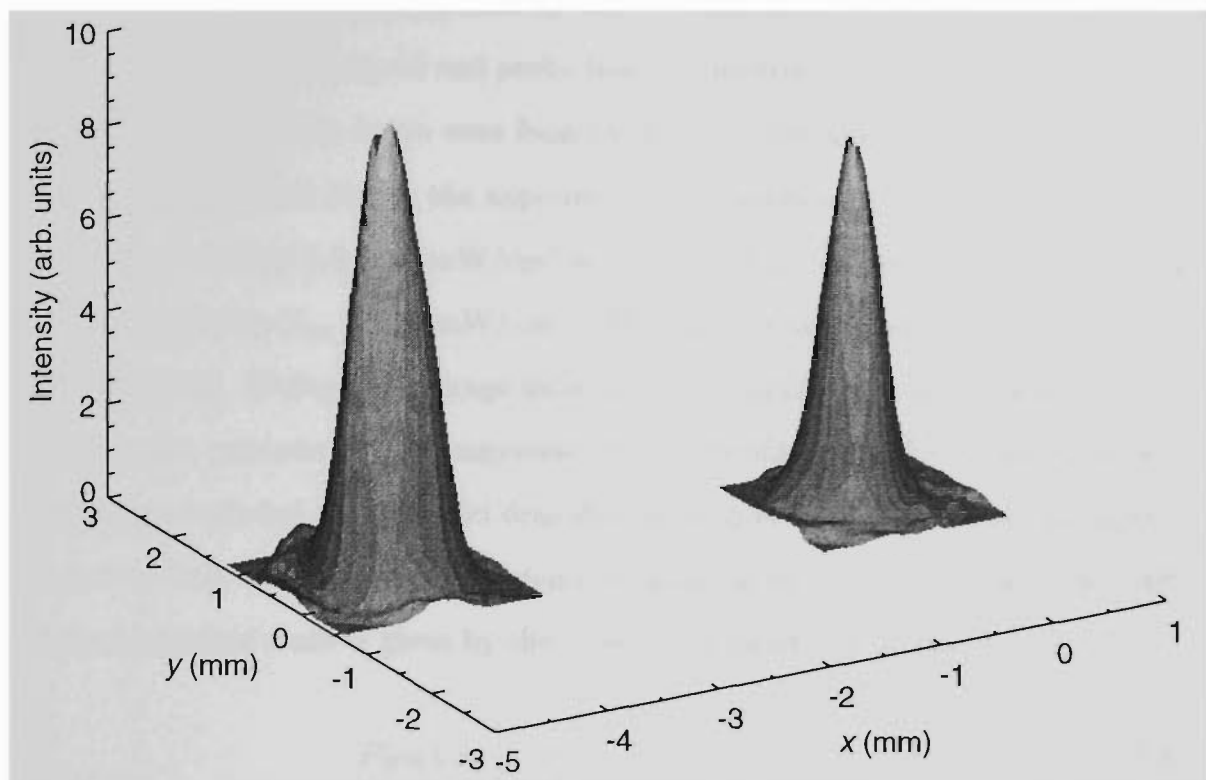
**Figure 3.8**: Plot of the spatial intensity profiles of the chopped (left) and probe (right) lasers. Probe and chopped laser powers are $34\,\mu$W and $46\,\mu$W respectively. Beam separation is $4.1 \pm 0.1$ mm.

and separation of the two lasers. In our experiments, this means that this spread of velocities will be quite large (up to $\pm 10\%$ of $v_x$) as the separation of the lasers was usually less than 10 mm and the laser spots were approximately 1 mm in diameter. In the $z$-direction however, the velocity distribution is defined by the interaction of the chopped and probe lasers with the atoms. This is determined in part by the saturated linewidths of the transitions and the resulting velocity distribution will be significantly narrower than in the $y$-direction.

In order to determine this transverse $(z)$ velocity distribution we need to know the distribution of atoms, as a function of $v_z$, that will be excited by the lasers. This is determined by the intensities of the lasers.

Spatial intensity profiles of the chopped and probe lasers, used in the experiments, were obtained using a Melles Griot Super BeamAlyser 13 SKP 003. A plot showing these profiles and their relative positions is given in figure 3.8.

The laser beams were separated by $4.1 \pm 0.1$ mm and the $\frac{1}{e^2}$ radii were 0.54 mm and 0.49 mm for the chopped and probe lasers respectively. From this, the $\frac{1}{e^2}$ area of the chopped and probe lasers were found to be 0.92 mm$^2$ and 0.75 mm$^2$. At a power of 46 $\mu$W, (measured during the experiments) the average intensity of the chopped laser $I_{Ch}$, was then $5.0 \pm 0.3$ mW/cm$^2$ which is well above the saturation intensity for this transition ($I_{sat} = 1.65$ mW/cm$^2$). This yields a saturation parameter, $G_{Ch} = \frac{I_{Ch}}{I_{sat}} = 3.0 \pm 0.2$. (Using the average intensity is a simplification which allows one to calculate an estimate of the transverse velocity profile. The full spatial intensity profiles are included in the model described in chapter 6). As saturation parameter is greater than unity, the mean probability an atom in the chopped laser field will be in the excited state is given by the power broadened Lorentzian, $P(\omega_L)$, [1]

$$P(\omega_L) = \frac{1}{2} \frac{G}{\left(4\dfrac{(\omega_L - \omega_0)^2}{\Gamma^2} + G + 1\right)} \tag{3.3}$$

where $\omega_L$ is the frequency of the laser, $\omega_0$ is the resonance frequency of the transition, $\Gamma$ is the spontaneous decay rate of the transition and $G$ is the saturation parameter. The full width at half maximum of this distribution or saturated linewidth, $\Gamma_{sat}$ is given by,

$$\Gamma_{sat} = \Gamma\sqrt{1 + G} \tag{3.4}$$

For the chopped laser then, the saturated linewidth is 12 MHz, two times the natural linewidth, $\Gamma = 6$ MHz. The laser linewidth is much narrower than this ($\approx 1$ MHz) so, when convoluted with the excitation probability, its contribution to the total width is negligible.

As the chopped laser is locked on resonance (ie. $\omega_L = \omega_0$), this mean excitation probability can also be expressed in terms of atomic velocities where the detuning

now arises from the Doppler shift, $kv_z$,

$$P(v_z) = \frac{1}{2}\frac{G}{\left(4\frac{(kv_z)^2}{\Gamma^2} + G + 1\right)} \qquad (3.5)$$

where $k = \frac{2\pi}{\lambda}$. The calculated full width at half maximum of this distribution is approximately 9.4 m/s. Figure 3.9 shows a plot of the calculated excitation probability of atom in the chopped laser field used for the experiments. As the velocity distribution of atoms is essentially flat within this range (to within 3%), this is effectively a plot of the transverse velocity distribution of atoms labelled by the chopped laser.
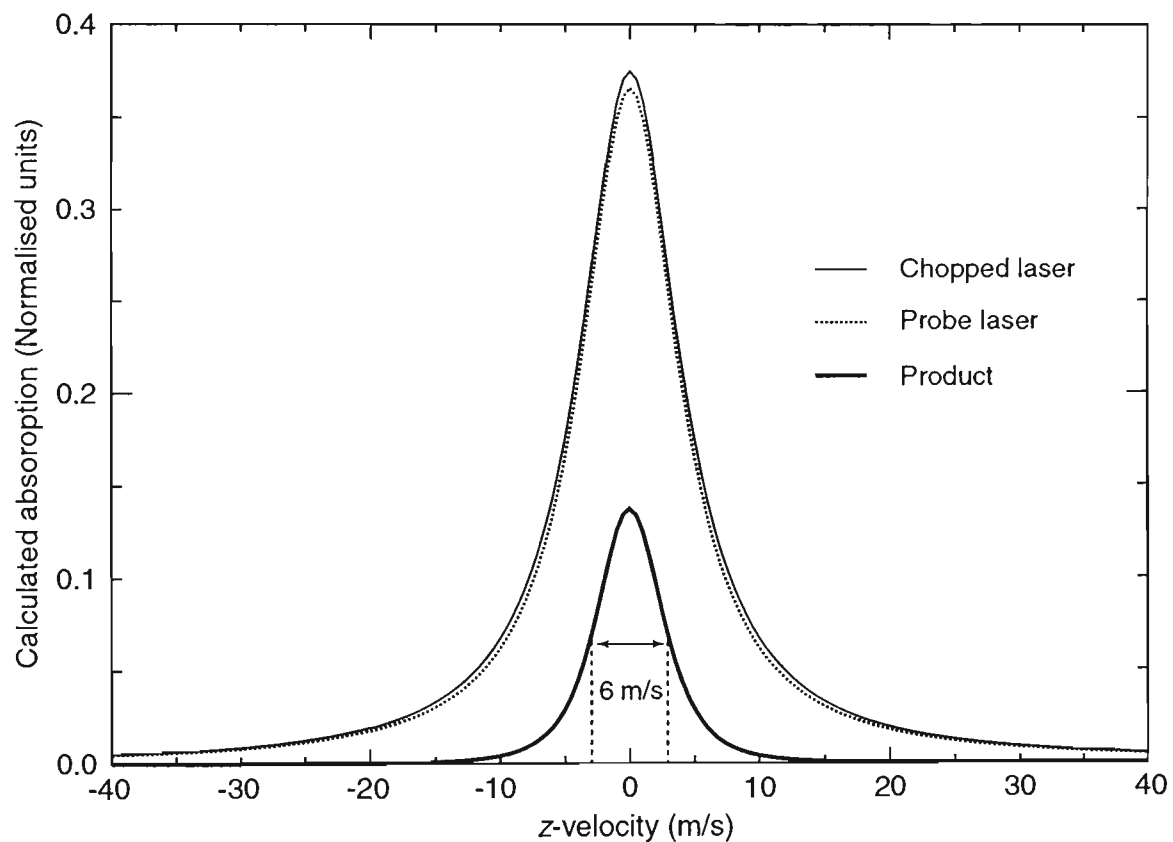


**Figure 3.9**: Excitation probability for atoms passing through the chopped and probe lasers and the product of these. The product defines the transverse velocity distribution of atoms in the VCAB and has a full width at half maximum of 6 m/s.

Next we need to consider the velocity selection of the probe laser. Its average

intensity was found, from the beam profiles, to be $4.5 \pm 0.3 \, \mathrm{mW/cm^2}$. Its velocity dependent mean excitation probability is again defined by equation 3.5 and this has also been plotted in figure 3.9. This distribution tells us the extent to which atom in the probe laser will be detected as a function of its velocity.

In the VCAB experiments which follow the frequency of both lasers will be locked to their respective transitions. As the laser frequencies are fixed, the convolution of the two distributions becomes a product and the transverse excitation probability of the VCAB will be given by the product of these two profiles (also shown in figure 3.9). As can be seen, the width of the combined distribution is narrower that the width of the individual distributions. Physically, this is because atoms which have some significant $z$-velocity component will only be labelled to a small degree and detected to a slightly lesser degree. The full width at half maximum of this profile is $6.0 \pm 0.3 \, \mathrm{m/s}$ and (as the velocity distribution of atoms this close to the centre of the Doppler profile is flat to much less than the uncertainty in the calculated width) this defines is the width of the transverse velocity distribution of the VCAB. (However, for the case where the probe laser frequency was scanned around resonance, as in figures 3.5 and 3.7, the convolution of the two distributions can not be simplified into a product as done here resulting in apparently wider peaks.)

This distribution will be used later in modelling the laser cooling experiment (chapter 6). For now though, it provides an indication of the limit to the attainable resolution of the system.

## 3.5 Discussion

The vapour cell atomic beam is, in many ways, very similar to a conventional atomic beam, in both the longitudinal and transverse directions. Unfortunately though, there are some unavoidable limitations with the vapour cell beam which means that in some situations it cannot match the performance of conventional beams.

One of the most important limitations is the transverse velocity selectivity. In

a real atomic beam, the divergence (or transverse velocity spread) of the beam can be reduced to a very small range by placing suitable apertures along the beam path after the beam exits the oven. In our system, the transverse velocity distribution is defined by the laser/atom interaction. The narrowest this can be (in the absence of any power broadening) is the natural linewidth of the atomic transition, 6 MHz for both lasers. When the contribution of both lasers is calculated, this corresponds to a VCAB velocity distribution of the beam with a minimum width of 3.3 m/s. To achieve this however, low laser power much lower than the saturation intensity would be necessary, which would decrease the number of atoms in the beam. To obtain a good signal to noise ratio ($\gg 1$), laser intensities such as those used in section 3.3 are required. This effectively limits the full width at half maximum of the velocity distribution to around 6 m/s, as calculated in section 3.4. In real atomic beam systems transverse velocity spreads are typically smaller, in some cases as low as 1 m/s. Obviously, the improved resolution of real atomic beams means that they are better suited to some types of experiments.

Another limitation of the vapour cell beam is atom flux. Rubidium atomic beams are generated from an oven which typically operates at a temperature of around 200°C. At this temperature, the number density of rubidium atoms in the beam is substantially higher (up to $10^{10}$ atoms/cm³ [46]) than what could be obtained from a source with room temperature atoms. In a room temperature vapour cell however, the vapour pressure is approximately $10^5$ lower than at 200°C. This gives an indication of the difference in number density of atoms in the two beams.

This however, is one of the main advantages of the VCAB as we have a room temperature atomic beam without needing an oven. Conversely, if the cell was heated, the number of atoms in the VCAB could, in principle, approach that of a normal beam. Two factors become important though when heating the cell and these are excessive absorption and lowering the mean free path of atoms in the cell.

The first of these factors arises because the increased number of atoms in the cell can absorb almost all of the laser light and atoms at the end of the cell will experience

essentially no labelling or detection. In a cell 75 mm long, this becomes important when the temperature exceeds 40°C as over 90% of the light will be absorbed along the length of the cell [47]. Therefore, we are restricted to operating at temperatures below 40°C.

The second factor arises because the mean free path of atoms between collisions is inversely proportional to the increase in the number of atoms per unit volume in the cell. Collisions between atoms in the beam and background atoms will interfere with the VCAB. However, provided the mean free path stays substantially larger than the distance between the chopped and probe lasers we would not expect to run into any problems.

In order to quantify this, let us assume that the temperature at which the mean free path becomes equal to the separation between the laser beams (say 10 mm) is the limiting condition. A maximum allowable cell temperature can then be calculated using equation 3.1. The mean free path of Rb atoms, $\lambda_{mfp} = 10$ mm, at a temperature of 150°C. For temperatures below this, problems due to atomic collisions should not arise in a VCAB less than or equal to 10 mm in length. With our vapour cells then, the primary limitation to the maximum operating temperature is always going to be due to excessive absorption.

Another of the limitations of the VCAB system is that the length of the atomic beam is restricted. Obviously, the beam can not be any larger than the dimensions of the cell. The cells use in our experiments prevented us from extending the beam beyond 20 mm. With custom designed cells however, it should be possible to extend the length of a VCAB up to at least 10 cm.

A final restriction on the length of the VCAB is related to the speed of the chopper. The higher the frequency of the chopper, the shorter the VCAB must be. First, consider the case when the chopper is open. If the chopped and probe lasers are separated by a distance of 10 mm, then at T = 20°C, the average time an atom will take to travel from one laser to the other is 37 μs. In a typical experiment, the chopper operates at approximately 2 kHz, meaning that the chopped beam will be

on for a time of 500 $\mu$s before it will be off for the same time. This case is fine as the majority of atoms which are labelled when the chopper is open will arrive at the probe laser before the chopper blocks the (chopped) laser beam again.

If however, the separation of the two lasers is increased such that the average time taken for atoms to travel between the two lasers exceeds the period of the chopper, then the labelling will be lost. This is because the Maxwellian spread of velocities will cause the labelled and unlabelled atoms to overlap, and the phase relation between them will smear out by the time they reach the probe. Fortunately though, for the chopper frequency used here (2 kHz), this occurs at a beam separation of 135 mm so this is not important in our situation. The further the beams are apart, the more smeared the signal becomes due to the Maxwellian velocity spread. To overcome this it would be necessary to reduce the frequency of the chopper and lock-in to allow for the longer atom travel time.

## 3.6 Conclusions

In this chapter it has been shown that atoms with particular velocities can be selected and measured from within a gas in a vapour cell. Two lasers were used to velocity select atoms in two dimensions, creating an atomic beam in a vapour cell. The beam is actually a ribbon of atoms with a Maxwellian velocity distribution in the direction the beam and has a $6.0 \pm 0.3$ m/s wide transverse velocity distribution. This scheme could be used to select velocity groups of atoms from any part of the transverse Doppler profile. For our applications, however, we wish to study the velocity group centred around $v_z = 0$.

Now that the vapour cell atomic beam has been realised, there are some interesting applications to follow. Firstly, we will show that when the chopped laser is used to spin polarise atoms, we can measure the Larmor precession of these atoms in a magnetic field, as they travel to the probe. Finally, the VCAB will be used to study one dimensional laser cooling.

# Chapter 4

# OBSERVATION OF LARMOR PRECESSION
# USING THE VCAB

In the previous chapter it was shown that an atomic beam can be created, in a sealed vapour cell, by measuring atoms which travel between two adjacent laser beams. In order to demonstrate the usefulness of this system it was applied to measurements which generally require a conventional atomic beam. One such measurement is the time evolution of the internal state of atoms as they travel from one laser to the other. As an example of this, the vapour cell atomic beam has been used to measure the Larmor precession of atoms in a magnetic field and this is described in the present chapter.

The chapter begins with a brief introduction to Larmor precession and review some of the previous work in the area. This is followed by a description of the scheme we used to observe Larmor precession. Theoretical predictions of the expected signals, as a function of magnetic field, are calculated and experimental data is then obtained and compared with the theory.

## 4.1   Background and review

The interaction of polarised resonant light with atoms can create an alignment or orientation of the magnetic moment of the atoms [48]. Light carries angular momentum which can be transferred to atoms via absorption. This leads to optical pumping of atoms into particular excited and ground state magnetic sublevels.

In 1924 it was shown by Hanle that the absorption of polarised resonance light

can produce high degrees of polarisation in the excited states of atoms [49]. This was demonstrated through the depolarisation of resonance fluorescence in the presence of an external magnetic field.

It was not until 1950, however, that Kastler demonstrated that the absorption and re-emission of resonant light could also lead to polarisation of atomic ground states [50]. He proposed that a non-uniform distribution of populations over the magnetic sublevels of an atomic ground state could be created by optical pumping methods. This idea was realised experimentally soon after by Brossel *et al.* who observed ground state polarisation, caused by optical pumping [51].

Further developments and progress in optical pumping were soon to follow. In 1957, Dehmelt [52, 53] showed that the intensity of polarised resonance light transmitted through a sodium vapour cell could be amplitude modulated by applying a radio frequency (rf) magnetic field to the cell. Strong modulation of the transmitted light was observed when the frequency of the applied rf signal was equal to the Larmor precession frequency, $\omega_L$ given by [54]

$$\omega_L = \frac{g_F \mu_B}{\hbar} B = \alpha B \tag{4.1}$$

where $g_F$ is the Landé $g$-factor of the hyperfine level F, $\mu_B$ is the Bohr magneton, $\hbar$ is Planck's constant on $2\pi$ and $B$ is the magnetic field.

Applying an rf field induces transitions between the magnetic sublevels of the ground state of atoms provided that the frequency of the applied rf signal matches the energy (frequency) separation of the magnetic sublevels. This separation, or Zeeman splitting, is dependent on the magnetic field the atoms experience.

A similar modulation of the resonance fluorescence was predicted [55] for atoms excited by resonant light and an rf field (at the Larmor frequency) and observed in cadmium around the same time [56]. This follows from the work of Dehmelt [52, 53] in that a modulation in the absorption will also show up in the fluorescence provided the frequency of the modulation is sufficiently smaller than the lifetime of

the excited state.

It was these principles that lead to the development of the first alkali metal magnetometers [57]. Essentially, these devices measured the frequency at which atoms precessed by monitoring the frequency of the applied rf signal required to induce a modulation of transmitted (polarised) resonance light.

In 1969 Dupont-Roc *et al.* reported the detection of extremely narrow zero-field level crossing resonances in $^{87}$Rb [58]. Their experiment was similar to a Hanle effect level crossing experiment [49], however, it was performed using the ground state of optically pumped Rb atoms. With sophisticated magnetic shielding and detection schemes, they were able to detect fields as low as $3 \times 10^{-14}$ T. This work, and the previously discussed reports, demonstrated the sensitivity of oriented atoms to magnetic fields and the usefulness of being able to accurately measure an atoms response to magnetic fields.

New ways of observing the orientation and precession of atoms are still being reported, for example Wäckerle, *et al.* used pulsed optical excitation to measure ground state spin coherence of $^{85}$Rb and $^{87}$Rb with kilohertz resolution [59]. Optical pulses were used to magnetise the atoms which were then probed by another (cw) laser. A polarisation sensitive detection scheme was used to measure the precession of the induced magnetisation. These ideas have been extended to detect precession between spatially separated lasers [41] as described in section 3.1.

A further development has been realised by Isayama *et al.* who have observed Larmor precession of laser-cooled Rb atoms in a magnetic field. By measuring paramagnetic Faraday rotation of linearly polarised light as it passed through cold ($10\,\mu$K) polarised atoms, they were able to determine the field strength with a precision of $1.8 \times 10^{-11}$ T. This report also proposes the usefulness of this technique for magnetometer applications.

A great many authors have studied the effects of magnetic fields on atoms and the reader is referred to [48, 60] for a general overview. This review will now focus on work which relates more closely with the experiment performed in this chapter;

the study of polarised atoms precessing in a magnetic field between two spatially separated lasers.

In 1974, Schieder and Walther reported a study of optically pumped sodium in which they observed the precession of spin polarised atoms in an atomic beam [61]. Their experiment involved pumping atoms at one point in the beam and probing them (measuring the fluorescence) at another point downstream. A circularly polarised pump laser, tuned on the $F' = 2$ to $F = 1$ $D_1$ transition, was used to polarise the atoms by optically pumping them into an extreme ground state magnetic sublevel ($m_F = +2$) of the $F = 2$ ground state. The probe laser was also tuned to the $F' = 2$ to $F = 1$ transition with the same handed circular polarisation. Atoms in the $m_F = +2$ substate were non-excitable by the probe, as there is no $F = 1$ excited state which can accept the additional angular momentum. Thus atoms in this state at the probe laser would not be excited and not produce fluorescence.

As atoms travelled from the pump to probe regions, they were subjected to a (variable strength) magnetic field which caused the atomic polarisation to precess. When the field was zero, the atoms were seen to remain in the $m_F = +2$ state as indicated by the small amount of fluorescence induced by the probe. As the field was increased, the atoms precessed out of the $m_F = +2$ state through the other magnetic sublevels and this led to an increase in the fluorescence at the probe. With further increases in the magnetic field, the fluorescence intensity was seen to cycle, following the precession of the polarisation of atoms in the beam. At larger fields, the cycling became obscured because of the spread of velocities in the beam.

Several years after this, Nakayama *et al.* reported a similar experiment using polarisation spectroscopy to measure the precession of sodium atoms as they travelled between two spatially separated laser beams in a vapour cell [39]. This work has been mentioned previously (section 3.1) but is worth elaborating on here as it relates closely to the present work. In their experiment, sodium atoms were spin polarised by a circularly polarised pump laser using the $F' = 2$ to $F = 1$ $D_1$ transition as in [61]. The polarisation rotation of a spatially separated probe laser (caused by

interaction with spin polarised atoms) was recorded as a function of magnetic field. Maximum rotation of the probe polarisation was observed at zero field, when the largest number of polarised stoms reached the probe. As the field was increased, the probe transmission varied periodically (and decayed strongly due to the velocity spread) with magnetic field, following the precession of the atoms.

In 1991, Théobald and coworkers performed an experiment on a caesium atomic beam in which they measured Ramsey-type resonances arising from ground state Zeeman coherences [62]. Two linearly polarised, laser beams intersected an atomic beam $34.5$ cm apart. The first laser, the pump, was tuned to the $F' = 3$ to $F = 2$ transition and created the ground state coherences ($\Delta m_F = \pm 2, \pm 4$ and $\pm 6$). These atoms then evolved at the Larmor frequency as they travelled to the probe. The probe laser was tuned to the same transition and the resulting fluorescence was monitored on a photodiode. The fluorescence was recorded as a function of the applied magnetic field and the precession of the atoms gave rise to similar signals as were observed in the two previously discussed reports.

Another report describing the observation of ground state coherences in a rubidium atomic beam was given by Schuh *et al.* in 1993 [63]. Spatially separated lasers were again used and the pumping and detection regions were $50$ mm apart. The coherences were induced by pumping on the $F' = 3$ to $F = 4$ $D_2$ transition in $^{85}$Rb. They were probed downstream, by another laser beam, on the same transition. A major difference of this experiment to the others was that the magnetic field was oriented in the same direction as the lasers. They observed dispersively shaped Ramsey fringes as the magnetic field was scanned around zero. A sensitivity to changes in the magnetic field of $3.7 \times 10^{-11}$ T$/\sqrt{\text{Hz}}$ was observed.

In a recent study on spin echoes in a lithium beam, Zielonkowski *et al.* observed spin precession of atoms between circularly polarised pump and probe lasers [64]. The lasers were $40$ cm apart and the magnetic field was applied perpendicular to both the laser propagation and atomic beam directions. Their results displayed a similar sensitivity to those reported in [63], however, they went on to demonstrate

that an echo in the spin signal could be detected by introducing a third circularly polarised laser between the pump and probe.

These reports described in the last few paragraphs each measure essentially the same phenomena that we will study with the vapour cell atomic beam. All of these experiments, with the exception of [39], were performed in a conventional atomic beam. Later in the chapter, a more detailed look at the results of the above studies is provided, along with a comparison to the present results.

## 4.2 Current scheme

In order to study the Larmor precession of atoms with the vapour cell atomic beam, the chopped laser was used to polarise atoms and the probe laser used to measure the polarisation state of these atoms after travelling through a region of constant magnetic field. With the quantisation axis along the direction of laser propagation ($z$-direction, see figure 4.1), both lasers where circularly polarised ($\sigma^+$) so that only excitations in which $\Delta m_F = +1$ could occur (figure 4.2). Resonant ($v_z = 0$) atoms which pass through the chopped laser were excited on the $F' = 3$ to $F = 4$ hyperfine transition. Once excited, atoms may relax back to the $F = 3$ ground state with $\Delta m_F = -1, 0$ or $+1$. As atoms traversed the chopped laser, they experienced many cycles of excitation and relaxation. This time however, very few are lost to the other ($F' = 2$) ground state as relaxation to this state from the $F = 4$ excited state involves $\Delta F = -2$, making it a non-allowed dipole transition.

After many cycles of excitation ($\Delta m_F = +1$) and relaxation ($\Delta m_F = 0$, $\pm 1$) a net shift of the ground state population to extreme (high) $m_F$ values will occur (figure 4.2). This means that after an ensemble of atoms have passed through the chopped laser, a large number of them occupy the $m_F = +3$ state, indicated by the shaded region. These then evolve at the Larmor frequency, on their journey to the probe laser.

The probe was tuned to the $F' = 3$ to $F = 3$ transition with the same handed
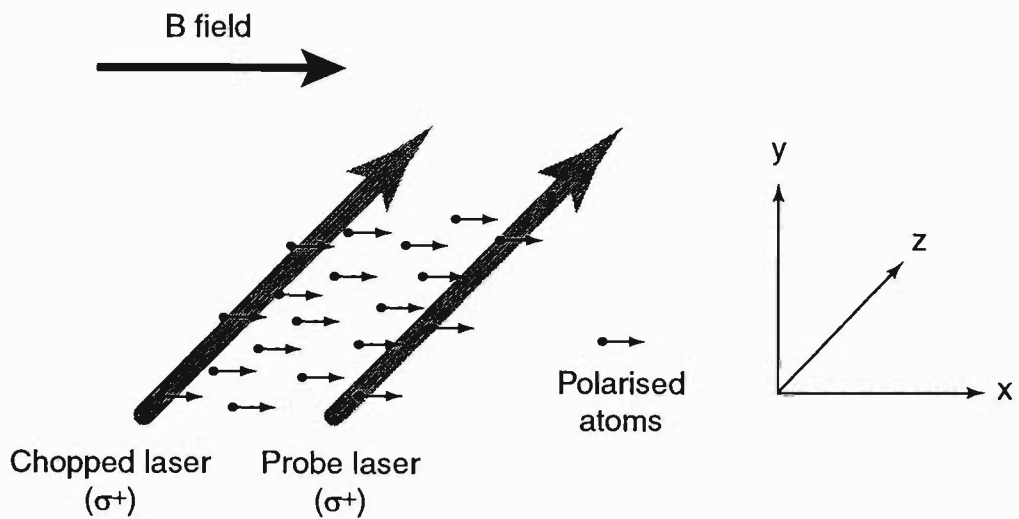
**Figure 4.1**: Basic arrangement of the Larmor precession measurement. The chopped laser polarises atoms which precess in the applied field. The polarisation state of the atoms when they reach the probe determines how much the probe will be absorbed.
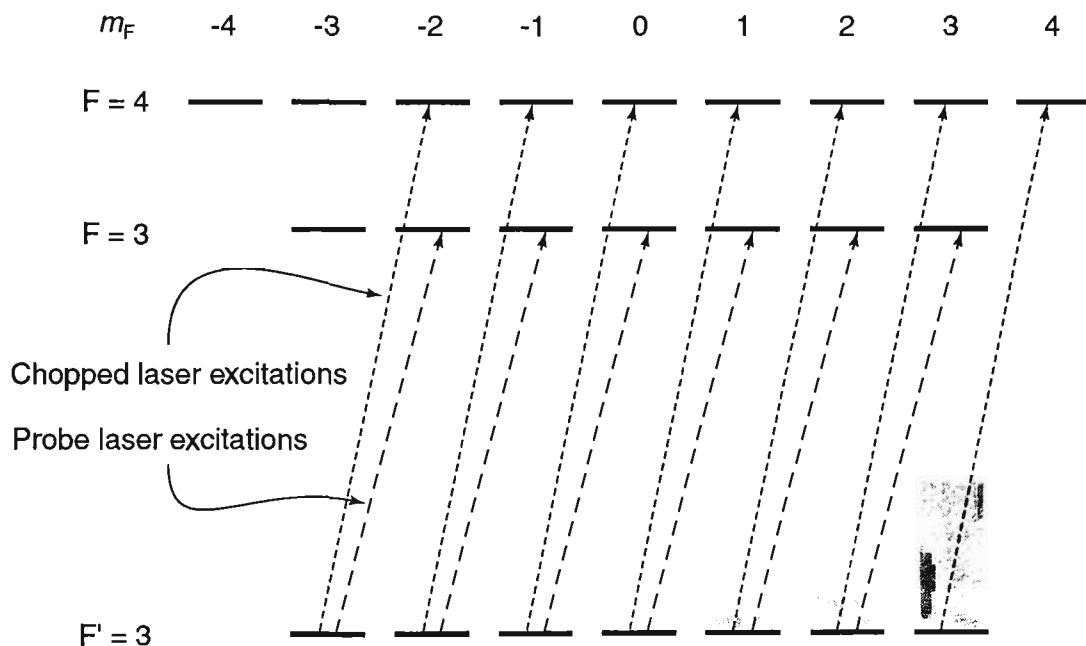


**Figure 4.2**: Partial energy level diagram of $^{85}$Rb showing the hyperfine transitions of the chopped and probe lasers. Both lasers are circularly polarised so only $\Delta m_f = +1$ excitations can occur. The shaded regions indicate where atomic populations accumulate after interaction with the lasers.

circular polarisation as the chopped laser figure 4.2. All of the magnetic substates, apart from the $m_F = +3$ state, can absorb probe radiation. Atoms in the $m_F = +3$ do not absorb any light as there is no $F = 3$ excited substate which can accept the additional angular momentum of the probe, so atoms in this state are transparent to the probe.

Atoms pumped into the $m_F = +3$ state by the chopped laser will remain in that state provided they are not perturbed. If the atoms are perturbed by a magnetic field, perpendicular to the quantisation axis $(z)$, they will precess around this field, resulting in Zeeman transitions to other ground state sublevels. Thus, in the absence of a magnetic field, we would expect the probe to be transmitted by the polarised atoms. As the magnetic field is increased we would expect the transparency to be destroyed. If all atoms in the VCAB travelled with the same velocity, the transparency should return after one (or more) complete precession cycle(s). However, because the atoms travel with a Maxwellian distribution of velocities, they take a range of different times to reach the probe and the polarisation will become obscured by the velocity dispersion.

## 4.3 Theoretical description of Larmor precession experiment

When a spin polarised atom is placed in a magnetic field, the magnetic moment of the atom will precess around the field at the Larmor frequency, $\omega_L$. The precession frequency is dependent on the strength of the magnetic field and is given by 4.1. In $^{85}$Rb the constant, $\alpha$, is 4.66 GHz/T.

In the current experiment, the lasers are separated by a distance $d$ and atoms travel at speed $v$ through a region with magnetic field $B_x$ oriented along the $x$-axis. Assuming $B_x$ is constant across the distance between the lasers and that $B_y$ and $B_z$

are zero, the precession angle $\phi$ is given by [64]

$$\phi = \frac{g_F \mu_B}{\hbar} \frac{B_x d}{v} = \alpha \frac{B_x d}{v}$$  (4.2)

where $\frac{d}{v}$ is simply the time taken for atoms to travel between the lasers. The absorption of the probe is dependent upon $\cos\phi$ (see appendix C for the derivation of the cos dependence in the case of a $J = \frac{1}{2}$ ground state).

Atoms travel from the chopped laser to the probe with a range velocities, $v$, given by the Maxwellian distribution [5]. In a vapour cell, this distribution, $N(v)dv$, is given by 4.3,

$$N(v)dv = \frac{4}{\sqrt{\pi}\tilde{v}^3} v^2 \exp\left(-\frac{v^2}{\tilde{v}^2}\right) dv$$  (4.3)

where the most probable speed, $\tilde{v}$ is given by,

$$\tilde{v} = \sqrt{\frac{2k_B T}{m}}$$  (4.4)

and $k_B$ is Boltzmann's constant, $T$ is the temperature of the gas and $m$ is the mass of the atoms.

As a first approximation, we assume that the chopped laser completely polarises all atoms which pass through it, irrespective of the time spent in the laser field. At the probe laser the observed magnetic moment $M(B_x, d)$ can be expressed as a function of the magnetic field and laser separation. This will be proportional to the integral over all velocities, of the velocity distribution, $N(v)dv$, multiplied by the cosine of the precession angle for each velocity.

$$M(B_x, d) \propto \int_0^\infty v^2 \exp\left(-\frac{v^2}{\tilde{v}^2}\right) \cos\left(\alpha \frac{B_x d}{v}\right) dv$$  (4.5)

This integral has been evaluated and is plotted in figure 4.3. On the vertical axis is the expected magnetic moment of the ensemble of atoms arriving at the probe. This is plotted against the normalised (dimensionless) magnetic field, $B/B_0$, where $(2\pi \times) B_0$ is the field which gives one full rotation for the most probably speed and

is given by $\frac{\bar{v}}{\alpha d}$.
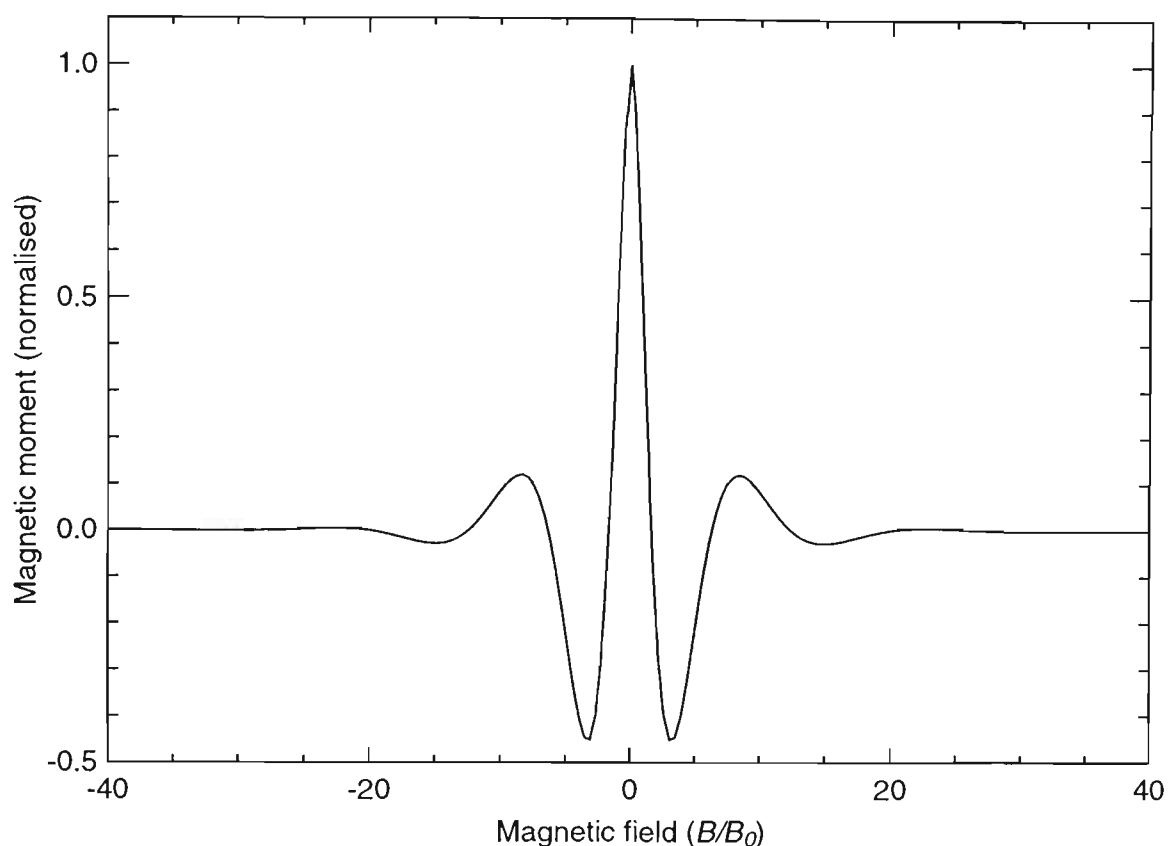


**Figure 4.3**: Calculated magnetic moment of atoms after travelling from the chopped laser to the probe. The magnetic moment is plotted against the normalised (dimensionless) magnetic field $B/B_0$ where $B_0 = \frac{\bar{v}}{\alpha d}$.

This curve describes the shape of the features we expect to observe experimentally. The most notable feature is the large central peak in the magnetic moment which corresponds to complete polarisation of the ensemble in zero magnetic field. The full width at half maximum (FWHM) of this peak is $2.48\,B_0$.

As the magnetic field is increased, the polarisation begins to rotate and the observed magnetic moment oscillates, with a strong decay. This decay is due to the velocity dispersion of the atomic beam. If atoms in the beam all travelled at the same velocity, sinusoidal oscillations of the magnetic moment would be observable at higher fields. However, as there are atoms with many different velocities in the beam, they each take different amounts of time to reach the probe. Thus they each have

different amounts of time to precess, so that the slower atoms will have precessed more than fast atoms. Once the field is strong enough so that one precession period becomes comparable to the time taken for atoms to reach the probe, the polarisation becomes blurred by this velocity dispersion. With further increases in the field strength, all evidence of the atomic polarisation is lost and the polarisation of atoms arriving at the probe returns to essentially random.

It is not immediately obvious from figure 4.3 but the width of the central feature is dependent upon several factors. Firstly, both the velocity of the atoms and the distance between the two laser beams determine the time atoms have to precess. If the (mean) velocity of the atoms is decreased (for example by decreasing the temperature) or the laser beams are moved further apart, the central feature would become narrower as the atoms would have a longer time to precess. Secondly, if the Landé $g$-factor, $g_F$, changes (as it will for different species), the value of $\alpha$ will also change, again altering the width of the central peak.

## 4.4 The Larmor precession experiment

A diagram of the arrangement used for the Larmor precession experiment is given in figure 4.4. The chopped and probe lasers travel parallel to each other through a rubidium vapour cell. Both lasers pass through a linear polariser and quarter wave plate (oriented at 45° to the axis of the linear polariser) to create the two circularly polarised beams of the same handedness. The lasers were tuned as in figure 4.2 and the distance between the two lasers was varied over the range 3 mm to 12 mm. Three orthogonal Helmholtz coil pairs were used to cancel the earth's magnetic field (only one set of coils is shown in the figure). A magnetic field, $B_x$, was then applied perpendicular to the quantisation axis (the direction of laser propagation) and in the direction of the VCAB, and varied over the range $\pm 40\,\mu$T.

The probe transmission was measured on a photodiode and sent to a lock-in amplifier tuned to the frequency of the chopper. A plot showing the normalised
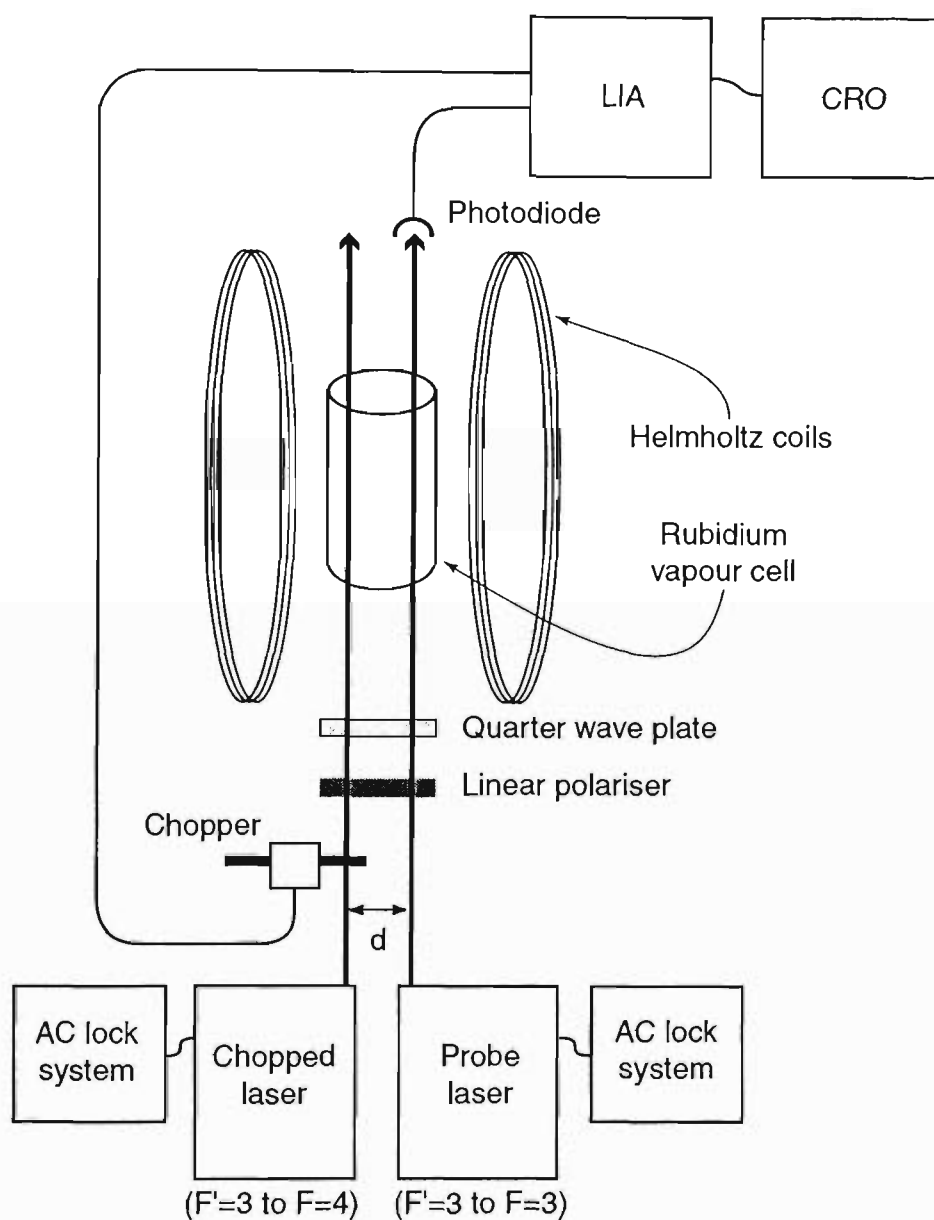
**Figure 4.4**: Experimental arrangement used to observe Larmor precession. d is the distance between the two laser beam. Only one of three orthogonal pairs of Helmholtz coils is shown.

lock-in signals, as a function of the applied magnetic field, is given in figure 4.5. Laser beam separations are given in the inset. Normalisation was performed by dividing all data points of each scan by the largest signal for that lsaer separation. This was so that all data sets could be viewed on the same scale. The laser intensities used were 30 ($\pm$ 5) mW/cm$^2$ and 12 ($\pm$ 2) mW/cm$^2$, for the chopped and probe lasers, respectively.
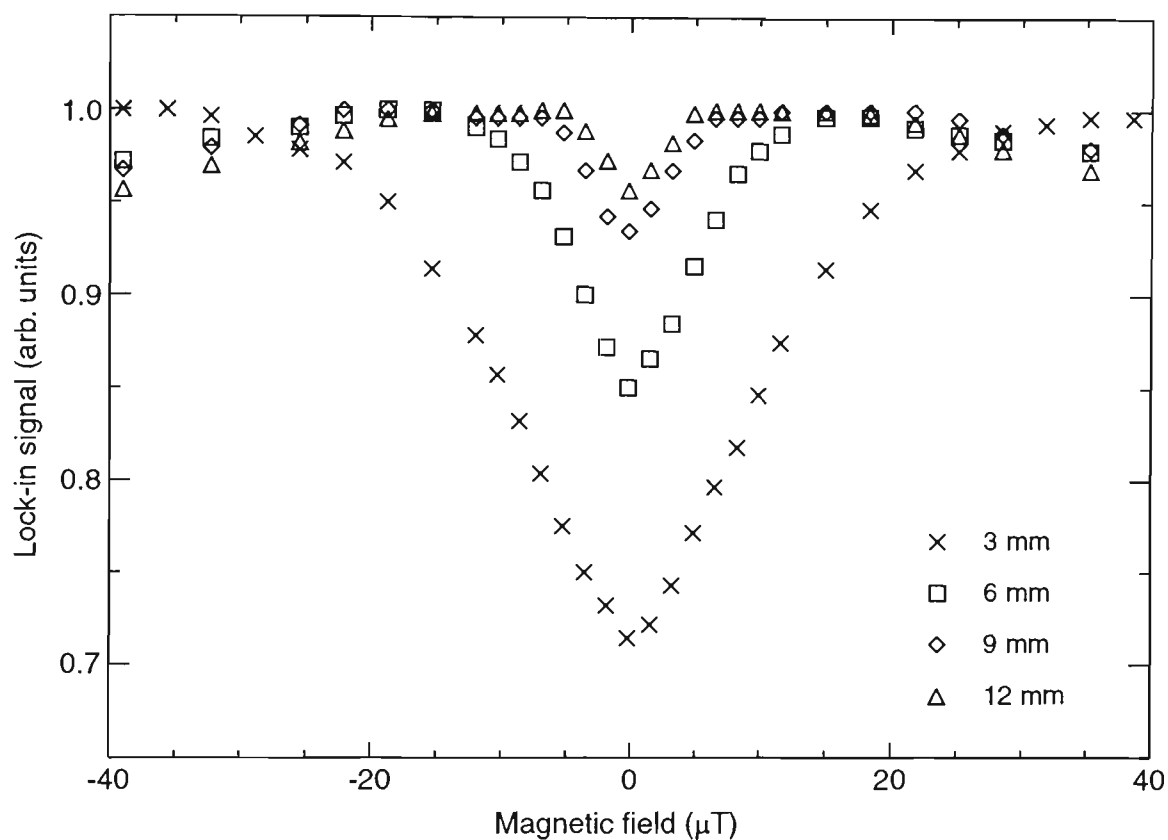


**Figure 4.5**: Normalised lock-in amplifier signal as a function of applied magnetic field for the laser separations listed on the plot.

A large central valley in all of the lock-in signals is evident around zero magnetic field. This feature becomes both narrower and more shallow, as the laser separation increases. These central valleys arise from atoms which retain their polarisation induced by the chopped laser upon reaching the probe. They appear as valleys (not peaks as in the theory) because of the phase setting of the lock-in which was chosen to maximise the measured signal.

The narrowing in width, at larger separations, occurs because atoms which travel longer distances have more time to precess out of their initial states. Therefore, smaller fields are required to induce a detectable precession. The decrease in valley depth however, is not predicted by the theory but is believed to be due to magnetic field non-uniformities across the cell. Measurements of the field uniformity indicated that, under normal experimental conditions, the magnetic field could vary by up to $2\,\mu T$ along the length of the vapour cell.

In order to compare these results to the theory, it is useful to plot the experimental data against the normalised magnetic field, $\frac{B}{B_0}$, as in the theoretical section. This has been done for each beam separation and the plots are given in figure 4.6. Also plotted is an appropriately scaled theoretical curve for comparison. The theoretical curves have been scaled and an offset applied so that the depths of the two central features match each other. The depths were chosen as the parameter to be matched as the large field limit is not always clear in the experimental results and the zero field minima has a depth which can be influenced by non-uniformities in the field (section 4.5.2).

In comparing the experimental and theoretical traces, some striking differences are apparent. Firstly, the experimental results have substantially broader central features than the matched theoretical curves. The general shape however, appears to at least qualitatively similar to the theoretical predictions. The large central feature, although broader, appears similar in shape to the calculated one while at higher fields the signal reduces slowly. It is not however, clear in the experiment that the signal reaches a steady high field level as predicted by the theory. Although this disagreement is disconcerting, the widths of these distributions still contain interesting information. Table 4.1 shows the FWHMs of the central valleys of the experimental results in both absolute and normalised units.

These (normalised) FWHMs are equal within the uncertainties of the measurement, so the FWHM goes as $\frac{1}{d}$, as expected given that the Landé factor and atomic velocity distribution remained constant. This linear behaviour in $\frac{1}{d}$ indicates that
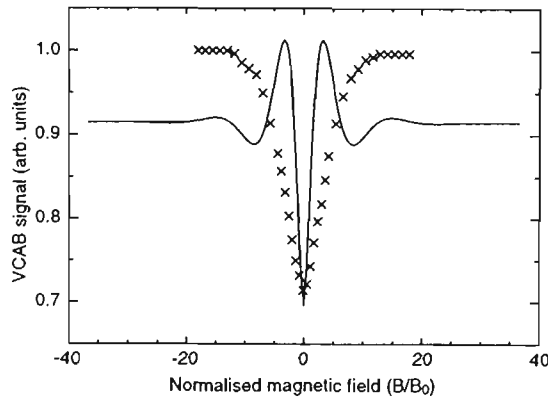
(a) Experimental and theoretical Larmor precession results for 3 mm laser separation
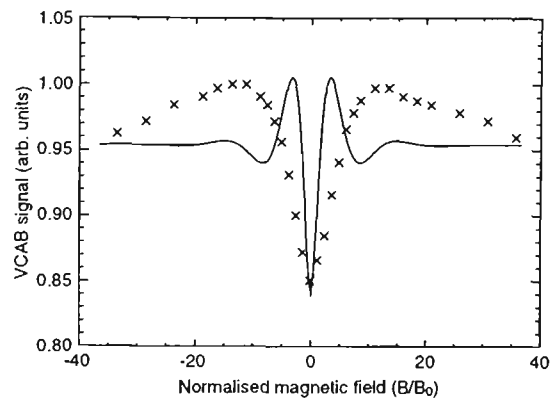
(b) Experimental and theoretical Larmor precession results for 6 mm laser separation
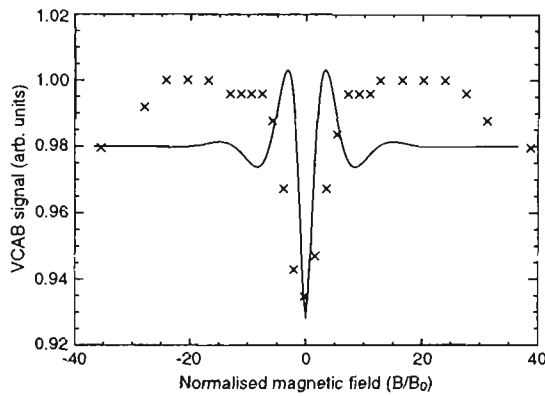
(c) Experimental and theoretical Larmor precession results for 9 mm laser separation
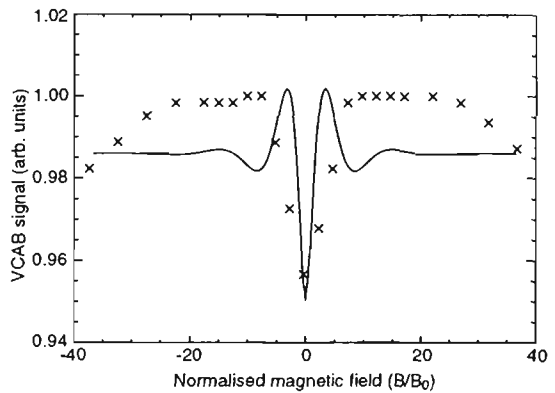
(d) Experimental and theoretical Larmor precession results for 12 mm laser separation

**Figure 4.6**: Plots of the experimental (crosses) and theoretical (solid line) Larmor precession signals for the different laser beam separations. The theoretical curves were fitted to match the size of the experimental central features.

| Beam separation (mm) | Experimental FWHM ($\mu$T) | Experimental FWHM (normalised $B/B_0$) |
|---|---|---|
| 3 | $20 \pm 0.5$ | $7.3 \pm 0.2$ |
| 6 | $10 \pm 0.5$ | $7.3 \pm 0.4$ |
| 9 | $6.6 \pm 0.5$ | $7.2 \pm 0.6$ |
| 12 | $5.1 \pm 0.5$ | $7.4 \pm 0.8$ |

**Table 4.1**: Table of the experimental full widths at half maximum of the central features for the various beam separations used in the Larmor precession experiment.

we are seeing a magnetic field dependent time evolution of the atoms, however, the widths are much larger than the expected value of $2.48 B_0$.

## 4.5 Discussion

Several factors may be responsible for the disagreement between the experimental and theoretical results and these are discussed later (section 4.5.2). The measured signals did however, vary roughly as expected with magnetic field and laser separation. This indicates that the signal arises from polarised atoms, produced by the chopped laser, affecting the absorption of the probe.

Such an arrangement is highly sensitive to small changes in the applied field, and could be used in low field magnetometer applications. Unlike conventional magnetometers, this scheme requires no metallic (ferromagnetic) components near the sensor (vapour cell) which can distort the local magnetic field.

Returning to the discrepancy between the experimental and theoretical results, it is worth looking more closely at the work of other authors and comparing our results to theirs.

## 4.5.1 Comparison with other work

Several authors, [61, 39, 62, 63, 64] have performed experiments which relate closely to ours. It is interesting to study their results, in terms of the normalised magnetic field and compare these to the theory and the present findings.

Schieder and Wälther [61] performed an optical pumping experiment in sodium in which they measured fluorescence from (precessing) polarised atoms in an atomic beam. A magnetic field was applied along the axis of the atomic beam, as was done in the present work, and the fluorescence was seen to vary as a function of the applied field. They observed a strong central valley, similar to those presented in section 4.4, which had a FWHM of $8\,\mu$T. Their pump and probe lasers were separated by $7\,$mm, but they did not provide details of the temperature (or velocity) of the atoms in their beam. We assumed that their sodium oven was at a temperature of 400°C (typical for sodium atomic beams [65]) which gives a most probable velocity of approximately $700\,$m/s. From these values it was possible to calculate $\alpha$ and then $B_0$ for their conditions as follows,

$$\alpha = \frac{g_F \mu_B}{\hbar} = 6.99\,\text{GHz/T} \tag{4.6}$$

where, $g_F = \frac{1}{2}$ for the $F' = 2$ ground state in sodium. This gives,

$$B_0 = \frac{\bar{v}}{\alpha d} = 2.26\,\mu\text{T} \tag{4.7}$$

Thus the normalised FWHM is 3.5 $B_0$, which is approximately half the width of ours, but nearly 1.5 times larger than the theory. Even though the velocity has been approximated, a velocity of $1000\,$m/s would be needed to resolve the discrepancy, ie. a temperature of approximately 1500°C which is well above any reasonable operating temperature of a sodium oven [3].

A similar analysis has been performed for the results of the other authors and the experimentally determined FWHMs are given in table 4.2 below. The uncertainties

in the FWHMs arose from estimating the width of features from their plotted results.

| Author | Year | Element | Normalised FWHM ($B_0$) |
|---|---|---|---|
| Schieder *et al.* | 1974 | sodium | $3.5 \pm 0.4$ |
| Nakayama *et al.* | 1980 | sodium | $2.5 \pm 0.5$ |
| Théobald *et al.* | 1991 | caesium | $1.6 \pm 0.2$ |
| Schuh *et al.* | 1993 | rubidium | $3.2 \pm 0.3$ |
| Zielonkowski *et al.* | 1998 | lithium | $2.6 \pm 0.2$ |

**Table 4.2**: Table of the experimental full width at half maximums of Larmor precession signals obtained by previous authors. FWHMs are given in normalised units.

As can be seen from these values not all authors have found good agreement with the predicted FWHM of $2.48 \, B_0$. They have reported numbers which are substantially closer than our findings, but are still not consistent either with each other or the theory. This suggests that either the theoretical model presented above is not complete and needs to be improved, and/or experimental imperfections (such as extraneous magnetic fields and incomplete optical pumping, especially of atoms deeper in the cell) were not properly accounted for.

## 4.5.2 Possible improvements

There are several ways the model and experiment could be improved to bring the two into better agreement. The theory assumes some simplifying factors which can never be completely realised experimentally. These are, firstly, that atoms which interact with the chopped laser are all completely polarised. In the present experiment, the chopped laser intensity is relatively high (with a saturation parameter, $\frac{I}{I_{sat}}$ of 18, where $I_{sat} = 1.65 \, \text{mW/cm}^2$) so this would be expected to produce a high, but not complete, degree of polarisation in the atoms with which it interacts. Secondly, the model takes no account of the different excitation probabilities from each of the ground state sublevels (except for the $m_F = +3$ level which is assumed to have zero

excitation by the probe laser).

For the theory to take these factors into account, a detailed optical pumping calculation to determine the distribution of atoms in the magnetic sublevels of the $F' = 3$ ground state would be needed. Then, the time evolution of this ensemble could be determined in the presence of a magnetic field and the probe absorption for this evolved distribution calculated.

However, the theory presented here has been used by Nakayama *et al.* [39] and Zielonkowski *et al.* [64] and excellent agreement has been demonstrated. This leads us to believe that it is more likely to be the experimental factors which cause the majority of the experimental/theoretical discrepancy.

Experimentally, the situation could be improved by applying more uniform magnetic fields to the cell. Schieder *et al.* found that their fluorescence spectra were significantly distorted if the earth's magnetic field was not completely cancelled [61]. In the present work, variations in the magnetic field of up to $2\,\mu$T were measured along the length of the cell. Given that the expected width of the central features is not substantially greater than this, it is not surprising that these field variations would lead to broadening and distortion of the results. It would be desirable therefore, to use magnetic shielding to cancel the earth's field and a carefully designed coil arrangement to generate a highly uniform magnetic field in the region of the cell. In the more recent experiments elsewhere [62, 63, 64] coils inside of magnetic shielding have successfully been used to generate uniform magnetic fields with a very low background ($< 50\,$nT [64]).

With large beam separations, the depths of the central valleys was seen to decrease, indicating variations (non-uniformities) in the applied magnetic field. As the laser separation increases, the system becomes more sensitive to small changes in field. Thus only a small amount of distortion on the field can seriously affect the polarisation of the atoms over the longer distances. With a more uniform magnetic field, the central features would be expected to grow in depth and narrow in width, bringing them closer to the theory.

## 4.6  Conclusions

In this chapter, it has been shown that the vapour cell atomic beam can be used to observe the Larmor precession of Rb atoms as they travel between two adjacent laser beams. The dependence of the observed signals on the magnetic field and the distance between the two lasers indicates that we are seeing a true time evolution of the the internal state of the atoms.

The experimental results observed are quite similar to those reported previously [61, 39, 62, 63, 64], however, the widths of the observed central features are significantly broader than both the theoretical prediction and previously reported results. This can be attributed primarily to imperfections in the experimental conditions, in particular, spatial variations in the applied magnetic field. In the next chapter, another useful appication of the VCAB is demonstrated, that is, for the observation of laser cooling.

# Chapter 5

# OBSERVATION OF LASER COOLING USING THE VCAB

The vapour cell atomic beam has now been used to observe the Larmor precession of polarised atoms in a magnetic field and hence may be useful in magnetometer applications. Another widely reported use of conventional atomic beams is in the study of laser cooling, particularly one-dimensional cooling. In this chapter, we show experimentally that the VCAB can be used to observe one-dimensional laser cooling, in an analogous way to cooling in a conventional atomic beam.

There are various ways light can be used to control the motion of atoms. In section 5.1, these are introduced and a review of some of the important developments in laser cooling is provided . Following this, the technique used to observe laser cooling of the vapour cell atomic beam will be explained. A description of the experimental conditions and results is given in sections 5.3 and 5.4 respectively. Finally, the results are discussed and the experiment compared to cooling in a conventional atomic beam.

## 5.1   Background

Techniques for controlling the motion of atoms with laser light have been a popular topic of investigation for a number of years. The 1997 Nobel prize in Physics was awarded jointly to W. D. Phillips, S. Chu and C. Cohen-Tannoudji for their pioneering work in the field of laser cooling.

## 5.1.1 Review of laser cooling

Laser cooling was first suggested in 1975 by Wineland and Dehmelt, who described techniques for cooling ions [66], and by Hänsch and Schawlow, who described possibilities for cooling neutral atoms [67]. The essential idea was to use red detuned (below resonant) laser light to reduce the kinetic energy of the atoms or ions with which it interacts.

Laser cooling of ions was first demonstrated by Wineland *et al.* in 1978 [68], and has since been realised in many species of atoms. The first experiments with neutral atoms involved the slowing of thermal atomic beams. In 1982 Phillips and coworkers slowed a beam of sodium atoms using a laser beam propagating opposite to the direction of the atom beam [69, 70]. These experiments were then further developed and larger numbers of slower atoms were being prepared. In 1985 Ertmer *et al.* reported a scheme they used to slow atoms in a sodium beam [71]. A frequency chirped field from a dye laser, incident upon the sodium beam, was seen to reduce the velocities of the atoms. A cloud of slow atoms with a temperature less than $50\,\mathrm{mK}$ was produced. Around the same time, Prodan *et al.* slowed a sodium atomic beam using a technique known as Zeeman slowing [72]. This scheme involved tuning the atomic resonance frequency with a spatially varying magnetic field along the length of the atomic beam. As atoms travel along the beam, they are slowed and their Doppler and Zeeman shifts change in such a way that they remained resonant with the cooling laser. Therefore, there was no need to chirp the laser frequency, and the atoms were cooled continuously.

Another development in 1985 was the phenomena known as "optical molasses" reported by Chu *et al.* [73]. This name was assigned to three orthogonal pairs of counter-propagating laser beams (standing waves), which could be used to slow atoms in three dimensions. Atoms which enter the molasses are damped (slowed) in the same way as a particle moving in a viscous liquid, hence the name, and a group of cold atoms is produced.

The next notable development in laser cooling techniques came in 1987 with the

demonstration of the magneto-optical trap (MOT) by Raab *et al.* [74]. A quadrupole magnetic field was applied around the region of optical molasses and this introduced a spatially dependent confining potential (provided that the polarisation of the laser fields were appropriately chosen). This scheme allowed a greater number of atoms to be trapped for substantially longer periods. These trapped atoms were confined at the lowest kinetic temperatures ever observed.

It was soon discovered that the temperatures of the cold atom clouds produced in laser cooling experiments were far lower than the expected theoretical limit [75]. This limit, known as the Doppler limit temperature, $T_D$, is given, in the low intensity regime, by $\frac{\hbar\Gamma}{2k_B}$ [54] ($= 144\,\mu$K for the $D_2$ transitions in rubidium). Until then, a relatively simple view of the physical process of laser cooling, based on two-level atoms, had been used. It was only later, in 1989, that a more accurate description of the cooling processes (including the full multilevel atomic structure) revealed there was more than just the spontaneous force acting on the atoms at these low temperatures [76]. These new mechanisms became known as polarisation gradient cooling as they depend upon the spatially varying polarisation of the laser fields.

There have also been several other techniques for cooling atoms, for example the channelling of atoms through the nodes of a standing wave [77], cooling by stimulated emission [78] and cooling by velocity selective coherent population trapping [79]. The latter has yielded atomic samples with extremely low temperatures (in one-dimension) below the one-photon recoil limit. More recently, 3D Raman sideband cooling has been demonstrated and shown to produce clouds of cold atoms with temperatures below 300 nK [80].

Several detailed review articles on laser cooling exist (see for example [81, 82, 83, 75] for a description and review of the main techniques). I shall now focus on cooling experiments more closely related to the present work, namely one-dimensional cooling or collimation of atomic beams.

Atomic beams emerging from an oven can be collimated by apertures, but this greatly reduces the number of atoms in the beam. Laser light can also be used to

collimate atomic beams by cooling the atoms in the beam in one or two dimensions, without reducing the beam flux. Collimated atomic beams are required for a number of applications including collision studies, atom lithography [84] and atom interferometers [85]. Additionally, the study of one-dimensional laser cooling of atomic beams has been a useful way to learn about the physical processes involved in laser cooling. Techniques for the focussing and collimation of atomic beams have been in use for a considerable time now, and the reader is referred to [86, 81] for a review and summary of the main early achievements.

More recently, there have been a number of studies focussed on cooling with high intensity lasers because, for a long time, the theoretical predictions and experimental data have displayed poor agreement. Studies on laser cooling of chromium [87], sodium [88] and rubidium and helium [89] have made considerable progress towards a better understanding of cooling processes at high intensities.

The VCAB cooling technique provides a simple and novel way to study laser cooling. There has also been considerable interest in cooling atoms in a vapour cell [40] however, to date the only successful demonstrations have used a vapour cell which was attached to a pumped vacuum chamber [90].

## 5.1.2  Spontaneous force

Probably the most fundamental way that light can be used to control atomic motion stems from the spontaneous force. This force can be understood by considering a stationary two-level atom interacting with a near resonant laser wave propagating in the $z$-direction. If the frequency of the laser, $\omega_L$, is detuned below the resonance frequency of the stationary atom, $\omega_0$, the atom will absorb very little light. If however, the atom is moving towards the laser with a velocity, $v_z$, where the Doppler shift, $kv_z$ (where $k = \frac{2\pi}{\lambda}$), is such that the atom becomes resonant with the laser, (ie. $\omega_0 = \omega_L - kv_z$), then it will absorb and re-emit photons. Each photon absorbed carries a momentum of $\hbar k$, which is imparted to the atom.

Similarly, when the excited atom spontaneously emits a photon it experiences a

recoil momentum kick in the direction opposite to the emitted photon. The emission of photons is essentially isotropic and so the recoil momentum kicks effectively average to zero. However, the momentum kicks from absorbed photons all contribute in the same direction and do not average to zero. The net result is a change in the atom's momentum in the direction of laser propagation. Once an atom has absorbed and emitted many photons, its velocity, $v_z$, will have changed enough so that it is no longer resonant with the laser. It will then stop absorbing and emitting photons and its z-velocity will stabilise at a new value. In this case, as the atom was initially moving towards the laser, it has been slowed.

Extending these ideas it can be seen that this technique can cool and trap atoms. Consider the case of an atom in a standing-wave laser field (two counter-propagating plane waves) which is once again detuned slightly below the resonance frequency. If the atom is travelling towards one of the laser beams it will be more resonant with that laser than with the one it is travelling away from. Hence, it will absorb more from the laser it is travelling towards, experiencing more force from that laser than the other. Therefore, regardless of the atom's direction of motion, it will always be pushed towards zero velocity (cooled). This is known as Doppler cooling as it is the Doppler shift of the atoms, with respect to the laser beams, that gives rise to the cooling force.

It follows from this that three mutually orthogonal pairs of counter propagating laser beams can cool atoms in three dimensions (optical molasses, as described earlier, 5.1.1). Atoms which enter the three pairs of lasers will be slowed in three dimensions. By applying a quadrupole magnetic field, with a zero at the point of intersection of the three pairs of laser beams, it is possible to create a tightly confining magneto optical trap (MOT). This relies on the Zeeman shift bringing atoms into resonance with the laser beam which pushes them toward the centre of the trap. When in the centre, the field is zero and so the atoms experience no net force. This type of trap is a reliable way of producing a cloud of trapped cold atoms

As a final note, the momentum carried by photons is very small compared to the

momentum of thermal atoms. Thus a large number of photons are required before any significant change to atomic velocities can occur. As a result, usually only very slow atoms which enter a trap can be confined. Atoms with any significant velocity will pass through the trap, experiencing only a small change in their velocity.

### 5.1.2.1  Spontaneous force in the low intensity limit

To better understand the spontaneous force, it is instructive to study the case of an atom in a low intensity laser field. The force experienced by a two level atom in a laser field propagating in the $z$-direction is given by the product of the photon momentum and the average photon scattering rate yielding [81]

$$F_{\text{SP}} = \frac{\hbar k \Gamma}{2} \frac{G}{1 + G + \frac{4(\Delta - k v_z)^2}{\Gamma^2}} \tag{5.1}$$

where $G = \frac{I_L}{I_S}$, $I_L$ is the intensity of the laser, $I_S$ is the saturation intensity, $\Gamma$ is the average photon scattering rate or natural linewidth of the transition, $\Delta = \omega_L - \omega_0$ is the laser detuning from resonance and $v_z$ is the velocity component of the atom in the direction of laser propagation.

In the case of a low intensity standing wave ($I_L < I_S$), the force experienced by the atom is simply the sum of the forces of the two oppositely directed travelling waves. This has been calculated and plotted as a function of atomic velocity (figure 5.1). The detuning of the laser, $\Delta$, is equal to $\frac{\Gamma}{2}$ which is the optimum condition for Doppler cooling, and the saturation parameter, $G$ is 0.5.

This force is essentially linear over the region $-\frac{1}{2} < \frac{kv}{\Gamma} < \frac{1}{2}$ which is approximately the velocity capture range for Doppler cooling. Atoms whose velocities lie within this region experience a friction force and can be slowed to very low kinetic temperatures.

This description applies to the simple case of a two level atom in a low intensity standing wave. For real atoms, with many levels, and at higher laser intensities, the theory becomes far more complicated [76].
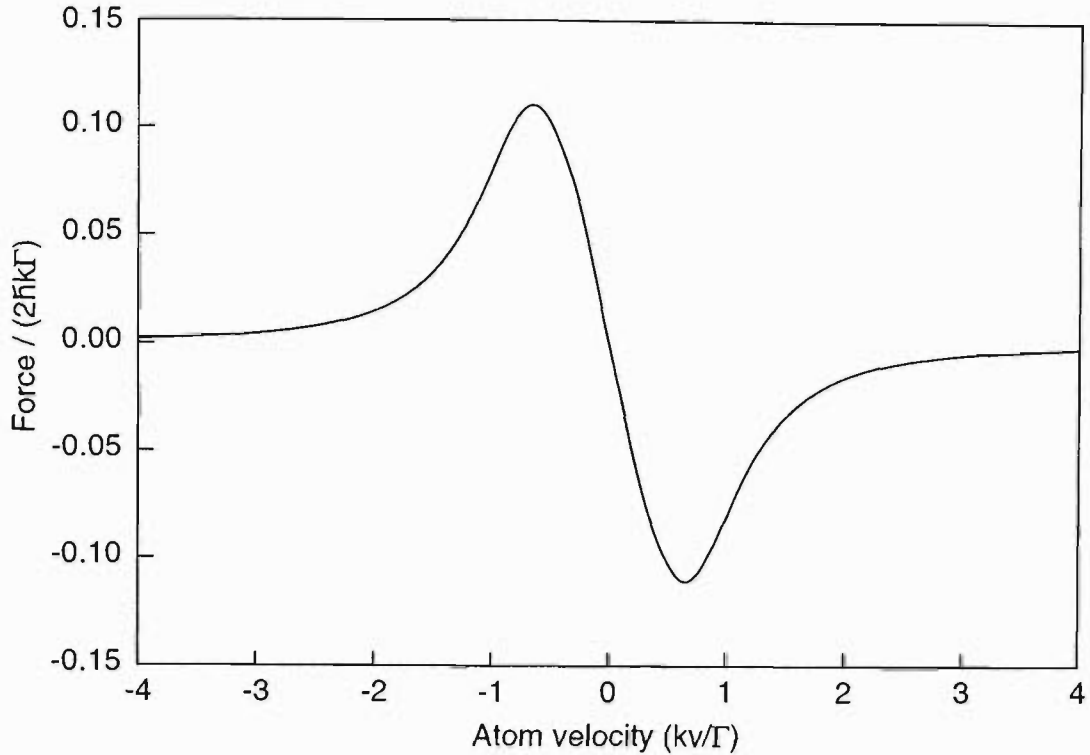
**Figure 5.1**: Spontaneous force on a two-level atom in a low intensity standing wave. This is equal to the sum of two Lorentzians, corresponding to two counter-propagating laser beams described by equation 5.1, where the laser detuning is half the natural linewidth of the transition and $G = 0.5$.

## 5.2  Laser cooling of the VCAB

It has previously been shown (section 3.4) that the transverse velocity distribution of the VCAB can be described by the product of two Lorentzians centred around $v_z = 0$ with a width of approximately $6\,\text{m/s}$. In order to observe laser cooling of the VCAB we devised a scheme which could measure cooling with this limit on the transverse velocity resolution.

One of the primary difficulties in performing cooling experiments in a vapour cell is measuring the velocity distribution of the cooled atoms. Imaging the velocity distribution of a real atomic beam is relatively simple as it only involves taking a spatial fluorescence profile of the atoms once they have travelled some distance from the cooling laser [87]. In the VCAB, however, this type of detection is not suitable for several reasons. Firstly, as the cell is quite small, it is not possible to measure the atoms at a large enough distance from the cooling laser to detect changes in

their spatial distribution. Secondly, as the vapour cell beam consists of a sheet of atoms, rather than a point to point stream, it is not possible to directly correlate the position of atoms with their transverse velocity. Finally, fluorescence arising from the probe laser is due primarily to atoms which are not part of the vapour cell beam. Thus any way of studying the beam characteristics requires the use of the lock-in detection scheme, described in chapter 3. The only direct information which can be obtained about the VCAB is a measurement of the number of atoms in the beam. Therefore, a scheme which allowed us to measure laser cooling, using only this information, was employed.

## 5.2.1 Concept

To understand the principles of the VCAB cooling experiment, it is instructive to consider the arrangement shown in figure 5.2. A third (cooling) laser has been added to the system. This laser propagated parallel to and in the same plane as the chopped and probe lasers. It was retro-reflected upon itself creating a standing wave situated such that atoms, which would normally travel through the chopped and probe lasers, also pass through the cooling laser.

The basic idea was to collimate the atoms before they entered the VCAB. As seen in figure 5.2, atoms travelling near to the direction of the VCAB also intersect the standing wave field of the cooling laser. Once in the standing wave (provided it is tuned below resonance) these atoms may be cooled and they will emerge from the cooling laser with their $z$-velocity components substantially reduced. This means there will be more atoms travelling perpendicular to the laser beams, that is more atoms in the velocity range excited by the chopped laser. This leads to an increase in the number of atoms in the VCAB, which is easily detectable with our scheme as an increase in the signal observed on the lock-in amplifier.

Similarly, if the cooling laser is tuned slightly above resonance (blue detuned), we would expect to observe laser heating of the atoms. Instead of seeing atoms cooled into the detectable velocity region, they would be heated out of it, as the radiation
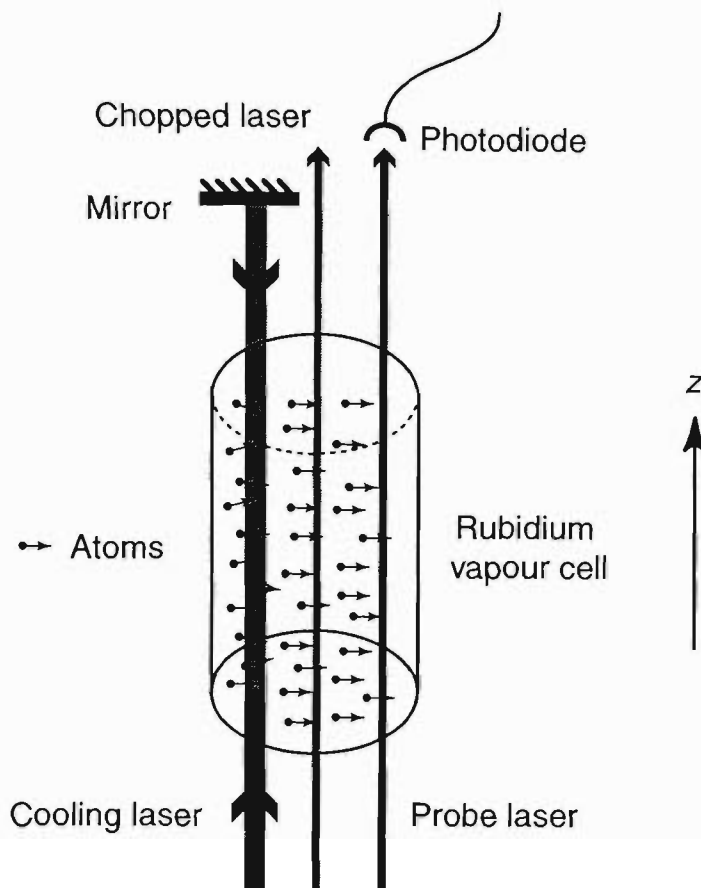
**Figure 5.2**: Principle of the laser cooling measurement. Atoms with a spread of velocities enter the cooling laser. These atoms are then collimated and detected in the VCAB system.

pressure force will be adding to the $z$-velocity component rather than reducing it.

With this setup for the observation of cooling, the cooling laser had to be located before the chopped and probe lasers. If it was located between the chopped and probe lasers, the effect on the velocity distribution of atoms in the beam would be virtually undetectable. Modifying the atoms' velocities after they have been labelled by the chopped laser does not effect the number of atoms in the beam so there is no way of identifying the atoms which have been cooled. With the cooling before the chopped laser, more atoms are placed into the velocity range which the chopped laser excites (ie. more atoms near $v_z = 0$) and this is manifested as an increase in the number of atoms in the atom beam.

## 5.2.2 Cooling in $^{87}$Rb

To realise this scheme in rubidium ($^{87}$Rb) three lasers were required. Figure 5.3 shows a partial energy level diagram of $^{87}$Rb and the transitions excited by each laser. The chopped and probe lasers were locked to the $F' = 2$ to $F = 2$ and $F' = 2$ to $F = 3$ transitions respectively, as in section 3.3. The cooling laser was tuned to the $F' = 2$ to $F = 3$ transition and its frequency was scanned over a small range around resonance, to observe its influence at both red and blue detunings.
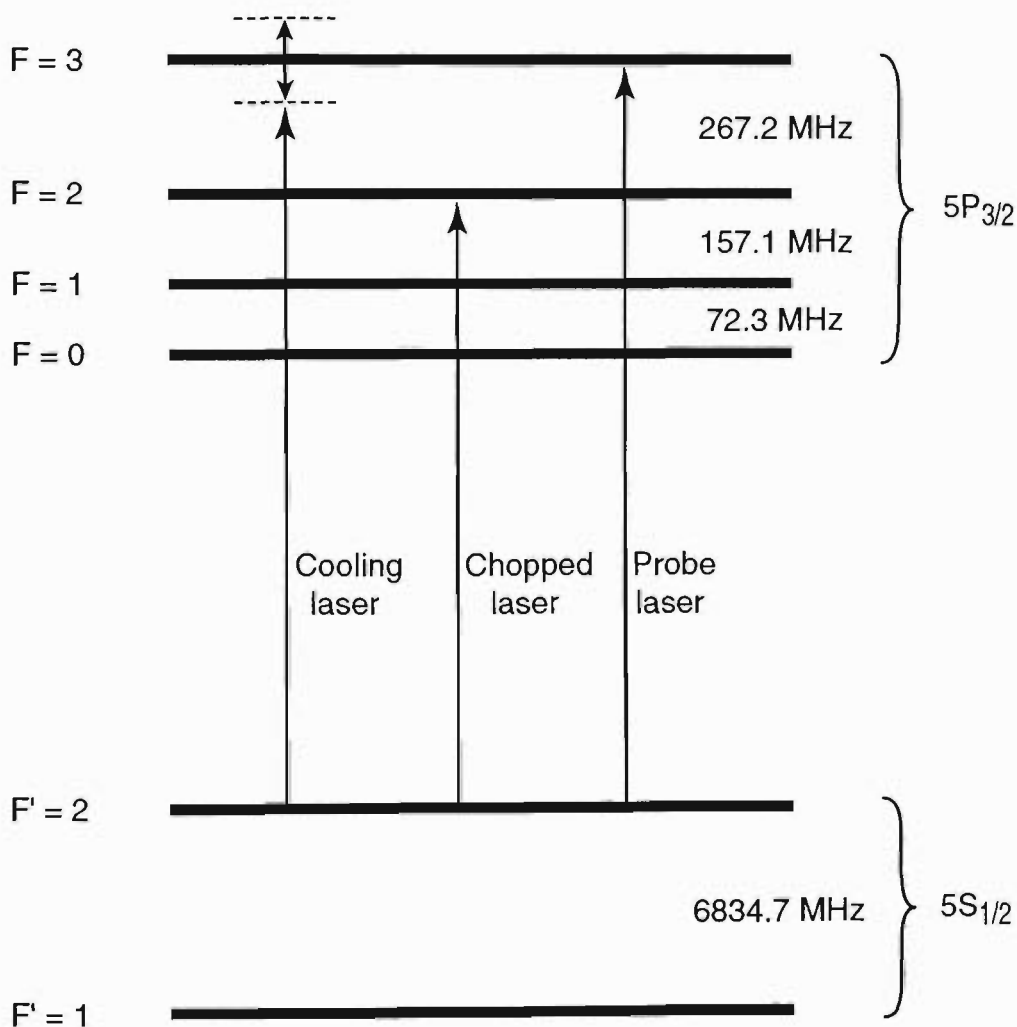


Figure 5.3: Partial energy level diagram of $^{87}$Rb showing the role of the cooling, chopped and probe lasers. The chopped and probe lasers were locked to the $F' = 2$ to $F = 2$ and $F' = 2$ to $F = 3$ transitions respectively. The cooling laser was scanned around the $F' = 2$ to $F = 3$ resonance.

The $F' = 2$ to $F = 3$ transition was the obvious choice for the cooling transition

for two important reasons. Firstly, it is the strongest transition so atoms will be cooled more quickly on this transition than on any others.

Secondly, as will be discussed in section 5.2.4, the cooling laser also introduces some additional optical pumping effects. These can obscure the real cooling effects as the optical pumping alters the observed signals. By cooling on this transition, these optical pumping effects are minimised, yielding the clearest measurement of laser cooling.

## 5.2.3 Cooling in the lin. ⊥ lin. configuration

At this point it is necessary to describe one of the intricacies of the cooling experiment. Unlike the standing wave experiment shown in figure 5.2, the actual cooling experiment included a quarter wave plate between the cell and the retro-reflector, as seen in figure 5.7. This served two purposes. Firstly, it means that, as well as Doppler cooling, polarisation gradient cooling was occurring and secondly, it reduced the amount of optical feedback getting back to the laser diode (without the quarter wave plate, the retro mirror could not be aligned directly on the path of the incoming beam without disturbing the stability of the laser diode).

The fact that we also have polarisation gradient cooling occurring, complicates the analysis of the cooling experiment, but as will be shown, the effects of the polarisation gradient cooling will have a negligible impact on the observed results. In order to see this we first need to understand the cooling process.

The cooling laser consists of two linearly polarised laser beams travelling in the $\pm z$-direction. The polarisation of the incident and return beam are oriented along the $y$ and $x$ axes respectively. The electric field, $\mathbf{E}(z,t)$ for this combination is given by

$$\mathbf{E}(z,t) = \mathbf{E}_x cos(\omega t - kz) + \mathbf{E}_y cos(\omega t + kz) \tag{5.2}$$

where $\mathbf{E}_x$ and $\mathbf{E}_y$ are the electric field vectors of the two polarisations. Assuming that $\mathbf{E}_x$ and $\mathbf{E}_y$ have equal amplitude, we find that at $z=0$, the polarisation of

the standing wave is linear and given by $\mathbf{E}_x + \mathbf{E}_y$ (see figure 5.4). At $z = \frac{\lambda}{8}$ the polarisation is circular, $\sigma^-$. At $z = \frac{\lambda}{4}$ the polarisation is linear and rotated by 90°, given by $\mathbf{E}_x - \mathbf{E}_y$. At $z = \frac{3\lambda}{8}$ the polarisation is oppositely handed circular or $\sigma^+$. The polarisation returns to linear at $z = \frac{\lambda}{2}$ and continues to follow this pattern along the $z$-axis (figure 5.4) repeating with a spatial period of $\frac{\lambda}{2}$.
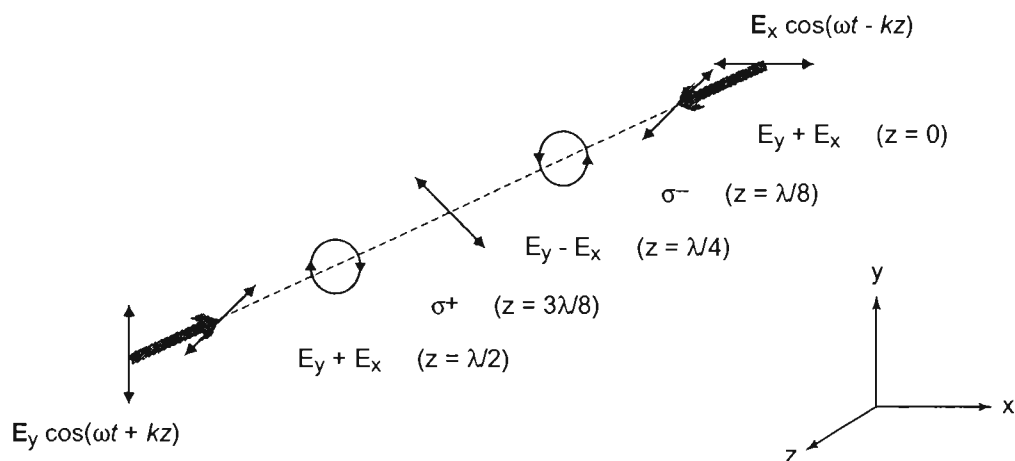


**Figure 5.4:** Plot showing the direction of polarisation of light for two counter-propagating beams in the lin ⊥ lin configuration. The polarisation directions are labelled at various positions along the $z$-axis (positions labelled in brackets). The polarisation varies from linear along $\mathbf{E}_y + \mathbf{E}_x$, to circular $\sigma^-$, to linear along $\mathbf{E}_y - \mathbf{E}_x$, to circular $\sigma^+$ and back to linear along $\mathbf{E}_y + \mathbf{E}_x$ over a distance of $\frac{\lambda}{2}$.

Polarisation gradient cooling requires that the ground and excited states contain more than one sublevel and that the transition probabilities between different combinations of levels are different. In the lin. ⊥ lin. configuration the cooling mechanism can be understood by considering an atomic transition between ground state with angular momentum $J = \frac{1}{2}$ and an excited state with $J = \frac{3}{2}$ .

Figure 5.5) shows the energy level diagram for a $J = \frac{1}{2}$ to $J = \frac{3}{2}$ transition along with the Clebsch-Gordan coefficients for each of the possible transitions. The Clebsch-Gordan coefficients provide a measure of the strength of the coupling of an atomic transition to the light field [54].

Polarisation gradient cooling relies on optical pumping and the different light
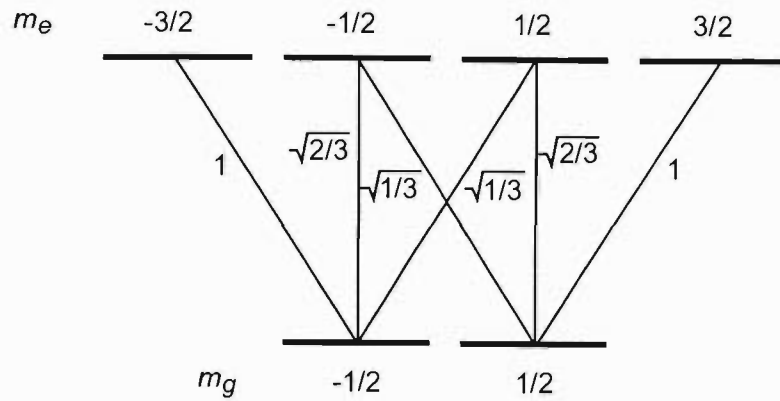
**Figure 5.5**: Energy level diagram for a $J = \frac{1}{2}$ to $J = \frac{3}{2}$ transition. The Clebsch-Gordan coefficients for transitions between the Zeeman sublevels of the ground $(m_g)$ and excited states $(m_e)$ are also given.

shifts (also known as the ac-Stark shift) for transitions between the different sublevels [91]. The light shift, $\Delta U$, is the change in the energy of a sublevel in the presence of an optical field which couples it to a transition [54]. In the low intensity limit, it is given by equation 5.3 [92]

$$\Delta U = \frac{2\hbar \Delta G C_{ge}^2}{4(\Delta/\Gamma)^2 + 1} \tag{5.3}$$

where $\hbar$ is Planck's constant on $2\pi$, $\Delta$ is the laser detuning from resonance, $G$ is the laser intensity relative to the saturation intensity, $C_{ge}$ is the Clebsch-Gordan coefficient for the transition which couples the atom to the light field and $\Gamma$ is the natural linewidth of the transition. As can be seen from equation 5.3 the light shift is proportional to the square of the Clebsch-Gordan coefficient for that transition and its sign is determined by the sign of the laser detuning.

Consider an atom in a region of $\sigma^+$ polarisation in a red detuned light field. Optical pumping will preferentially pump the atom into the $m_g = +\frac{1}{2}$ state which, according to 5.3, has the largest negative light shift (as the $\sigma^+$ light couples it to the $m_e = +\frac{3}{2}$ excited state). If the atom moves away from the centre of the $\sigma^+$ region, the polarisation becomes slightly elliptical and the $m_g = +\frac{1}{2}$ state becomes less strongly coupled to the light field so its light shift becomes less negative. The atom is then climbing up a potential hill and in doing so giving up some of its kinetic energy.

Once the atom has travelled a distance of $\frac{\lambda}{4}$, it will be in a $\sigma^-$ polarisation region. It will then be preferentially pumped into the $m_g = -\frac{1}{2}$ ground state which now has the largest negative light shift as it is coupled to the $m_e = -\frac{3}{2}$.

This process is shown schematically in figure 5.6 As the atom climbs out of one polarisation region it gives up some of its kinetic energy. After a distance of $\frac{\lambda}{4}$, the polarisation has inverted and the light shift is most negative for the other state. The probability for optical pumping into the other state is highest and in getting to this state, the atom spontaneously emits a photon which brings it to its lowest energy state. The motion of an atom between two potential minima therefore reduces the atoms kinetic energy by an amount equal to the light shift.
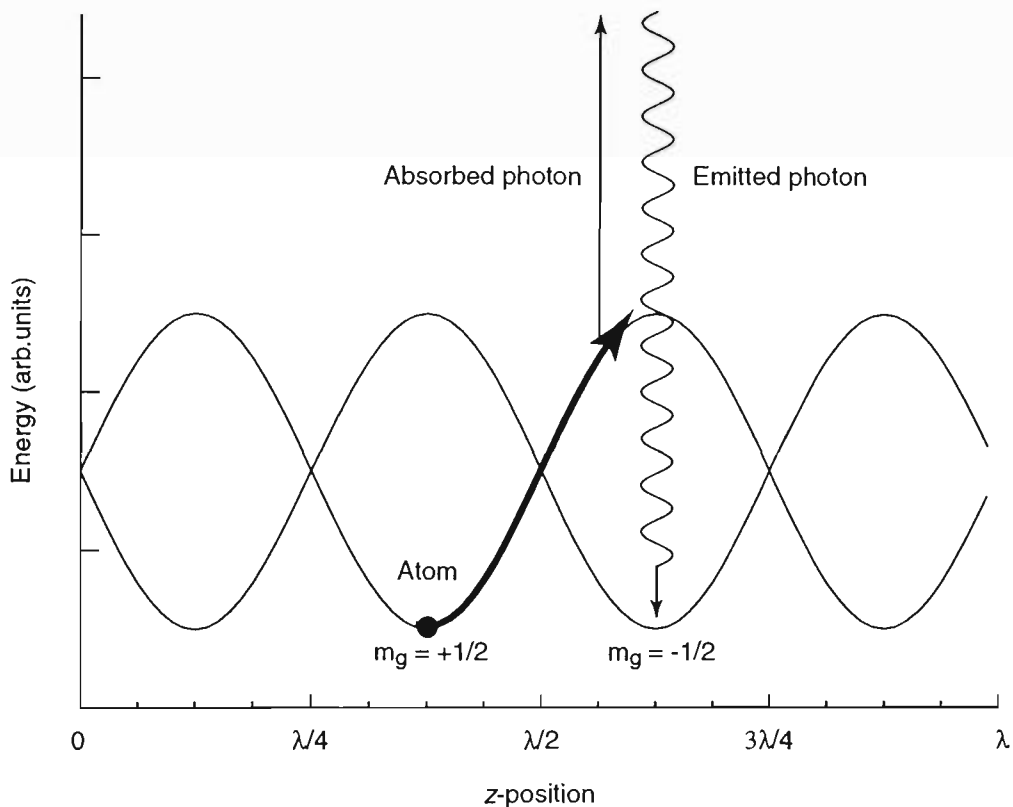


**Figure 5.6**: Lightshift of a J $= \frac{1}{2}$ ground state in a lin $\perp$ lin light field. An atom gets optically pumped into the level with the largest negative lightshift which depends on the polarisation of the light in that region. As it moves, it climbs up a potential hill where it gets pumped into the other ground state which now has the largest negative lightshift. During the optical pumping, the absorbed photon has less energy than the spontaneously emitted photon, so the atom loses some of its kinetic energy in this process.

This type of cooling is known as Sisyphus cooling after the Greek myth in which Sisyphus was condemned to repeatedly roll a boulder up a hill. Sisyphus cooling is most effective on atoms with a velocity less than a characteristic velocity, $v_c$, corresponding to a travelling a distance of $\frac{\lambda}{8}$ in an optical pumping time $\tau_p$ [91]. If they are moving too slowly, then they will not have reached the top of the potential hill before they are pumped. If they are moving too quickly, then they will pass over the top of the hills before they are pumped, making the cooling process inefficient.

In the low intensity limit, one can estimate the characteristic velocity for a $J = \frac{1}{2}$ to $J = \frac{3}{2}$ transition using the following expression [91]

$$kv_c = \frac{1}{2\tau_p} = \frac{\Gamma}{9}\frac{G}{4\left(\dfrac{\Delta}{\Gamma}\right)^2 + 1} \tag{5.4}$$

For an intensity of $G = 1$, and a detuning of $\Delta = -\Gamma$, $v_c = \frac{1}{45}\frac{\Gamma}{k}$. However, equation 5.4 does not apply to either the transition studied here ($F = 2$ to $F = 3$), nor does it describe the intensity range used here.

To accurately determine the range of velocities of atoms, a full quantum mechanical calculation would need be performed however, this is quite difficult and requires a great deal of computing power [89]. An alternative approach is to use a semi-classical approach which requires solving the Fokker-Planck equation. This has been done by Williams *et al.* and their results show that Sisyphus cooling is only important for those atoms with velocities less than $\approx 0.2\frac{\Gamma}{k}$ even at intensities of $G = 50$ [89]. For experiments described later in this chapter, this means that only atoms with velocities less than 1 m/s will be greatly influenced by Sisyphus cooling. As will be discussed later, because of the limited resolution of our VCAB system, we do not expect to resolve the effects of polarisation gradient cooling.

## 5.2.4 Optical pumping considerations

Ideally, the only effect that the cooling laser would have on the vapour cell atomic beam would be to deflect (cool or heat) the atoms. Unfortunately, this is never going to be the case. After excitation by the cooling laser, atoms will not necessarily relax back to the state which they initially occupied. This results in some additional optical pumping to atoms in the system and the measured signals are complicated by this effect. There are however, some simple considerations which enable the optical pumping and cooling effects to be separated as discussed below.

Essentially, there are two important types of optical pumping, these are leakage out of the system to the lower hyperfine ground state, and, redistribution of atoms among the different magnetic sublevels of the upper ($F' = 2$) hyperfine ground state.

Leakage out of the system refers to atoms which are lost to the $F' = 1$ ground state. That is, some of the atoms excited by the cooling laser will relax to the $F' = 1$ ground state, which is not accessed by the chopped laser. Atoms in this state can no longer be part of the vapour cell atomic beam. This has the effect of reducing the number of atoms in the beam, leading to a reduction in measured signals.

The number of atoms lost via this mechanism is expected to be quite small as the cooling laser is tuned to excite atoms to the $F = 3$ excited state. From this state, atoms will all relax only to the $F' = 2$ ground state as relaxation to the $F = 1$ state involves a transition for which $\Delta F = 2$, which is non-allowed for a dipole transition. However, the intensity of the cooling laser is sufficiently high to excite a small fraction of atoms to the $F = 2$ state due to the substantial power broadening. Once in the $F = 2$ state, they may relax to the $F' = 1$ ground state, in which case they are lost from the system.

One can estimate the effects of optical pumping via this route using equation 3.3 where the detuning, $\omega_L - \omega_0$ is $2\pi \times (267 \pm 20)$ MHz. The $\pm 20$ refers to the variation in optical pumping as the laser frequency is scanned. The excitation predicted to the $F = 2$ excited state for detunings at the highest intensities are approximately 0.006 and 0.004 for the lowest and highest cooling laser detunings respectively. As

expected, this leakage will be most significant when the cooling laser is detuned to the red side of resonance because the laser frequency is closer to the $F' = 2$ to $F = 2$ transition.

Thus we would expect any loss of atoms, arising from this optical pumping mechanism, to reduce the signal more for red detunings than for blue although this effect will be small as shown be the expected fraction of atoms excited to the $F = 2$ state. Fortunately then, the signature of this optical pumping mechanism has the opposite detuning dependence to that of laser cooling so we can use this to establish whether the optical pumping or laser cooling effects have the strongest effect on the measured signals.

Atoms which do stay in the system after cooling, will experience a second type of optical pumping, that being a redistribution among the $(2F + 1)$ magnetic substates of the $F' = 2$ ground state. This mechanism can also effect the size of the measured signals as transitions from different magnetic sublevels have different transition probabilities. The absorption of the chopped laser will depend upon the distribution of atoms among the various substates and this will directly impact on the number of atoms labelled.

This optical pumping mechanism depends strongly on the polarisation of the cooling laser. In our experiments, the cooling laser standing wave was in the lin $\perp$ lin polarisation configuration described in the previous section.

It has been shown [93] that the coldest atoms produced in Sisyphus cooling become trapped in potential wells which occur in the $\sigma^+$ and $\sigma^-$ regions of the field. These wells are very small in spatial extent, $\frac{1}{8}$ of the optical wavelength, and atoms occupy and even smaller region $(\frac{\lambda}{15})$ [93]. This means they will finish in the extreme sublevels, $m_f = \pm 2$ levels of the ground state which have the largest negative lightshifts.

However, for atoms to be trapped in these small wells in our cooling laser, the-het must be cooled to a transverse velocity, $|v_z|$, below 1 cm/s [93]. Because the chopped and probe lasers detect a much larger transverse velocity spread than this

($|v_z| \leq 3\,\text{m/s}$) the majority of atoms we detect will have enough transverse veloc-ity to travel across many regions of different polarisation without being confined. Therefore, whilst some of the atoms may be confined, the great majority of atoms we detect will emerge with an essentially random distribution of magnetic sublevel populations.

When the cooling laser is blue detuned, the situation is further simplified. The transverse ($z$) velocity component of the atoms is increased so that they will travel across even more polarisation regions of the cooling laser standing wave. Once again this should lead to an essentially random distribution of magnetic sublevel populations for emergent atoms.

The chopped laser is polarised in the $y$-direction and so it will excite atoms on transitions for which $\Delta m = 0$, where the quantisation axis is defined by the direction of polarisation. Transitions out of the different magnetic sublevels have different transition probabilities so that the amount of labelling applied is dependent upon the magnetic substate the atoms occupy. However, as the population distribution will be essentially random for all cooling laser detunings, we expect this optical pumping mechanism to have no noticeable effect on the signals we measure.

Thus, whilst there will always be two types of optical pumping present in our experiments, they should not prevent us from observing the signature of laser cooling. The first type of pumping (loss to the other ground state) will be weak as the cooling laser is detuned a long way from the $F' = 2$ to $F = 2$ transition and the excitation probability is very low. Additionally, the detuning dependence of this pumping mechanism has the opposite slope to the expected cooling features so we can identify whether we are measuring cooling or optical pumping. The second type of optical pumping will only be important to a very small fraction of the atoms we measure and hence we would not expect this to cause any detectable changes to the signals we measure.

## 5.3   Experimental conditions

Apart from the addition of a cooling laser, the experimental arrangement used for laser cooling was essentially the same as has been described previously (chapter 3). A schematic of the experimental arrangement is given in figure 5.7.
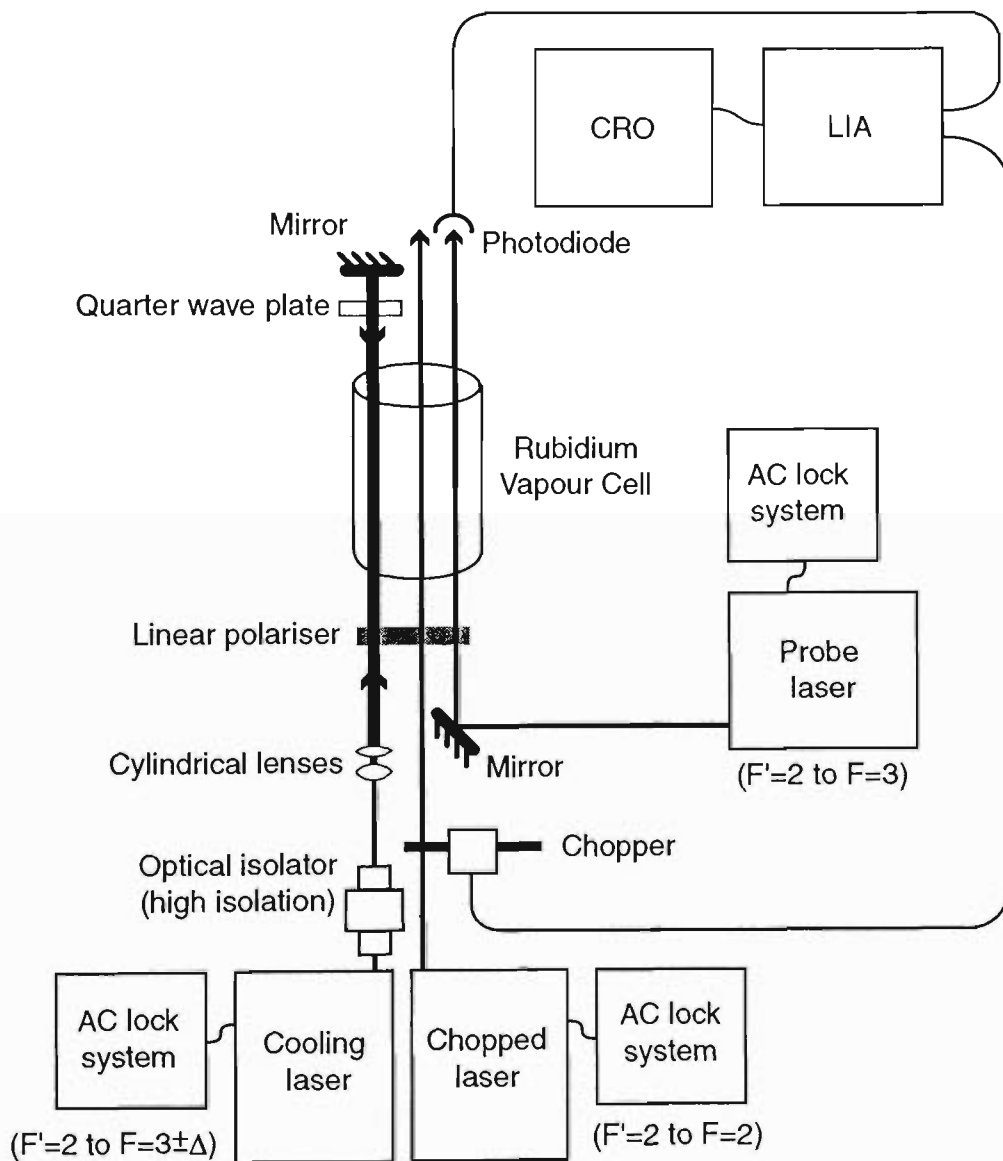


**Figure 5.7**: Experimental arrangement used to observe laser cooling of the VCAB.

The chopped and probe lasers were tuned to the $F' = 2$ to $F = 2$, and, $F' = 2$ to $F = 3$, $D_2$ transitions in $^{87}$Rb respectively. The cooling laser was tuned to the $F' = 2$ to $F = 3$ transition. All lasers were locked using the AC locking technique described
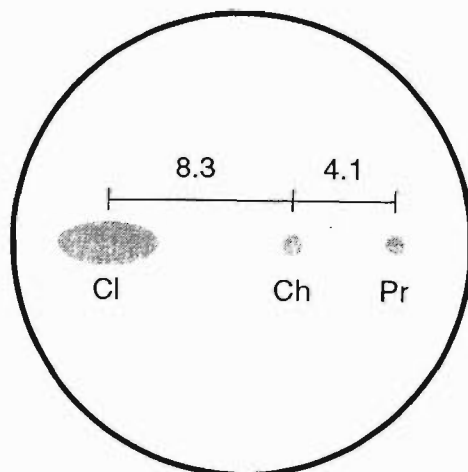
**Figure 5.8**: End view of the vapour cell showing the positions of the three lasers. Pr refers to the probe laser spot, Ch the chopped and Cl the cooling laser. Distances given are in mm.

in section 2.5.2. The lock point of the cooling laser was scanned around resonance by applying a variable DC magnetic field to the reference cell in the locking setup. The cooling laser detuning was measured by beating it with another locked laser of known frequency and measuring the beat note on an RF spectrum analyser. The uncertainty in the measured detuning was $\pm 0.5$MHz.

Three pairs of orthogonal Helmholtz coils (not shown in the figure) were used to cancel the earths magnetic field to less than $2\,\mu$T.

The chopped and probe beams were separated by $4.1 \pm 0.1$ mm. The distance from the chopped laser to the centre of the cooling laser was $8.3 \pm 0.3$ mm. Figure 5.8 shows a scaled cross-sectional drawing of the beams entering the cell, showing the relative positions of the laser beams. The cooling laser was quite a distance away from the other two lasers. This was done to minimise stray light from the laser reaching the photodiode and influencing the measurements. However, as is discussed later, it would have been preferable to have the cooling laser closer to the chopped laser to maximise the number of highly cooled atoms measured.

The cooling laser spot was expanded in one dimension using a pair of cylindrical lenses. This ensured that atoms travelling through the VCAB system would spend a long time in the field and hence experience greater deflection. A spatial intensity

profile of the cooling laser, measured with a Melles Griot Super BeamAlyser 13 SKP 003, is given in figure 5.9. The $\frac{1}{e^2}$ radii of the cooling beam at the vapour cell were $2.60 \pm 0.08$ mm and $1.20 \pm 0.03$ mm in the long and short axes respectively. These values are used later in the theoretical model of the cooling experiment (chapter 6). Here, we use these values to provide an estimate of the laser intensity in the cell.
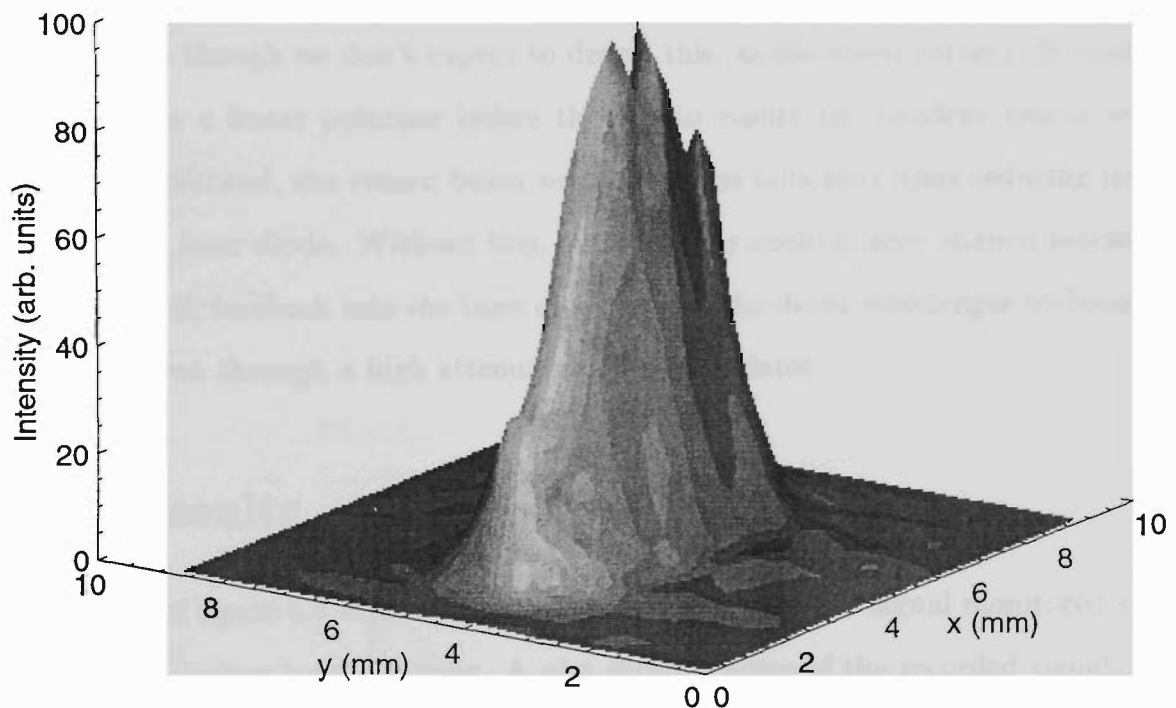


**Figure 5.9**: Spatial intensity profile of the cooling laser. The beam was expanded in the $x$-plane to increase the amount of time atoms spent in the laser field.

The probe and chopped laser intensities were $4.5 \pm 0.3$ mW/cm$^2$ and $5.0 \pm 0.3$ mW/cm$^2$ respectively, as in section 3.4. The cooling laser power, measured prior to entering the cell, was varied over the range 1 mW to 12 mW yielding a range of intensities of $8.5 \pm 0.6$,mW/cm$^2$ to $100 \pm 6$ mW/cm$^2$.

Light entering the cell from all three lasers was linearly polarised along the $y$-axis. On the other side of the cell the cooling laser passed through a quarter wave plate, with its optic axis oriented at 45° to the $y$-axis. This converted the linear

polarisation into circular polarisation. The laser then reflected off the mirror which changed the handedness of the circular polarisation. It passed through the quarter wave plate once more before reentering the cell, converting the light back to linear polarisation. However, this returning linear polarisation was rotated by 90° to the incident beam, creating the lin ⊥ lin polarisation configuration required for Sisyphus cooling.

As mentioned earlier, the motivation for using the lin ⊥ lin scheme was two-fold. Firstly, the cooling efficiency may be slightly increased due to the polarisation gradients (even though we don't expect to detect this, as discussed earlier). Secondly, as there was a linear polariser before the cell to ensure the incident beams were vertically polarised, the return beam would be cross polarised, thus reducing feedback to the laser diode. Without this, and with the cooling laser aligned precisely back on itself, feedback into the laser diode caused the diode wavelength to become unstable, even through a high attenuation optical isolator.

## 5.4 Results

The setup of figure 5.7 was realised and the lock-in amplifier signal monitored as a function of cooling laser detuning. A plot showing some of the recorded signals, as a function of cooling laser detuning and intensity, is given in figure 5.10. A good deal of averaging was used on all of the data presented here to reduce noise. Not all of the scans obtained are shown on this graph, for the purpose of clarity. Scans obtained for all of the laser intensities are studied in more detail in the following chapter when compared with the theoretical predictions.

In the absence of any cooling, these traces would be flat however, strong dispersion shaped signatures are evident for all of the laser intensities. The size of these features increases nonlinearly with laser power. The signals generally peak at detunings of around −5 to −7 MHz. Similarly, the signals are lowest at detunings between +5 and +7 MHz, indicating the detunings for the maximum and minimum number
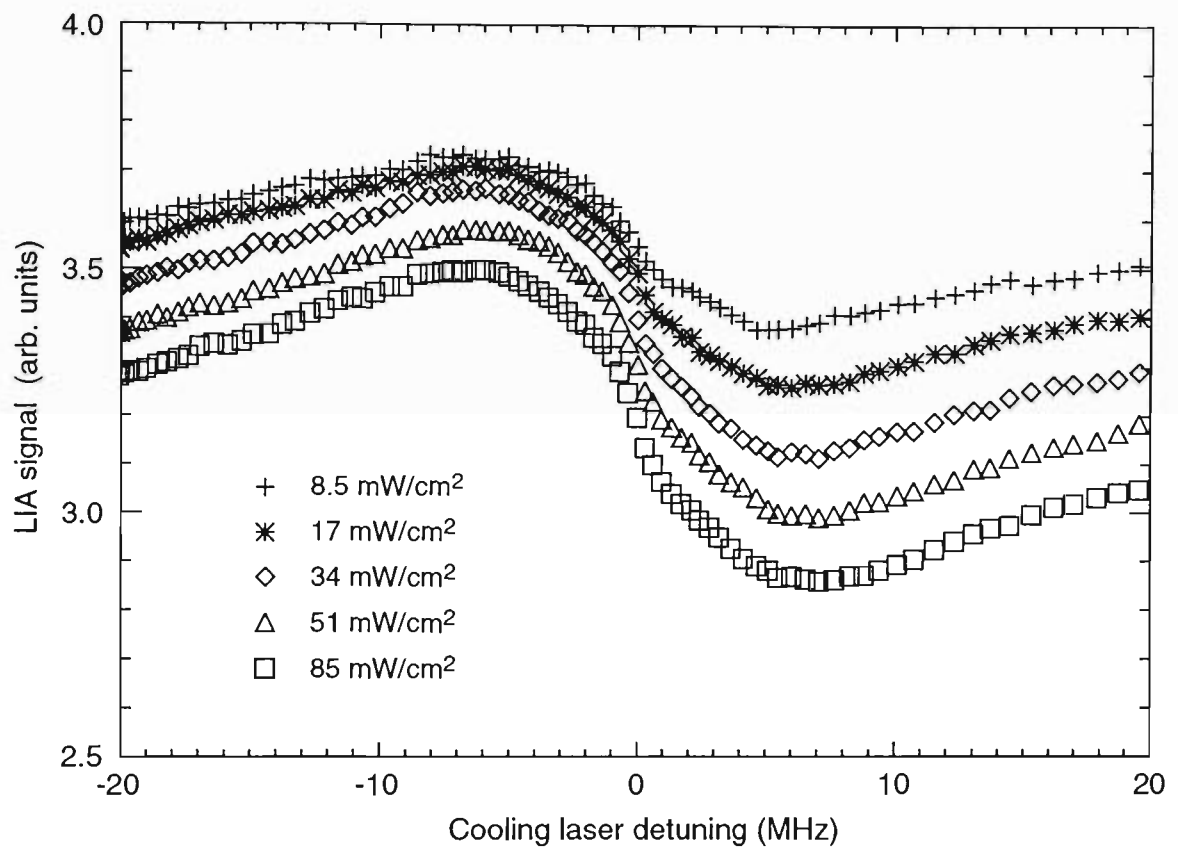
**Figure 5.10**: Measured lock-in amplifier signal as a function of cooling laser detuning for a range of cooling laser intensities (given on the plot). The uncertainty in the detuning was $\pm 0.5$ MHz.

of atoms in the vapour cell atomic beam. As would be expected, the strongest cooling (heating) effects occur when the laser is tuned, $\approx \Gamma$, one natural linewidth, below (above) resonance.

A notable feature of these signals is the gradually decreasing vertical offset. As the laser power was increased, the reference level (or DC offset) steadily decreases. We can define the reference level as the value of the lock-in signal when the cooling laser is precisely resonant with the atoms (ie. detuning = zero). At zero detuning, the cooling force is also zero, as the counter propagating laser beams apply equal and opposite amounts of force to the atoms regardless of their velocity. At this point changes in the signal level for different intensities must arise from effects other than cooling. This is evidence of optical pumping, removing atoms from the system and lowering the size of the measured signals. As would be expected, the number of atoms removed from the system increases with laser intensity. This reference level then provides information about the magnitude of the optical pumping effects (chapter 6).

Looking now at the deviations of the signals from the reference level, it is clear that the cooling becomes more significant with increased laser intensity. To obtain a better indication of the amount of cooling, we calculate a normalised measure of the peak to peak laser cooling effect; given by the signal maximum minus the signal minimum, divided by the reference level. Table 5.1 below shows these values, along with the zero detuning reference levels for the various laser intensities. The peak to peak deviations have also been plotted in figure 5.11. This graph shows the nonlinear increase in the cooling effects as a function of cooling laser intensity. At an intensity of $100 \, \text{mW/cm}^2$, the size of the signal (number of atoms in the beam) varies by over 20%.
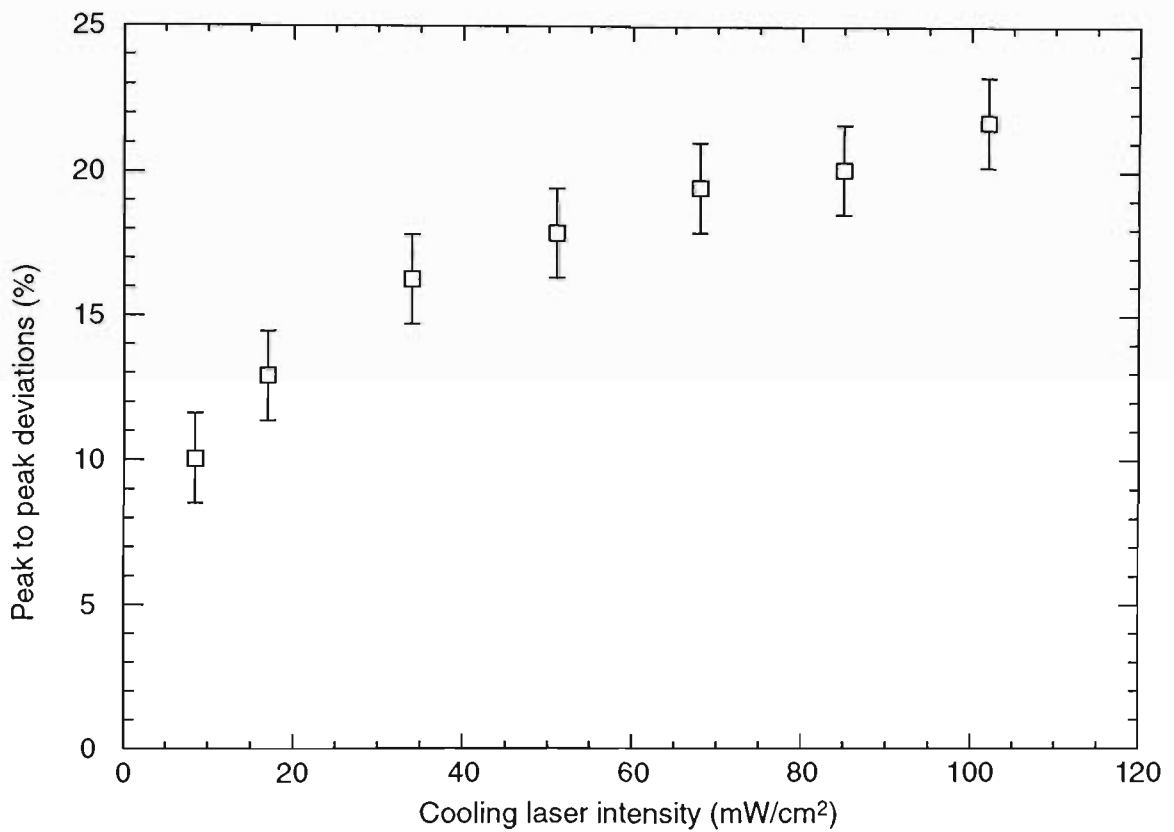
**Figure 5.11**: Normalised peak to peak deviations of the cooled signal relative to the reference level as a function of cooling laser intensity.

| Laser Intensity ±10% (mW/cm$^2$) | Reference level ± 0.04 | Peak to Peak deviation ± 1.6 (%) |
|---|---|---|
| 8.5 | 3.55 | 10.0 |
| 17 | 3.49 | 12.9 |
| 34 | 3.40 | 16.3 |
| 51 | 3.31 | 17.9 |
| 68 | 3.27 | 19.5 |
| 85 | 3.20 | 20.1 |
| 100 | 3.18 | 21.7 |

**Table 5.1**: Table of the reference levels and peak to peak deviations from the reference levels for the various cooling laser intensities.

## 5.5 Discussion

The results shown above demonstrate the expected behaviour of laser cooling. However, the vapour cell atomic beam is not able to completely replicate conventional atomic beams for the study of one-dimensional laser cooling. There are several limitations associated with this technique and these are discussed in the following sections. Also provided are some suggested changes to the experiment which would improve some aspects of the measurement.

### 5.5.1 Comparison with conventional atomic beams

One of the main limiting factors to the usefulness of the VCAB for the study of laser cooling is the transverse velocity resolution. As has already been pointed out, the resolution of the present scheme is limited by the natural linewidth of the the chopped laser transition. In experiments with conventional atomic beams, the transverse velocity resolution of the detection system can be as low as the one-photon recoil velocity, $v_r = 6\,\text{mm/s}$ in Rb [89].

At this stage, all that can be said about the vapour cell cooling experiment is that atoms have been cooled into a velocity range below $|v_z| = 3\,\text{m/s}$. This velocity

resolution is approximately one thousand times worse than in a conventional atomic beam. Measuring cooling with the VCAB then provides no obvious way to determine the temperatures of the coldest atoms in the beam. We would expect these atoms to have transverse velocities of several cm/s, which lies well below our resolution limit.

Even so, we can convert this velocity resolution into a one-dimensional temperature using,

$$\frac{1}{2} m v_{\text{rms}}^2 = \frac{1}{2} k_{\text{B}} T \tag{5.5}$$

where, $m$ is the mass of a rubidium atom, $k_{\text{B}}$ is Boltzmann's constant and $T$ is the temperature of the atoms in Kelvin. This yields a kinetic temperature resolution of $0.09\,\text{K}$ in one dimension, which is good with respect to room temperature, but nothing like that achievable in a conventional atomic beam ($0.4\,\mu\text{K}$ [89]) and is also far above the Doppler limit, $T_{\text{D}} = 144\,\mu\text{K}$.

## 5.5.2    Possible improvements to the experimental technique

There are several ways that the experimental conditions could be improved to give a better measure laser cooling.

One of the obvious ways to improve the amount of laser cooling and reduce the effects of optical pumping would be to use a repumping laser [94]. The repumping laser should be of low intensity ($I < I_{\text{S}}$) propagating coaxially with the cooling laser. The repumping laser would pump atoms out of the $F' = 1$ ground state to the $F' = 2$ ground state. It should be tuned from the $F' = 1$ to the $F = 2$ transition so that atoms would have the greatest chance of finishing in the $F' = 2$ state.

The benefits of introducing a repumping laser are twofold. Firstly, atoms which have been lost to the $F' = 1$ ground state do not experience any further cooling. The repumping laser would take these atoms out of the $F' = 1$ state and return them to the system where they can be further cooled. Secondly, the repumping laser would also take atoms which are initially in the $F' = 1$ ground state (ie. atoms which would normally not interact with either the cooling or chopped lasers) and place them in

the $F' = 2$ state from which they are accessible to both the cooling and chopped lasers. It is clear then, that such a laser would be useful even in the absence of a cooling laser, as it would increase the atom flux of the VCAB by placing more atoms in the ground state which is accessed by the chopped laser. The benefit of this is an increase in the signal to noise ratio.

The main drawback of using a repumping laser is the requirement for a fourth laser. However, in laser cooling experiments with conventional atomic beams, and even three-dimensional atom traps, a repumping laser is generally used as a standard part of the experimental apparatus [93, 26, 88].

There is also a geometrical consideration which can be used to increase the efficiency of the cooling. Essentially, we want all atoms which are excited by the chopped laser and detected by the probe to have interacted with a high intensity region of the cooling laser. Our current setup was not optimised to satisfy this requirement. A simple fix for this problem would be to reduce the diameter of the chopped laser and/or move it closer to the cooling laser beam. Then, only atoms which pass through the centre of the cooling laser and are highly cooled would be labelled by the chopped laser and contribute to the VCAB.

## 5.6 Conclusions

In this chapter it has been shown that the VCAB can be used to study laser cooling. A scheme was developed which allowed cooling effects to be measured with a velocity resolution limited by the interaction of the chopped and probe lasers with the atoms. Experimental verification of this cooling technique has been provided. These studies could be further developed, as mentioned in section 5.5, by modifying the experimental conditions. In order to further verify and analyse the usefulness of this cooling scheme, a theoretical model of the experiment was also developed and this is described in the following chapter.

# Chapter 6

# MODEL OF THE LASER COOLING EXPERIMENT

In the previous chapter, an experimental study of laser cooling using the VCAB was presented. In order to verify and further understand these results, a theoretical model of the laser cooling experiment was developed.

Firstly, an outline of the calculations is given, followed by a description of the modelled situation. The model allows us to predict how the cooling laser alters the velocity of atoms with which it interacts and how this affects the measured signals. Comparisons between the theoretical and experimental results are discussed along with some limitations of the model.

## 6.1   Introduction

Introducing a cooling laser to the vapour cell considerably alters the velocity distribution of the atoms in the cell so that the atoms are no longer selected from a simple Maxwellian distribution. This model was designed to predict the effect of the cooling laser on the number of atoms in the velocity range important to the VCAB and thus the measured signals.

In simple terms, an ensemble of atoms with a range of trajectories and velocities given by the Maxwellian distribution pass through the cooling laser. As they traverse this laser, their $z$-velocity component is altered and they emerge with a new (cooled) $z$-velocity distribution. The chopped and probe lasers then select atoms from this new distribution and those which lie within their absorption profiles form the vapour

cell atomic beam.

As discussed in section 5.2.3 the experiment performed here used lasers in the lin $\perp$ lin polarisation configuration. This means that, as well as Doppler cooling, Sisyphus cooling will also be active [91]. It has already been shown in section 5.2.3 that the atoms which are cooled be Sisyphus cooling already lie well within the velocity range of the VCAB so further cooling of these atoms makes only a small difference to the measured signals. This is illustrated by noting that atoms with $|v_z| \leq 1\,\text{m/s}$ will have at least a 94% of being detected with the VCAB (assuming they have suitable $x$ and $y$ trajectories to intersect the lasers). Thus cooling these atoms further could at most improve there detectability by 6%. Atoms which are cooled from well outside the velocity range of the VCAB (say $|v_z| \approx 10\,\text{m/s}$) can have there detection probability increased from less than 10% to above 90% if they are cooled to $\approx 1\,\text{m/s}$. We expect that the main contribution to changes in the signal we measure to be the result of these hotter atoms being Doppler cooled into the velocity range we measure rather than any further cooling of the atoms which are in the range of Sisyphus cooling.

This condition allows us to make an important simplification to the modelling of the cooling experiment. In the calculations that follow, only Doppler cooling is considered which greatly reduces the computing time. To generate an adequate model of the lin $\perp$ lin cooling experiment in the high intensity regime as used in the experiments described in the previous chapter, would require a great deal of effort [89]. Doppler cooling is well described using a two level model [91] thus we exclude details of the hyperfine structure in the calculations. In choosing the two level model, we also assume that the excitation probability is independent of laser polarisation. This fact allows us to use the spatially averaged term of the Minogin and Serimaa model [95] as described in section 6.5. (The terms arising from the periodic nature of the standing wave in the Minogin and Serimaa model, which do depend on the polarisation, are not included for a different reason, also discussed in section 6.5.)

## 6.2 Modelled situation

We define the laser spots to have gaussian profiles, with $\frac{1}{e^2}$ radii obtained from the beam profiles measured in sections 3.4 and 5.3.

A two-dimensional gaussian intensity profile, $I(x, y)$, is given in equation 6.1

$$I(x, y) = I_0 \exp\left(-\frac{2x^2}{x_{\text{rad}}^2} - \frac{2y^2}{y_{\text{rad}}^2}\right) \tag{6.1}$$

where $I_0$ is the peak intensity at the centre of the gaussian and $x_{\text{rad}}$ and $y_{\text{rad}}$ are the $\frac{1}{e^2}$ radii of the beams in the $x$ and $y$ planes.

We have also measured the power in each of the laser beams used in the experiments (section 5.3). The power, $P$, is equal to the integral over $x$ and $y$ of the intensity distribution, that is,

$$P = \int_{-\infty}^{\infty} \int_{-\infty}^{\infty} I(x, y) \, dx \, dy \tag{6.2}$$

Using this relation, the peak intensities, $I_0$, for each of the lasers were calculated by integrating over $x$ and $y$.

It is useful to consider the laser intensities relative to the saturation intensity, $I_{\text{sat}} = 1.65 \, \text{mW/cm}^2$ for the $D_2$ transition in Rb, so that,

$$G(x, y) = \frac{I(x, y)}{I_{\text{sat}}} = G_0 \exp\left(-\frac{2x^2}{x_{\text{rad}}^2} - \frac{2y^2}{y_{\text{rad}}^2}\right) \tag{6.3}$$

where $G_0$ is the peak saturation parameter. A table showing the relevant parameters for each of the lasers is given below.

A plot showing the spatial intensity profiles of each of the three lasers is given in figure 6.1. Intensity, in units of saturation, is plotted on the vertical axis against $x$ and $y$. By definition, the probe laser was located at the origin ($x = 0$, $y = 0$) and the chopped and cooling lasers were located on the (dashed) line $y = 0$, at positions 4.1 mm and 12.4 mm to the left of the probe, respectively. These are the scaled laser
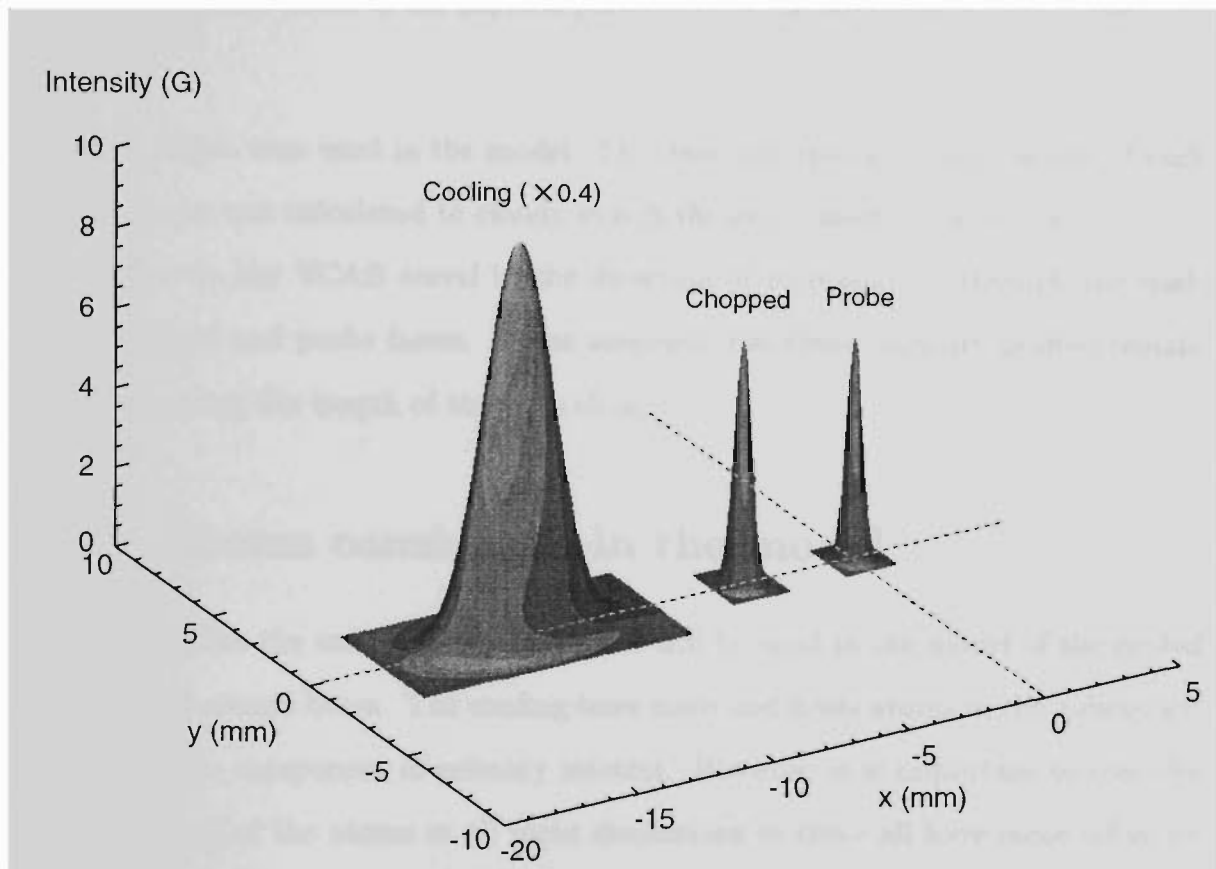
**Figure 6.1**: Spatial intensity profiles of the lasers used in the model, represented by two-dimensional gaussians. The cooling laser has been scaled down by a factor of 0.4 (from its intensity at 2 mW). The probe laser lies at the origin ($x = 0$, $y = 0$) and the chopped and cooling lasers lie at ($x = -4.1$, $y = 0$) and ($x = -12.4$, $y = 0$) respectively.

| Laser | Power (mW) | $I_0$ (mW/cm$^2$) | $G_0$ | $x_{rad}$ (mm) | $y_{rad}$ (mm) |
|---|---|---|---|---|---|
| Probe | 0.034 | 9.0 | 5.4 | 0.49 | 0.49 |
| Chopped | 0.046 | 10.3 | 6.2 | 0.54 | 0.54 |
| Cooling | 1 - 12 | 17 - 200 | 10.5 - 126 | 2.6 | 1.2 |

**Table 6.1**: Table of the physical parameters of the laser beams used in the model.

profiles which were used in the model. The intensity, spot size and position of each of the lasers was calculated to closely match the experimental conditions.

Atoms in the VCAB travel in the direction of increasing $x$, through the cooling, chopped and probe lasers. It was assumed that these intensity profiles remain constant along the length of the cell (along $z$).

## 6.3 Atoms considered in the model

Here we define the ensemble of atoms that will be used in the model of the cooled vapour cell atomic beam. The cooling laser cools and heats atoms in the $z$-direction so this is the component of primary interest. However, it is important to consider the velocities of the atoms in all three dimensions as these all have some influence on the measurements.

### 6.3.1 $Z$-velocity distribution

Because of its high intensity (up to $G = 60$), the cooling laser interacts strongly with atoms over a large range of $z$-velocities. For this reason, atoms with a large selection of $z$-velocities, $0 \pm 50$ m/s (the centre portion of the Doppler profile) were considered. At room temperature, the FWHM of the Doppler profile is 400 m/s. The number of atoms, $N(v_z)$, which lie within the velocity range $v_z$ to $v_z + dv_z$, is given by the
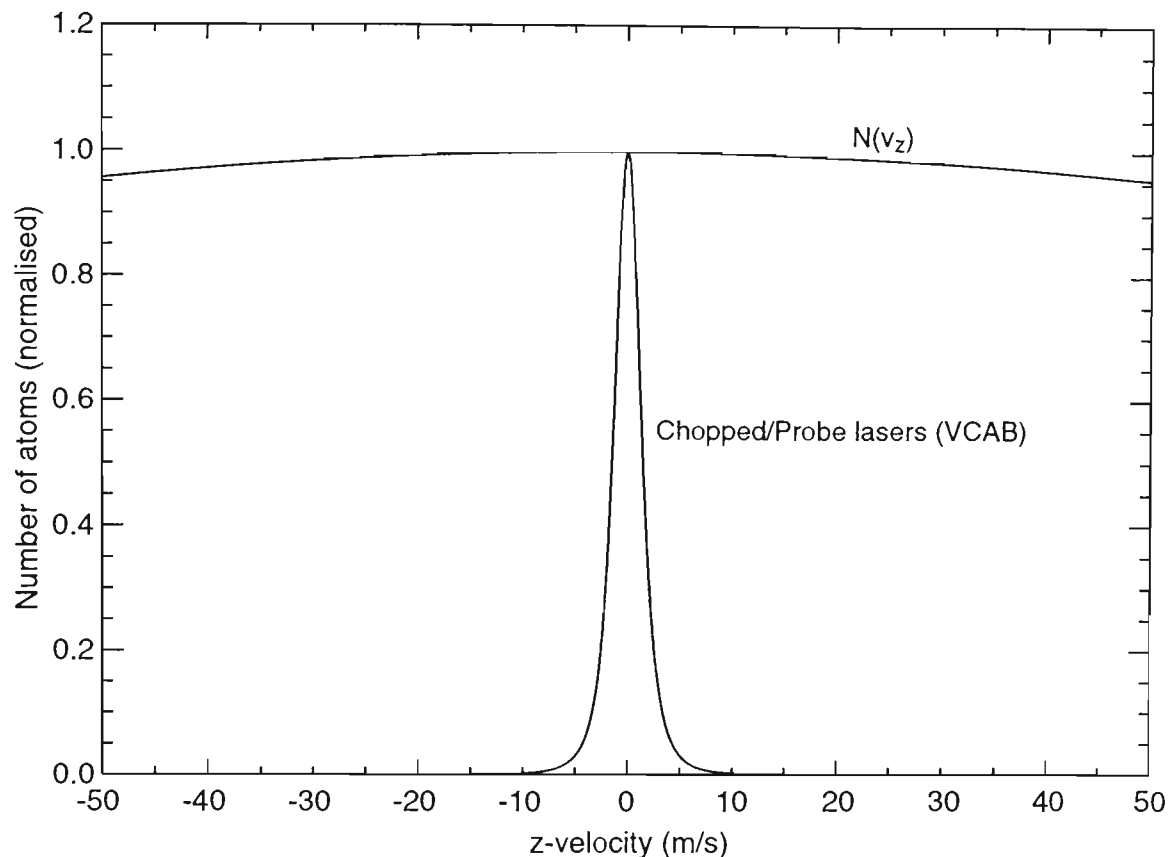
**Figure 6.2**: Initial $z$-velocity distribution of atoms, $N(v_z)$, and the combined chopped/probe lasers absorption profile (VCAB transverse velocity profile). Both plots are normalised with respect to their $v_z = 0 \, \text{m/s}$ value.

Maxwellian velocity distribution [5],

$$N(v_z)dv_z = N_0 \exp\left(-\frac{mv_z^2}{2k_B T}\right) dv_z \tag{6.4}$$

where, $N_0$ is the number of atoms with $v_z = 0$, $m$ is the mass of the atoms, $k_B$ is Boltzmann's constant and $T$ is the temperature of the atoms. This distribution has been plotted for rubidium atoms at room temperature for the range of velocities considered in the model (figure 6.2). From this distribution, we know the relative number of atoms which enter the cooling laser beam with a velocity, $v_z$.

Also shown in the figure is the transverse velocity distribution of the VCAB (as in section 3.4). The velocity range we have included extends far beyond the atoms which are normally detected in the VCAB. This was done so that any cooling effects

on atoms far from $v_z = 0$ would be accounted for.

## 6.3.2 $X$-velocity distribution

In the direction of the vapour cell atomic beam ($x$-direction) the number of atoms , $N(v_x)$, moving with a speed in the range $v_x$ to $v_x + dv_x$ is given by the Maxwellian distribution of speeds [5],

$$N(v_x)dv_x = N_0 v_x^2 \exp\left(\frac{-mv_x^2}{2kT}\right) dv_x \qquad (6.5)$$

As a first approximation however, the situation was simplified by considering only atoms moving at the mean velocity. For rubidium atoms at room temperature this velocity, $\bar{v}_x$, is 270 m/s. This simplification may effect the outcomes of the calculations as atoms which spend longer in the cooling laser will experience more cooling/heating than those which pass through more quickly. It is difficult to predict how significant this effect will be without doing the complete calculation however, the computing time required to do this would make running the program impractical.

## 6.3.3 $Y$-velocity distribution

In the plane perpendicular to both the laser propagation and atomic beam direction (vertical, $y$-direction), the situation was slightly more complicated. There are a range of $y$-velocities of atoms which contribute different amounts to the measured vapour cell atomic beam signal. To fully understand this, it is useful to look at figure 6.3. This figure shows a scaled end on view of the laser beams in the cell and their relative positions. The beam profiles for the chopped and probe lasers are circular with a $\frac{1}{e^2}$ radius of 0.54 mm and 0.49 mm respectively. The profile for the cooling laser is elliptical with $\frac{1}{e^2}$ radii of 1.2 mm and 2.6 mm.

Also shown in the figure are two possible atom trajectories (labelled A and B). Path A intersects the cooling, chopped and probe lasers at the same $y$ coordinate and passes through a relatively high intensity region of each of the lasers. Path B
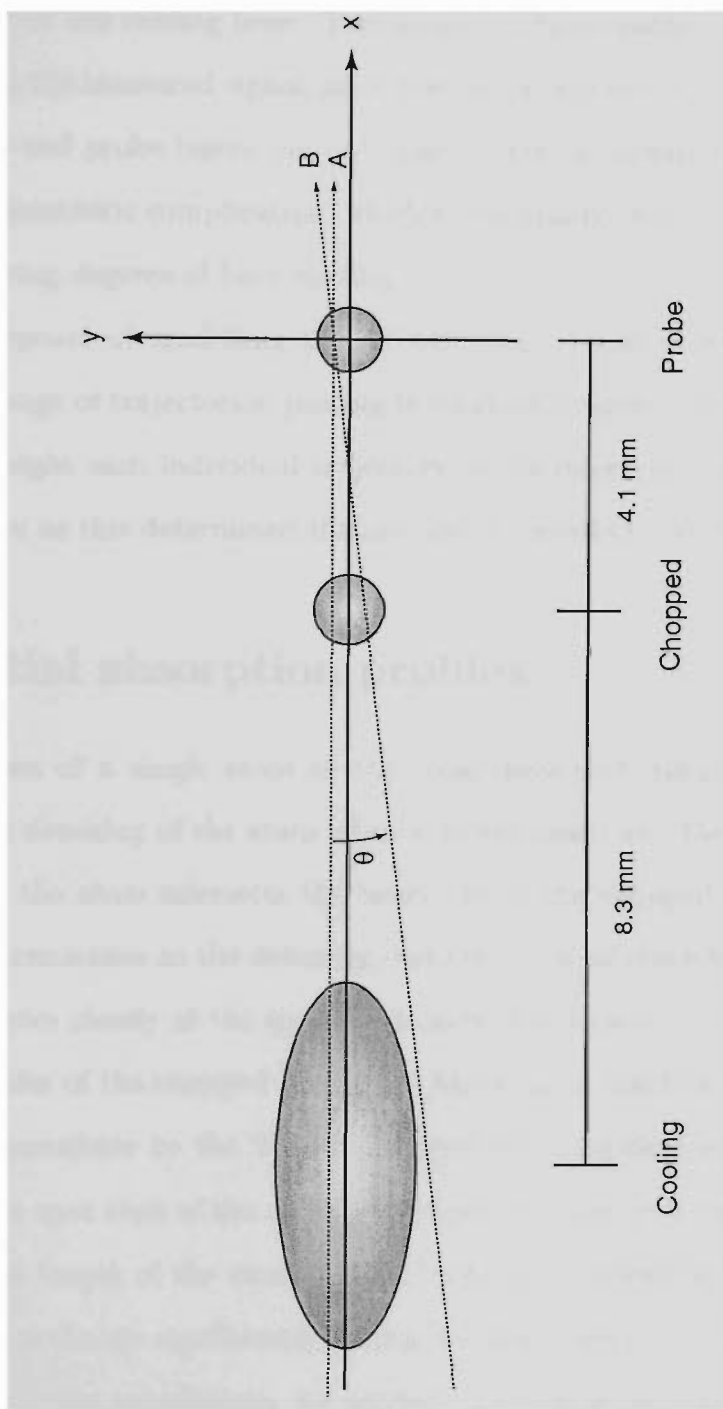
**Figure 6.3**: Positions of the three laser spots when the cell is viewed end on. The diagram is to scale. Atoms which travel on paths A and B see the same intensities of the chopped and probe lasers, yet very different intensities of the cooling laser.

however, oriented at some angle $\theta$ to the $x$-axis, experiences the same intensity of the chopped and probe lasers as an atom on path A, yet passes through a far lower intensity region of the cooling laser. Two atoms on these paths will contribute the same amount to the measured signal, since they both experience the same intensities of the chopped and probe lasers, yet only one of them is significantly cooled. This illustrates the geometric complication, which is essentially that the atoms we detect experience varying degrees of laser cooling.

For the purposes of modelling the VCAB then, it was necessary to consider atoms with a range of trajectories, passing through at a range of heights. It was also necessary to weight each individual trajectory by its interaction with the chopped and probe lasers as this determined the amount it contributes to the total signal.

## 6.4 Spatial absorption profiles

The contribution of a single atom to the total measured signal depends on the Doppler shifted detuning of the atom relative to the lasers and the optical intensity at the position the atom intersects the lasers. Both the chopped and probe lasers were locked on resonance so the detuning dependence is as described in section 3.4. Here we look more closely at the spatial intensity dependence.

The intensities of the chopped and probe lasers are a function of both $x$ and $y$. Atoms which contribute to the VCAB are generally travelling near to parallel to the $x$-axis as the spot sizes of the chopped and probe lasers ($\approx 1\,\text{mm}$) are somewhat smaller than the length of the atomic beam ($\approx 4\,\text{mm}$). Therefore, the $y$-position of the atom does not change significantly during the time it interacts with an individual laser. To simplify the calculations, we assumed that an atom crossing a laser does so at a fixed $y$, regardless of its incident angle, $\theta$, as $\theta$ will be small. Thus we can say that an atom experiences an average intensity, dependent upon its $y$-position, as it crosses a laser. By average intensity we mean the average over $x$ of the two-dimensional gaussian at a given $y$. These averages were calculated for both the

chopped and probe lasers, by averaging the gaussian between the $\frac{1}{e^2}$ $x$-radii.

From this, it is possible to determine the atoms' corresponding average absorption as a function of $y$. Both the chopped and probe lasers are tuned resonantly to their respective transitions, so, using a two-level approximation, the average absorption, $A(y)$, is given by [1]

$$A(y) = \frac{1}{2} \frac{G_{\text{ave}}(y)}{1 + G_{\text{ave}}(y)} \tag{6.6}$$

where, $G_{\text{ave}}(y)$ is the spatially averaged saturation parameter expressed as a function of $y$. These two functions have been calculated for both the chopped and probe lasers and are plotted in figure 6.4.

The absorption profiles are significantly wider than the intensity profiles because the laser intensities far exceed the saturation level ($G > 1$). This is important as it means that the effective size of the chopped and probe lasers is somewhat larger than might be expected from the intensity profiles alone. A consequence of this is that we are better able to measure atoms with larger $|\theta|$. From these profiles, we were able to calculate appropriate weighting factors to weight each atom trajectory by the $y$-coordinates at the points where they intersect the chopped and probe laser beams.

## 6.5  Cooling in a high intensity laser field

Atoms which travel through the cooling laser experience a change in their $z$-velocity. In this section, the method used to calculate this change as a function of atom velocity and the cooling laser intensity and detuning is described.

It has already been shown that the calculations can be simplified by not considering the polarisation gradient cooling with only a minor modificaton to the outcomes. Thus we only include the spontaneous or scattering force in the calculations which follow.

In a high intensity counter-propagating laser field, the spontaneous light force is no longer well described by equation 5.1. When the saturation parameter, $G = \frac{I_L}{I_S}$,
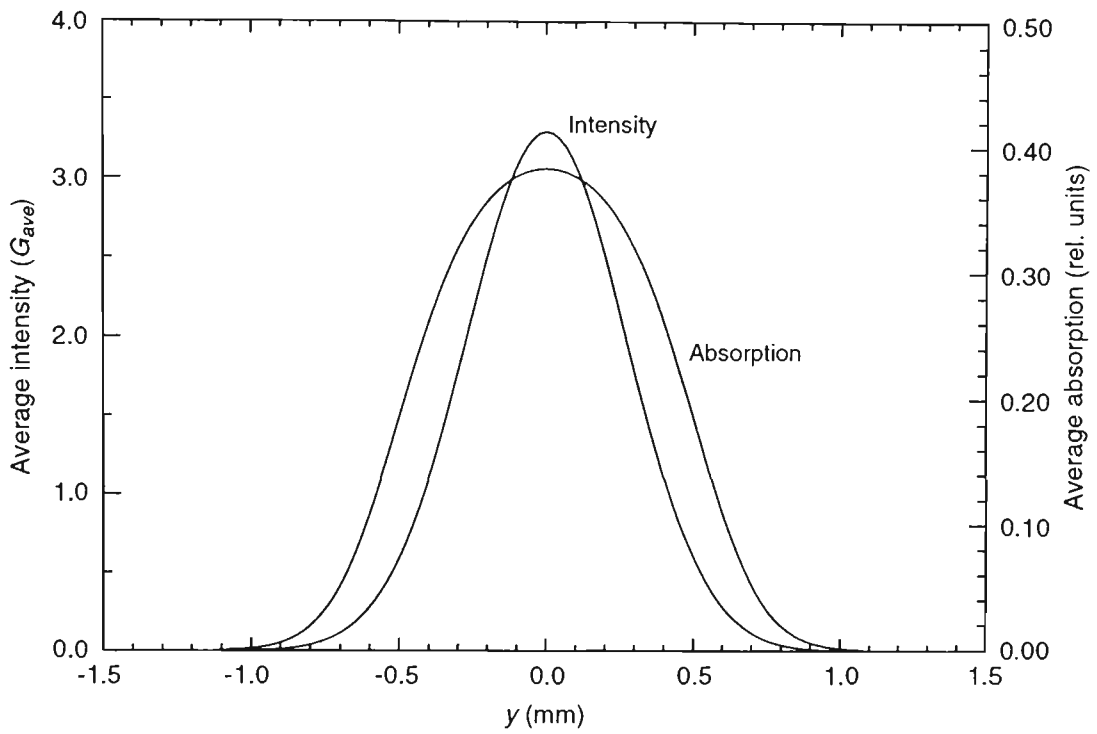
(a) Average intensity and absorption profiles of the chopped laser
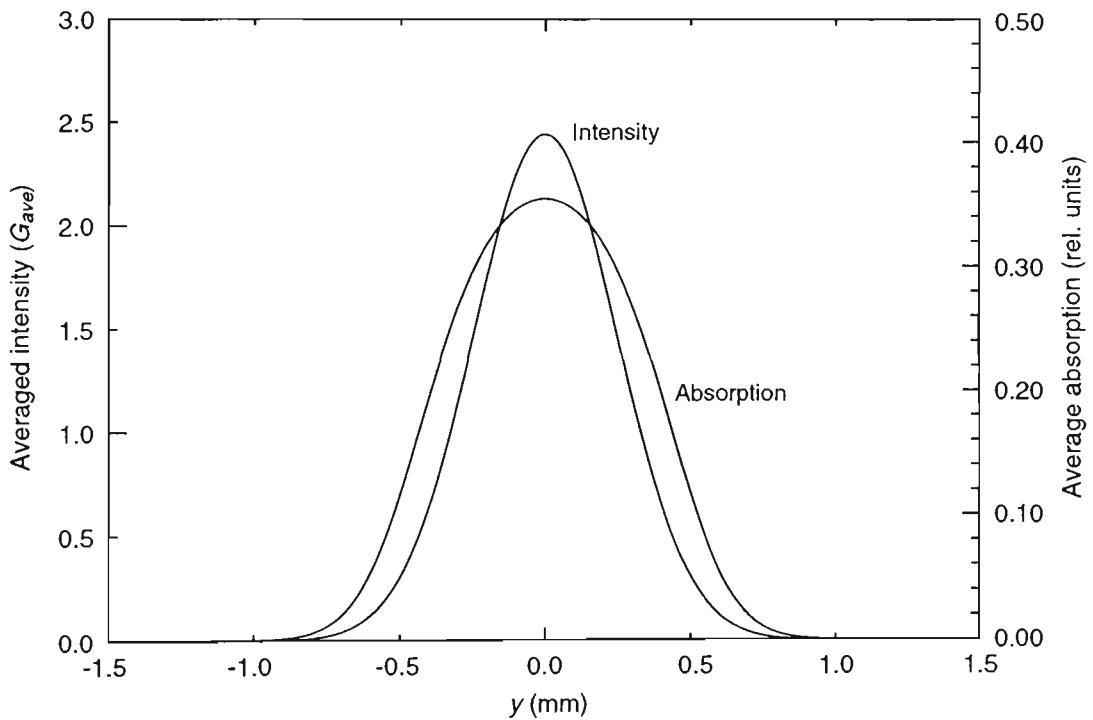


(b) Average intensity and absorption profiles of the probe laser

**Figure 6.4**: Intensity and absorption profiles of the chopped and probe lasers as a function of $y$. Intensities are given on the left axis and absorption on the right axis.

exceeds 1, other effects, primarily multi-photon processes, become important. A technique for calculating the exact spontaneous radiation pressure force on atoms in an intense laser standing wave was reported by Minogin and Serimaa in 1979 [95] and their method has been employed here. Details of the derivation are not included, but we have employed their results.

They derive an expression for the velocity dependent force a two level atom experiences in a high intensity laser standing wave. The expression for the force consists of a spatially averaged term and Fourier components which is given by equation 6.7 [95]

$$F_{total} = F^0 + \sum_{n=1}^{\infty} \left( F_n^c \cos 2nkz + F_n^s \sin 2nkz \right) \tag{6.7}$$

where $F^0$ is the spatially averaged force, $F_n^c$ and $F_n^s$ are the Fourier coefficients of the cosine and sine terms respectively, $k = \frac{2\pi}{\lambda}$ and $z$ is the atom's position along the wave. The Fourier terms account for the spatial periodicity of the electric field in a standing wave [96] (these occur with a period of $\frac{\lambda}{2}$).

In the model here, we choose to calculate only the spatially averaged term for the following reason. These periodic terms are most important for atoms whose energies are of the same order as the depth potential wells formed by the standing wave [96]. For atoms which travel over many nodes and antinodes of the standing wave, these terms will average to zero over several periods of the cosines and sines. In our experiment, for atoms to travel over only one or fewer $\frac{\lambda}{2}$ periods in the time they are in the cooling laser they would need to be moving with a $z$ velocity less than $2\,\mathrm{cm/s}$. As we have already made the approximation that atoms moving with $v_z < 1\,\mathrm{m/s}$ will not significantly alter our results (in eliminating polarisation gradient cooling), calculating only the spatially averaged force $F^0$ is a far less serious simplification as the velocity range influenced by the oscillating terms in the Fourier expansion is much smaller.

## 6.5.1 The cooling force

The spatially averaged (along the axis of the standing wave) spontaneous force, $F^0$, on a two-level atom in a high intensity standing wave is given by [95].

$$F^0 = -2\hbar k\gamma \frac{\text{Im}(A)}{1 + 2\text{Re}(Q)} \tag{6.8}$$

where Im and Re refer to the real and imaginary parts of the complex numbers,

$$A = \frac{\Delta}{\gamma + ikv_z} Q . \tag{6.9}$$

and $Q$, which is the continued fraction given by 6.10

$$Q = \cfrac{p_0}{1 + \cfrac{p_1}{1 + \cfrac{p_2}{1 + \cfrac{p_3}{1 + ...}}}} \tag{6.10}$$

where the numerators, $p_n$, are given by 6.11

$$p_n = G\frac{\gamma + in_1kv_z}{2\gamma + in_2kv_z} \frac{2\gamma^2}{[\Delta^2 + (\gamma + in_1kv_z)^2]} \tag{6.11}$$

with,

$$n_1 = \begin{cases} n+1 \\ n \end{cases} , \quad n_2 = \begin{cases} n & n \text{ even} \\ n+1 & n \text{ odd} \end{cases}$$

$\gamma = \frac{\Gamma}{2}$ is equal to half the spontaneous decay rate, $\Delta = \omega_L - \omega_0$ is the laser detuning from resonance, $v_z$ is the velocity of the atom in the plane of the standing wave and the other variables are as in section 5.1.2.

A computer program was written to calculate the spontaneous force as a function of laser intensity, detuning and atom velocity. A three-dimensional plot of this is given in figure 6.5. The laser detuning was chosen to be $-3\gamma$ and the force is plotted for the intensity range $1 < G < 100$.

For low intensities, the force converges to that calculated in section 5.1.2.1. At
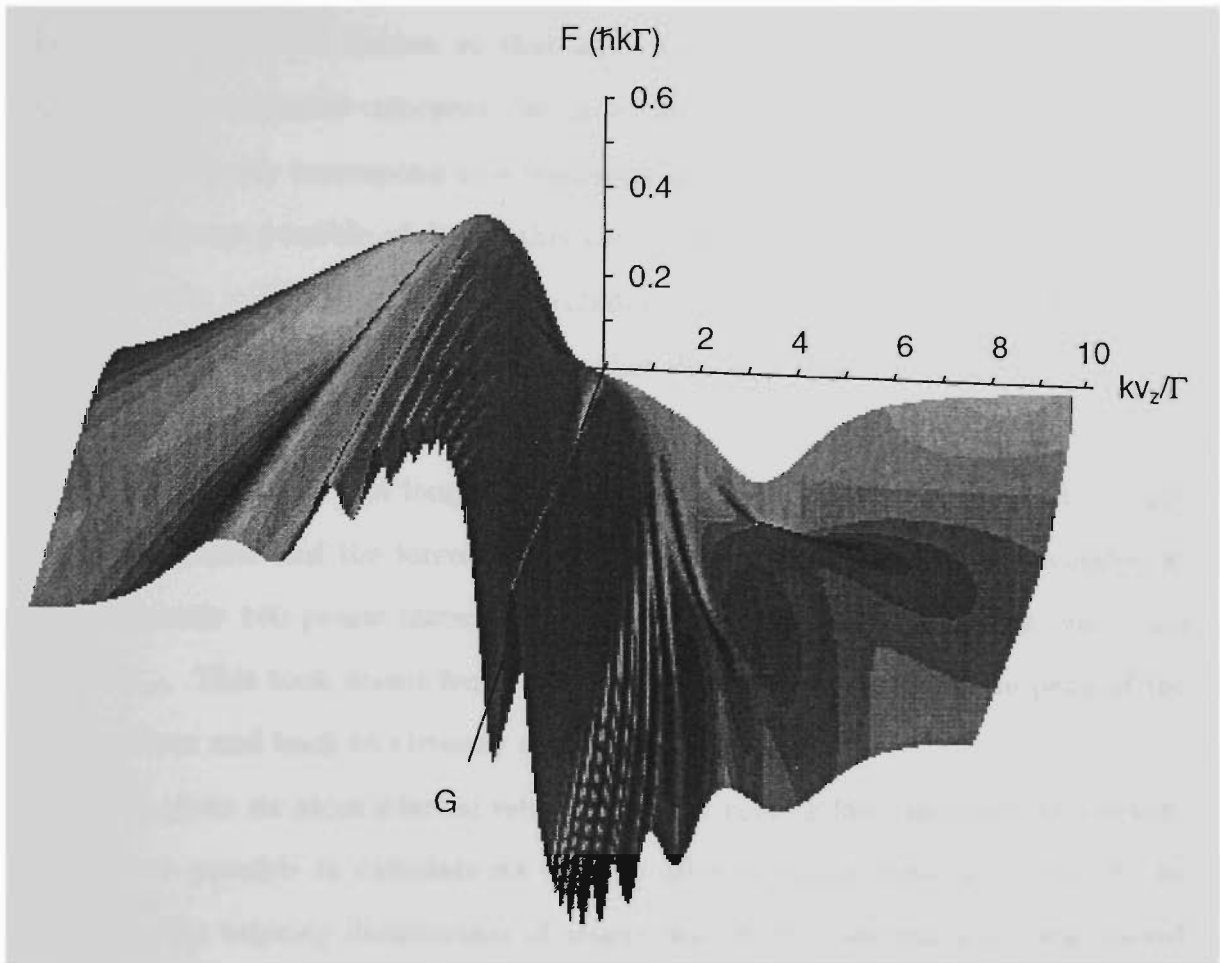
**Figure 6.5**: Spontaneous force on a two-level atom in a high intensity standing wave plotted over the range $1 < G < 100$ for a laser detuning of $\Delta = -3\gamma$. Atom velocity and force are expressed in normalised units.

higher intensities however, the force curves appear quite different to the low intensity case. For very small atomic velocities, the laser actually heats the atoms (characterised by the change of sign of the force curve near $v_z = 0$). Also visible on the plot are the Doppleron resonances due to the multi-photon processes [95]. These are indicated by the ripples on the force curve.

## 6.5.2   Atomic velocities through the cooling laser

Knowing the force on an atom in the cooling laser, the change in its velocity, $dv_z$, can be calculated using $dv_z = \frac{F(v_z)}{m} dt$ where, $dt$ is a short time interval. In the model, atoms were stepped across the cooling laser in time intervals of $dt = 200\,\text{ns}$.

This value of $dt$ was chosen so that any changes $dv_z$ would be calculated using appropriately adjusted velocities. Secondly, any changes in velocity which occur in this time will only correspond to a negligibly small change in the force experienced. (The maximum possible of $dv_z$ in this time is approximately four recoil velocities, $4v_r$, where $v_r = \hbar k/m = 6\,\text{mm/s}$ for rubidium. This corresponds to 1/200th of the scaling on the force curve, and it is clear that the force does not change significantly over this scale.)

Atoms (travelling with longitudinal velocity $v_x = 270\,\text{m/s}$) were stepped through the cooling laser and the force, $F$, and change in velocity, $dv_z$, were calculated at approximately 140 points through the gaussian cooling beam extending out to 1.5 times $x_{\text{rad}}$. This took atoms from virtually zero intensity, through the peak of the cooling laser and back to virtually zero again.

Thus, given an atom's initial velocity and the cooling laser intensity and detuning, it was possible to calculate its velocity after emerging from the laser. As an example, the velocity distribution of atoms described in section 6.3.1 was passed through the centre of the cooling laser, detuned 3 MHz below resonance and with peak intensities $G_0$ of 1, 10 and 100. The emergent velocity distributions are shown in figure 6.6.

A large peak of cooled atoms is collected in the centre of the distribution. The size of the peak increases with laser intensity. Some smoothing has been performed to reduce noise arising from the binning procedure (emergent atoms were binned into 0.05 m/s wide velocity "buckets").

Also shown in the figure is the transverse velocity distribution of the uncooled VCAB as calculated in section 3.4. It is clear, that when the cooling laser is on, there are more atoms lying in the velocity region of the VCAB than there were in figure 6.2.

With the cooling laser was tuned above resonance we would see the opposite effect, that is, the emergent atoms would have a velocity distribution which dips, instead of peaks, around $v_z = 0$. Thus there would be fewer atoms in the velocity
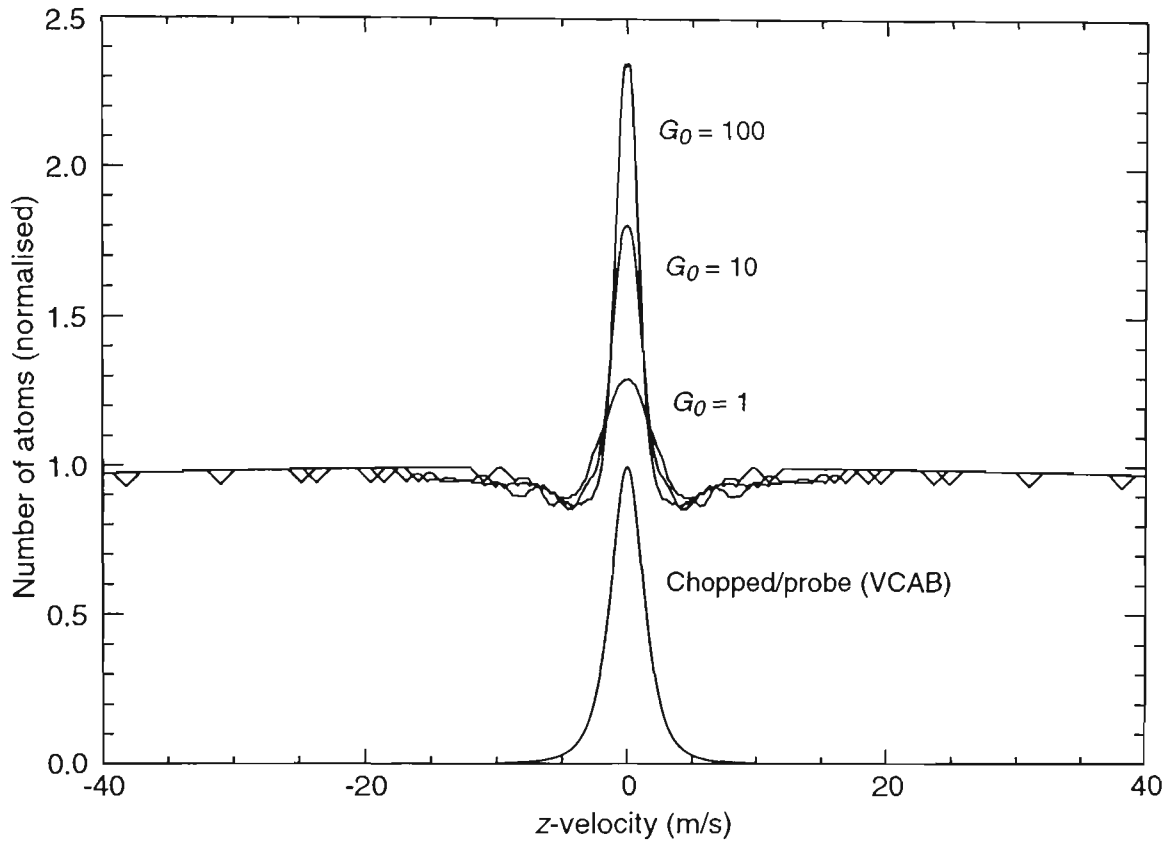
**Figure 6.6**: Predicted velocity distribution of atoms emerging from the cooling laser for various cooling laser intensities. The transverse velocity distribution of the VCAB is also shown. As the intensity of the cooling laser increases, more atoms are placed in the velocity range excited by the chopped laser.

region excited by the chopped laser and detected by the probe leading to fewer atoms in the beam.

## 6.5.3 Number of atoms in the VCAB

The total number of atoms in the VCAB is given by the convolution of the two distributions shown figure 6.6. That is, the velocity distribution of the atoms emerging from the cooling laser and the combined absorption profiles of the chopped and probe lasers. In the present case, this is given by the area under the product of the two distributions. Finding this yields a figure directly proportional to the number of atoms in the beam which we expect to be directly proportional to the lock-in signals measured in the experiment.

## 6.6 Results

PV-Wave [97] code was written to calculate the force and change in velocity for atoms on a range of trajectories and is given in appendix D. The calculations were performed for atoms travelling through the lasers at positions ranging from either side of the $\frac{1}{e^2}$ radii and angles from $-0.17 \le \theta \le +0.17$ rad. This covered all possible trajectories that could contribute to the measured signals. Each of these trajectories was weighted by the average absorption experienced in both the chopped and probe lasers. These weighted trajectories were then summed to give the total expected signal for a particular cooling laser detuning and intensity.

The calculations were performed for all cooling laser detunings and intensities used in the experiments. A plot showing the calculated relative number of atoms in the VCAB as a function of cooling laser detuning is given in figure 6.7 for a range of cooling laser intensities.

The results display very similar trends to the experimental results in figure 5.10, with an increase in the number of atoms in the beam when the cooling laser is red detuned and a decrease in the number of atoms when the laser is blue detuned. The greatest deviations from the zero detuning level occur at detunings of approximately $\pm \Gamma$ with the size of the deviations increasing with laser intensity. The maxima and minima also shift away from resonance with increasing laser intensity.

## 6.7 Comparison of experimental and theoretical results

It is difficult to make direct comparisons between the theoretical (figure 6.7) and experimental (figure 5.10) results as both sets of data are plotted on arbitrary scales with partially arbitrary background levels (particularly for the experimental results). As well as this, the model takes no account of optical pumping effects. The theory retains all atoms in the system and does not attempt to predict how these optical
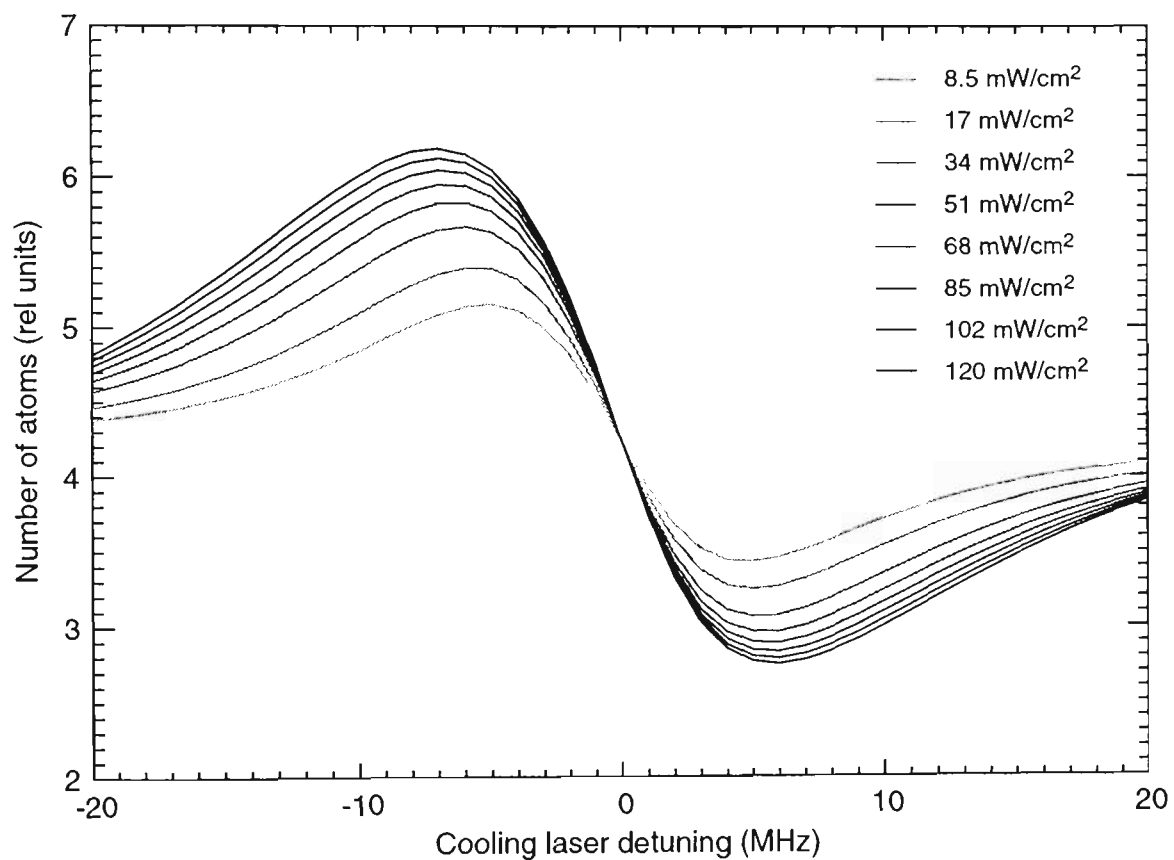
**Figure 6.7**: Theoretical plot showing the effect of the cooling laser on the VCAB signal (number of atoms in the VCAB) as a function of cooling laser detuning. Cooling laser intensities are given on the graph.

pumping effects alter the measured signal.

A simple way to take the optical pumping into account is to assume that the optical pumping effects are essentially flat over the detuning range studied. This is not unreasonable as the most important pumping mechanism (loss to the $F' = 1$ ground state) will be essentially the same over the relatively small range of detunings (from the $F' = 2$ to $F = 2$ transition) scanned over.

Given this assumption, we can apply a linear scaling factor and offset to the theoretical curves to account for the optical pumping and background differences and then be in a position to make better comparisons with the experiment. A least squares fitting routine was used to determine the appropriate scaling factors and offsets for the theoretical data to give the closest agreement with the experiment. A plot showing the adjusted theoretical curves and the experimental data for all laser intensities is given in figures 6.8 and 6.9. These plots show excellent agreement for all laser intensities.

A table showing the calculated scaling factors and offsets found by the least squares fitting is given in table 6.2. These scaling factors and offsets have been plotted against laser intensity in figures 6.10 and 6.11. The error bars were obtained from the uncertainty in the least squares fitting parameters.

As the primary source of optical pumping is via excitation to the $F = 2$ excited state leading to loss to the $F' = 1$ ground state, we can predict what this loss will look like in a relatively simple manner. The excitation probability to the $F = 2$ state, $\rho_{22}$, goes as,

$$\rho_{22} = \frac{1}{2} \frac{G}{4\left(\frac{\Delta^2}{\Gamma^2}\right) + G + 1} \tag{6.12}$$

where $G$, $\Delta$ and $\Gamma$ are as defined previously. However, as we are far detuned from the $F = 2$ excited state ($\approx 267\,\text{MHz}$), we have $\frac{\Delta^2}{\Gamma^2} \gg G$ and 6.12 reduces to,

$$\rho_{22} = \frac{G}{8\left(\frac{\Delta^2}{\Gamma^2}\right)} \tag{6.13}$$

That is, the amount of optical pumping will increase linearly with laser intensity.
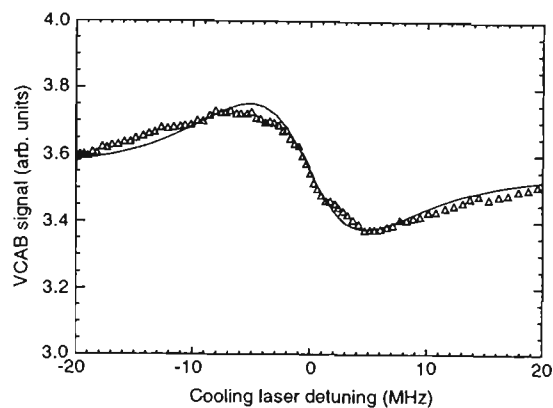
(a) Laser intensity = 8.5 mW/cm²
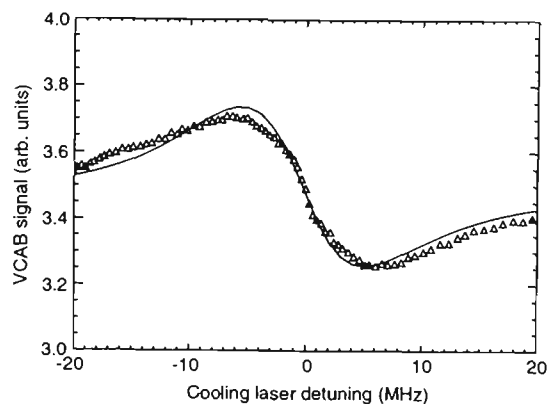
(b) Laser intensity = 17 mW/cm²
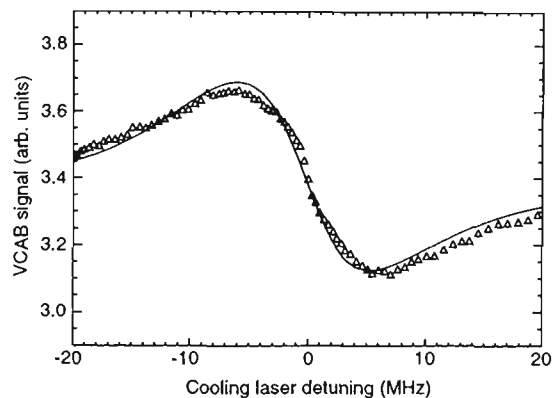
(c) Laser intensity = 34 mW/cm²
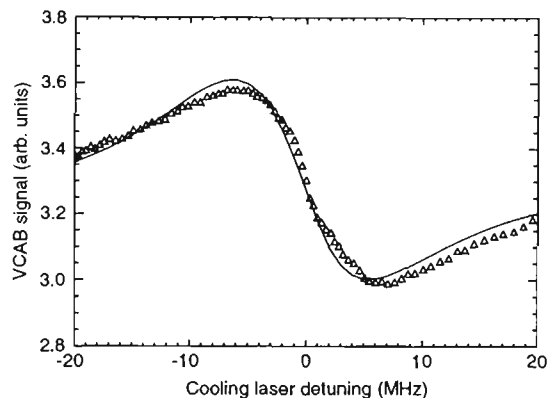
(d) Laser intensity = 51 mW/cm²

**Figure 6.8**: Plots of the experimental and theoretical results for the laser cooling experiment. The theoretical results have been scaled to account for the optical pumping effects.
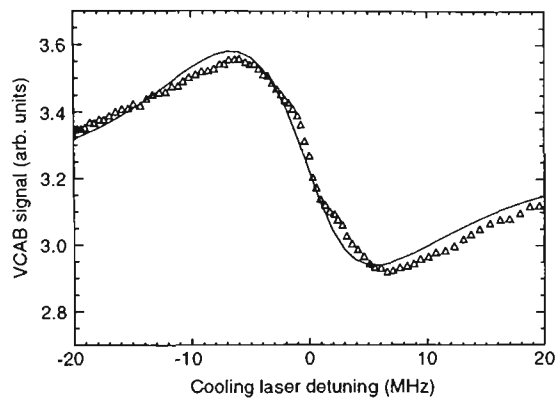
(a) Laser intensity = 68 mW/cm$^2$
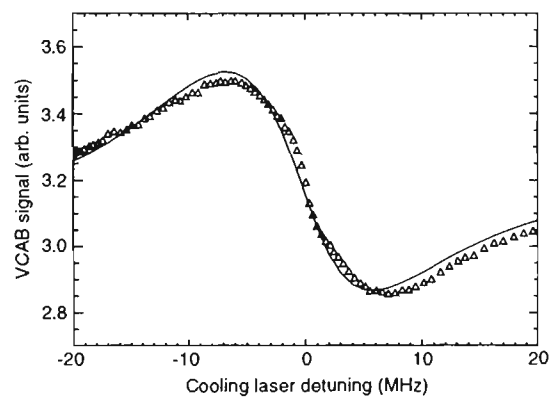
(b) Laser intensity = 85 mW/cm$^2$
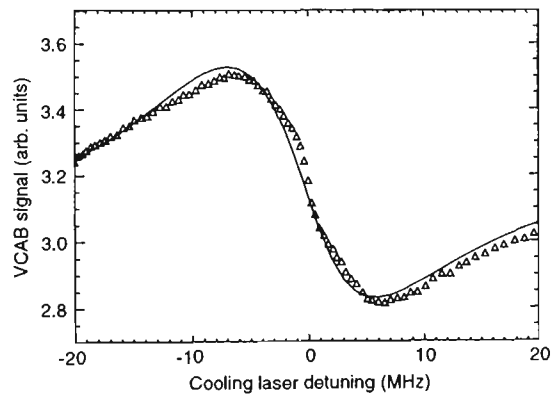
(c) Laser intensity = 100 mW/cm$^2$

**Figure 6.9**: Plots of the experimental and theoretical results for the laser cooling experiment. The theoretical results have been scaled to account for the optical pumping effects.

| Cooling laser intensity (mW/cm$^2$) | Scaling factor (arb. units) | Offset (arb. units) |
|---|---|---|
| 8.5 | 0.218 ± 0.0024 | 2.63 ± 0.029 |
| 17 | 0.222 ± 0.0025 | 2.54 ± 0.028 |
| 34 | 0.217 ± 0.0024 | 2.46 ± 0.027 |
| 51 | 0.212 ± 0.0025 | 2.38 ± 0.029 |
| 68 | 0.209 ± 0.0026 | 2.34 ± 0.029 |
| 85 | 0.205 ± 0.0025 | 2.28 ± 0.028 |
| 100 | 0.209 ± 0.0025 | 2.25 ± 0.027 |

**Table 6.2**: Table of the scaling factors and offsets applied to the theoretical data to fit it to the experimental laser cooling results.

Looking at figures 6.10 and 6.11, this linear dependence becomes evident. The straight line fits shown on the plots indicate what this "linear" optical pumping would do to the measured signals.

As can be seen, the straight lines represent the data reasonably well. The gradient (relative to the magnitude) of the offsets line is about twice as steep as the scaling factors line, suggesting that the optical pumping has a stronger effect on the offsets than the scaling. If there was no optical pumping, we would expect the scaling factors and offsets to be the same for all laser intensities.

It is likely that better fits to these scaling factors and offsets could be obtained using more complicated functions. However, without performing a detailed optical pumping calculation, it is difficult to know what form these function should take. Given the uncertainties in the experimental data and the limitations of the model, the linear approximation for optical pumping provides a reasonable way of separating the laser cooling effects from the optical pumping. The good agreement between the experimental and theoretical plots of figures 6.8 and 6.9 helps confirm the validity of this approach.
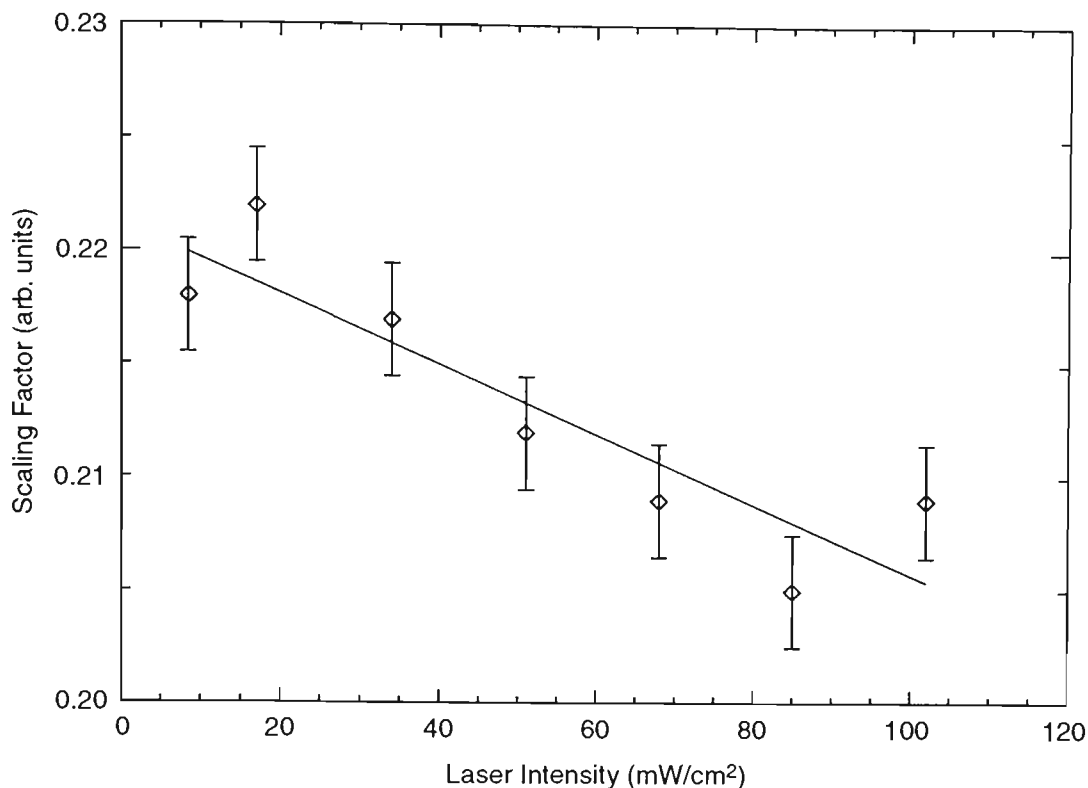
**Figure 6.10**: Scaling factors used in fitting the theoretical to experimental results for the laser intensities used. A straight line fit to this is also shown to illustrate the effect of "linear" optical pumping.

## 6.8  Discussion

The model developed here provides a reasonable description of the effect of the cooling laser on the VCAB signals. The predictions of the model agree well with the experimental results indicating that the signals measured in chapter 5 provide clear evidence of laser cooling. The raw predictions of the theory show cooling effects which exceed the experimental observations. When the theory is scaled to take into account the arbitrary scaling, unknown background level and optical pumping the agreement between the two is excellent. However, several other details could be included in the model to make it a more accurate representation of the experiment.

Probably the greatest deficiency in the theoretical description of the cooling experiment is the failure to properly calculate the optical pumping. Without a re-pumping laser, we would not expect to measure all of the cooled atoms as these have interacted most strongly with the cooling laser and are therefore most susceptible to
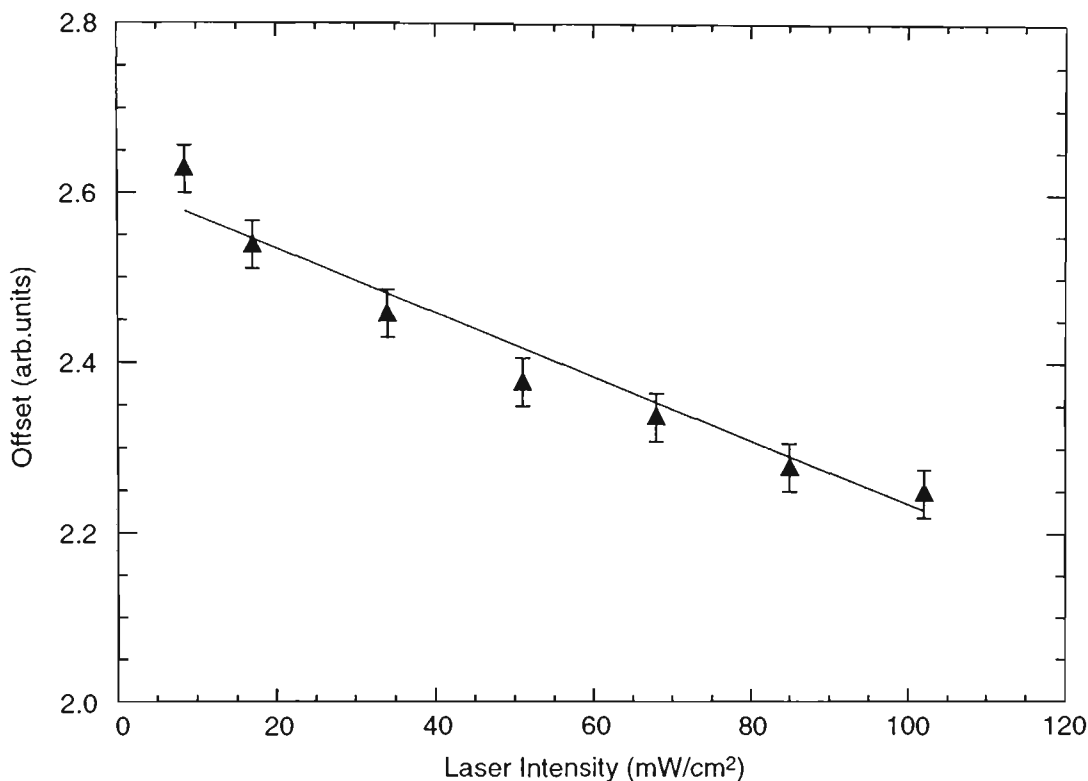
**Figure 6.11**: Offsets used in fitting the theoretical to experimental results for the laser intensities used. A straight line fit to this is also shown to illustrate the effect of "linear" optical pumping.

being pumped out. The way we have accounted for optical pumping effects above is not particularly accurate as it assumes that all atoms experience the same degree of pumping, independent of the cooling they experience. A better approach would be to calculate the optical pumping for each of the atom trajectories, as a function of the cooling laser detuning and intensity and include this as a weighting factor for each trajectory. This would provide a more accurate prediction of the number of cooled atoms we would expect to detect in the VCAB.

In addition to the optical pumping, the cooling force is only calculated for a two-level atom. A more detailed calculation of the cooling force, such as that given by Williams et al. [89], would be more appropriate. Their technique, which is based on the full multi-level atomic structure, includes polarisation gradient cooling as well as Doppler cooling. They reported very good agreement between experimental and theoretical results for one-dimensional lin ⊥ lin cooling of a conventional atomic

beam. Techniques like those described in [89] could be implemented here to calculate a more accurate force curve. This should lead to more accurate predictions of the cooled velocity distributions and hence the observed signals.

It is also possible that in the experiment the laser beams were not aligned perfectly to lie on the same $x$-axis. A small misalignment of the beams means that the coldest atoms would not travel through the centre of both the chopped and probe lasers. This would also lead to a drop in size of the measured cooling effects and reduce the scaling factors obtained when fitting the theoretical to experimental data.

## 6.9 Conclusion

In this chapter, a model to describe the laser cooling experiment has been developed. The predictions of the model are in very good agreement with the experimental results indicating that the model provides a good representation of the experiment. There is scope for further development of the model and some suggestions to this effect have been given.

By analysing the theoretical results (which take no account of the optical pumping effects) we were able to determine approximately the optical pumping effects and separate these from the true cooling features. This verifies that the VCAB provides us with a useful tool for the study of laser cooling.

# Chapter 7

## CONCLUSIONS

The work presented in this thesis has primarily been concerned with the creation of a usable atomic beam inside a sealed glass vapour cell. This has been achieved by selecting and detecting atoms travelling between, and orthogonal to, two adjacent spatially separated laser beams. The usefulness of the scheme has been demonstrated by implementing it in the study of phenomena which generally require a conventional atomic beam.

In chapter 2, the lasers necessary to perform the vapour cell atomic beam experiments were described. The design and construction of two types of external cavity laser diode systems, based on the work of [7] and [19], was detailed. These lasers were then characterised, tested and locked to spectral features of the rubidium $D_2$ line. Two locking techniques were tested and an AC locking system (based on the scheme of [31]) was found to be best suited for the present application. Both types of ECLD could be locked for periods of several hours, with linewidths less than 2 MHz, to the transitions required for later experiments.

Chapter 3 describes the concept and demonstration of the vapour cell atomic beam experiment. A velocity selective optical pumping scheme, along with lock-in detection, was used to select and measure atoms travelling from one laser to another, creating a ribbon atomic beam from within a gas of rubidium atoms. The transverse velocity distribution of the VCAB was found to have a full width at half maximum of 6 m/s. This compares quite well with conventional atomic beams which typically have transverse velocity spreads of 1-2 m/s. The beam in a vapour cell provides a novel and practical way to isolate and study atoms moving in a well defined direction.

One experiment which highlighted the usefulness of the vapour cell atomic beam was described in chapter 4. Using a relatively simple arrangement, Larmor precession of spin polarised atoms in a magnetic field was observed. The results demonstrate that the VCAB provides a useful way to detect and study the time evolution of an ensemble of polarised atoms. Some further improvements to the experimental conditions and theoretical treatment given in this chapter would help to resolve the discrepancies between the two. Although, as the review of the literature highlighted, there has been some inconsistencies in previously reported results. This indicated that others have also had difficulty with the experiment and that it is highly sensitive to small non-uniformities in the applied magnetic field. However, as the measured signals displayed the expected trends with magnetic field and beam separation, it was clear that Larmor precession of atomic polarisation was responsible for the observed results.

Another experiment which demonstrated the usefulness of the VCAB was presented in chapter 5. One-dimensional laser cooling of the vapour cell atomic beam was observed in an analogous way to transverse cooling of a conventional atomic beam. An increase in the number of atoms with low velocities, in one-dimension, was observed when a cooling laser was added prior to the chopped laser. As the detuning of this laser was scanned below (above) resonance, an increase (decrease) in the number of atoms in the velocity range of the VCAB was measured. This followed the expected behaviour with the strongest cooling and heating observed at detunings around one natural linewidth away from resonance.

To further understand the results of the cooling experiment, a theoretical model to describe the laser cooling experiment was developed and presented in chapter 6. Whilst the calculations were based only on Doppler cooling, the agreement between the experimental and theoretical predictions is very good. Optical pumping effects have been dealt with in a simple manner in the model yet close agreement was still observed. The significance of the model was to show that the observed experimental traces did provide clear evidence of laser cooling and to demonstrate

a way of separating the optical pumping effects from the cooling. Using relatively simple arguments, it was possible to extract the effects of optical pumping from the measured signals.

It is also of interest to envisage ways in which the vapour cell atomic beam could be made more useful. Better transverse velocity resolution is desirable and an idea which would make this possible has recently been suggested to us [98].

Raman transitions provide a coherent way to transfer atomic population. With two phase coherent lasers separated in frequency by the $F' = 1$ to $F' = 2$ ground state splitting, it is possible to shift population from one ground state to the other without directly involving an excited state [54]. Therefore the velocity width of the atoms which take part in the interaction is no longer limited by the lifetime of the excited state. Other factors, such as the laser linewidth, would then determine the resolution limits. If we were to replace the chopped laser with two lasers inducing a stimulated Raman transition, the transverse velocity spread of the labelled atoms would drop markedly.

With the velocity selectivity achievable using a Raman technique, resolution comparable to, or perhaps even better than, that of real atomic beams should be achievable. This would mean laser cooling experiments should easily be able to detect polarisation gradient cooling and other cooling mechanisms which have previously only been observable with conventional atomic beams or trapped atoms.

Another scheme we have considered which would allow point-to-point rather than beam-to-beam measurements involves a two-photon labelling and detection scheme. In this scheme, two laser beams, which intersect each other at 90°, are required at both the labelling and detection regions. The labelling would be performed by one pair of lasers, the first tuned from the $5S_{\frac{1}{2}}$ $F' = 2$ to $5P_{\frac{3}{2}}$ $F = 3$ $D_2$ transition in $^{87}$Rb. The second labelling laser, which crosses the first at 90°, would be tuned to the $5P_{\frac{3}{2}}$ to $5D_{\frac{3}{2}}$ transition and only this laser would be chopped. With this scheme, atoms excited by the first laser would generally all relax back down to the $F' = 2$ ground state. However, if the second laser excites atoms to a $5D_{\frac{3}{2}}$ level with a low hyperfine

quantum number, then a significant number of these atoms would relax back down to the $F' = 1$ ground state. Thus yielding some optical pumping and a mechanism to label atoms. These atoms would originate only from the point where the two laser beams crossed.

The detection process would involve the same combination of crossed lasers. One laser would be used to excite atoms up to the $5P_{\frac{3}{2}}$ $F = 3$ level and then the detection would be performed on the excited state transition. That is, the transmission of the laser tuned to the $5P_{\frac{3}{2}}$ to $5D_{\frac{3}{2}}$ transition would be measured on the photodiode and sent to the lock-in. This scheme still only requires two lasers yet creates an atomic beam which more closely resembles a real beam in that the two crossed lasers define two apertures through which atoms in the beam can travel. Such a scheme may prove more useful as it would provide a geometry similar to that of a conventional beam, however, it would suffer from a greatly reduced signal to noise ratio.

The techniques described in this thesis provide a new way of studying some aspects of atomic physics and laser/atom interactions without the need for complicated apparatus. Many research groups can not afford the money or time to construct the atomic beam systems which have generally been required for the experiments described here. This work is a step on the way towards the attractive goal of performing more sophisticated atom optics in a sealed vapour cell. Achieving this would make many of the popular topics in modern atomic physics, more accessible to less established researchers, and bring interesting applications, such as compact and portable atom optical devices, closer to realisation.

# BIBLIOGRAPHY

[1] W Demtröder. *Laser spectroscopy*. Springer-Verlag, Berlin, 2nd enlarged edition, 1996.

[2] N F Ramsey. *Molecular beams*. Oxford University Press, Oxford, 1956.

[3] K J Ross and B Sonntag. High temperature metal atom beam sources. *Rev. Sci. Instrum.*, 66(9):4409–4433, 1995.

[4] MacGillivray W R, Pegg D T, and Standage M C. *Opt. Comm.*, 25:255, 1978.

[5] F Reif. *Fundamentals of statistical and thermal physics*. McGraw-Hill, Singapore, international edition, 1985.

[6] C Wieman and T W Hänsch. Doppler-free laser polarization spectroscopy. *Phys. Rev. Lett.*, 36(20):1170–1173, 1976.

[7] K B MacAdam, A Steinbach, and C E Wieman. A narrow-band tunable diode laser system with grating feedback and a saturated absorption spectrometer for Cs and Rb. *Am. J. Phys.*, 60:1098–1111, 1992.

[8] C E Wieman and L Hollberg. Using diode lasers for atomic physics. *Rev. Sci. Instrum.*, 62(1):1–20, 1991.

[9] J C Camparo. The diode laser in atomic physics. *Contemp. Phys.*, 26(5):443–477, 1985.

[10] B Bölger and J C Diels. Photon echoes in Cs vapour. *Phys. Lett. A*, 28:401–402, 1968.

[11] S Siahatgar and U E Hochuli. Display of the 8521 Å line of cesium utilising a swept GaAs laser. *I.E.E.E. J. Quant. Electron.*, 5(6):295–297, 1969.

[12] U Hochuli, P Halderman, and S Siahatgar. Display of the 8521 Å cesium hyperfine lines using a swept GaAs laser. *J. Appl. Phys.*, 40(8):3374–3375, 1969.

[13] A S Pine, C J Glasbrenner, and J A Kafalas. Pressure-detuned GaAs diode-laser absorption spectroscopy of Xenon hyperfine structure. *I.E.E.E. J. Quant. Electron.*, 9(8):800–807, 1973.

[14] J C Camparo and C M Klimcak. Laser spectroscopy on a "shoestring". *Am. J. Phys.*, 51(12):1077–1081, 1983.

[15] M G Boshier, D Berkeland, E A Hinds, and V Sandoghar. External-cavity frequency-stabilization of visible and infrared semiconductor lasers for high resolution spectroscopy. *Opt. Comm.*, 85:355–359, 1991.

[16] K C Harvey and C J Myatt. External-cavity diode laser using a grazing-incidence diffraction grating. *Opt. Lett.*, 16(12):910–912, 1991.

[17] S Filimonov and J Borysow. Long-range tunable diode laser. *Appl. Opt.*, 34(3):438–443, 1995.

[18] L Ricci, M Weidemüller, T Esslinger, A Hemmerich, C Zimmermann, V Vuletic, W König, and T Hänsch. A compact grating-stabilized diode laser system for atomic physics. *Opt. Comm.*, 117:541–549, 1995.

[19] A S Arnold, J S Wilson, and M G Boshier. A simple extended-cavity diode laser. *Rev. Sci. Instrum.*, 69(3):1236–1239, 1998.

[20] J Bowie, J Boyce, and R Chiao. Saturated-absorption spectroscopy of weak-field Zeeman splittings in rubidium. *J. Opt. Soc. Am. B*, 12(10):1839–1842, 1995.

[21] H S Lee, S E Park, J D Park, and H Cho. Zeeman effect in the saturation spectroscopy of the $^{87}$Rb $D_2$ line. *J. Opt. Soc. Am. B*, 11(4):558–563, 1994.

[22] C Monroe, H Robinson, and C Wieman. Observation of the ceasium clock transition using laser cooled atoms in a vapour cell. *Opt. Lett.*, 16(1):50–52, 1991.

[23] A Clairon, C Salomon, S Guellati, and W D Phillips. Ramsey resonance in a Zacharias fountain. *Europhys. Lett.*, 16(2):165–170, 1991.

[24] C Wieman, G Flowers, and S Gilbert. Inexpensive cooling and trapping experiment for undergraduate laboraroties. *Am. J. Phys.*, 63(4):317–330, 1995.

[25] U Schünemann, H Engler, M Zielonkowski, M Weidemüller, and R Grimm. Magneto-optic trapping of lithium using semiconductor lasers. *Opt. Comm.*, 158:263–272, 1998.

[26] H Ludvigsen, A Äijälä, A Pietiläinen, H Talvitie, and E Ikonen. Laser cooling of rubidium atoms in a vapour cell. *Physica Scripta.*, 49:424–428, 1994.

[27] M H Anderson, J R Ensher, M R Matthews, C E Wieman, and E A Cornell. Observation of Bose-Einstein condensation in a dilute atomic vapour. *Science*, 269:198–201, 1995.

[28] A Hemmerich, D H McIntyre, D Schropp Jr., D Meschede, and T W Hänsch. Optically stabilised narrow linewidth semiconductor laser for high resolution spectroscopy. *Opt. Comm.*, 75(2):118–122, 1990.

[29] D M Kane and A P Willis. External-cavity diode lasers with different devices and collimating optics. *Appl. Opt.*, 34(21):4316–4325, 1995.

[30] M de Labachelerie and G Passedat. Mode-hop suppression of Littrow grating-tuned lasers. *Appl. Opt.*, 32(3):269–274, 1993.

[31] T P Dinneen, C D Wallace, and P L Gould. Narrow linewidth, highly stable, tunable diode laser system. *Opt. Comm.*, 92:277–282, 1992.

[32] K L Corwin, Z T Lu, C F Hand, R J Epstein, and C E Wieman. Frequency-stabilised diode laser with the zeeman shift in an atomic vapour. *Appl. Opt.*, 37(15):3295–3298, 1998.

[33] U Schünemann, H Engler, R Grimm, M Weidemüller, and M Zeilonkowski. Simple scheme for tunable frequency offset locking of two lasers. *Rev. Sci. Instrum.*, 70(1):242–243, 1999.

[34] V S Letokhov and B D Pavlik. Nonlinear absorption of separated light beams in a Doppler-broadened transition. II Strong field. *Opt. and Spectrosc.*, 32(6):573–575, 1972.

[35] M Baba. Observation of saturated absorption of methane at 3.39 $\mu$min two spatially-separated antiparallel traveling wave beams. *Jap. J. Appl. Phys.*, 20(12):2425–2426, 1981.

[36] M Baba and K Shimoda. Observation of ramsey resonance absorption in three separated laser fields produced by a corner reflector. *Appl. Phys.*, 24:11–12, 1981.

[37] W D Phillips and D Pritchard. Velocity selection by doppler shift: A general method for studying exicted-state collisions. *Phys. Rev. Lett.*, 33(21):1254–1257, 1974.

[38] W D Phillips, J A Serri, D J Ely, D E Pritchard, K R Way, and J L Kinsey. Angular scattering by doppler spectroscopy: $Na(3P_{\frac{1}{2}})$ + Ar $\rightarrow$ $Na(3P_{\frac{3}{2}})$+ Ar. *Phys. Rev. Lett.*, 41(14):937–940, 1978.

[39] S Nakayama, G W Series, and W Gawlik. Larmor precession in polarization spectroscopy with spatially separated beams. *Opt. Comm.*, 34(3):389–392, 1980.

[40] Y Wang, C Ye, X Wang, S Zhou, Y Cheng, L Ma, and L Ding. Observation of collimated atoms by light pressure force in absorption cell. *Chin. Phys. Lett.*, 10(4):213–216, 1993.

[41] J Skalla and G Wäckerle. Ramsey-type spectroscopy of alkali spin coherence in sealed glass cells: measurement of geometric quantum phases. *Appl. Phys. B*, 64:459–464, 1997.

[42] A N Nesmeyanov. *Vapour pressure of the elements.* Infosearch, London, 1996.

[43] J Emsley. *The elements.* Oxford University Press, New York, 1989.

[44] P M Farrell and W R MacGillivray. On the consistency of Rabi fredquency calculations. *J. Phys. A*, 28:209–221, 1995.

[45] Editor: R C Weist. *CRC Handbook of chemistry and physics.* CRC Press, Florida, 62nd edition, 1981-82.

[46] M R Walkiewicz. PhD Thesis, Manipulation of atoms using laser light. Universitiy of Melbourne, 2000.

[47] P W Milonni and J H Eberly. *Lasers*. John Wiley and Sons, New York, 1988.

[48] W Happer. Optical pumping. *Rev. Mod. Phys.*, 44(2):169–249, 1972.

[49] W Hanle. *Z. Physik.*, 30:93, 1924.

[50] A Kastler. *Phys. Rad.*, 11:255, 1950.

[51] J Brossel, A Kastler, and J Winter. *Phys. Rad.*, 13:984, 1952.

[52] H G Dehmelt. Slow spin relaxation of optically polarised sodium atoms. *Phys. Rev.*, 105:1487–1489, 1957.

[53] H G Dehmelt. Modulation of a light beam by precessing absorbing atoms. *Phys. Rev.*, 105:1924–1925, 1957.

[54] D Suter. *The physics of laser-atom interactions*. Cambridge University Press, Cambridge, 1997.

[55] A Corney and G W Series. Theory of resonance fluorescence excited by modulated or pulsed light. *Proc. Phys. Soc.*, 83:207–212, 1964.

[56] A Corney and G W Series. Double resonance excited by modulated light. *Proc. Phys. Soc.*, 83:213–216, 1964.

[57] A L Bloom. Principles of operation of the rubidium magnetometer. *Appl. Opt.*, 1:61–68, 1962.

[58] J Dupont-Roc, S Haroche, and C Cohen-Tannoudji. Detection of very weak magnetic fields ($10_{-9}$ Gauss) by [87]Rb zero-field level crossing resonances. *Phys. Lett.*, 28:638–639, 1969.

[59] G Wäckerle, St. Appelt, and M Mehring. Two-dimensional optical spectroscopy by periodic excitation of sublevel coherence with sub-Doppler resolution. *Phys. Rev. A*, 43(1):242–250, 1991.

[60] P Hannaford. Oriented atoms in weak magnetic fields. *Physica Scripta.*, pages 117–137, 1997.

[61] R Schieder and H Walther. Optical pumping experiments using a cw dye laser with a narrow spectral output. *Z. Physik.*, 270:55–58, 1974.

[62] G Théobald, V Giordano, N Dimarcq, and P Cérez. Observation of narrow Ramsey-type resonances in a caesium beam due to zeeman coherences. *J. Phys. B*, 24:2957–2966, 1991.

[63] B Schuh, S I Kanorsly, A Weis, and T W Hänsch. Observation of Ramsey fringes in nonlinear Faraday rotation. *Opt. Comm.*, 100(5):451–455, 1993.

[64] M Zielonkowski, J Steiger, U Schünemann, M DeKieviet, and R Grimm. Optically induced spin precession and echo in an atomic beam. *Phys. Rev. A*, 58(5):3993–3998, 1998.

[65] P M Farrell. Private communication.

[66] D J Wineland and H Dehmelt. Proposed $10^{14}$ $\delta\nu < \nu$ laser fluorescence spectroscopy on Tl$^+$ mono-ion oscillator iii. *Bull. Am. Phys. Soc.*, 20:637, 1975.

[67] T W Hänsch and A L Schawlow. Cooling of gases by laser radiation. *Opt. Comm.*, 13:68, 1975.

[68] D J Wineland, R E Drullinger, and F L Walls. Radiation-pressure cooling of bound resonators. *Phys. Rev. Lett.*, 40(25):1639–1642, 1978.

[69] W D Phillips and H Metcalf. Laser deceleration of an atomic beam. *Phys. Rev. Lett.*, 48(9):596–599, 1982.

[70] J V Prodan, W D Phillips, and H Metcalf. Laser production of a very slow monoenergetic atomic beam. *Phys. Rev. Lett.*, 49(16):1149–1153, 1982.

[71] W Ertmer, R Blatt, J L Hall, and M Zhu. Laser manipulation of atomic beam velocities: Demonstration of stopped atoms and velocity reversal. *Phys. Rev. Lett.*, 54(10):996–999, 1985.

[72] J Prodan, A Migdall, W D Phillips, I So, H Metcalf, and J Dalibard. Stopping atoms with laser light. *Phys. Rev. Lett.*, 54(10):992–995, 1985.

[73] S Chu, L Hollberg, J E Bjorkholm, A Cable, and A Ashkin. Three-dimensional viscous confinement and cooling of atoms by resonance radiation pressure. *Phys. Rev. Lett.*, 55(1):48–51, 1985.

[74] E L Raab, M Prentiss, A Cable, S Chu, and D E Pritchard. Trapping of neutral sodium atoms with radiation pressure. *Phys. Rev. Lett.*, 59(23):2631–2634, 1987.

[75] P D Lett, W D Phillips, S L Rolston, C E Tanner, R N Watts, and C I Westbrook. Optical molasses. *J. Opt. Soc. Am. B*, 6(11):2084, 1989.

[76] J Dalibard and C Cohen-Tannoudji. Laser cooling below the Doppler limit by polarisation gradients: simple theoretical models. *J. Opt. Soc. Am. B*, 6:2023, 1989.

[77] C Salomon, J Dalibard, A Aspect, H Metcalf, and C Cohen-Tannoudji. Channelling atoms in a laser standing wave. *Phys. Rev. Lett.*, 59(15):1659–1662, 1987.

[78] A Aspect, E Arimondo, R Kaiser, and C Cohen-Tannoudji. Laser cooling below the one-photon recoil energy by velocity-selective coherent population trapping. *Phys. Rev. Lett.*, 61(7):826–829, 1986.

[79] A Aspect, J Dalibard, A Heidmenn, C Salomon, and C Cohen-Tannoudji. Cooling atoms with stimulated emission. *Phys. Rev. Lett.*, 57(14):1688–1691, 1988.

[80] A J Kerman, V Vuletic, and C Chin amd S Chu. Beyond optical molasses: 3D Raman sideband cooling to high phase-space density. *Phys. Rev. Lett.*, 84(3):439–442, 2000.

[81] V I Balykin and V S Letokhov. *Atom optics with laser light - Laser Science and Technology series*, volume 18. Harwood, Switzerland, 1995.

[82] C J Foot. Laser cooling and trapping of atoms. *Contemp. Phys.*, 32(6):369–381, 1991.

[83] C Cohen-Tannoudji and W D Phillips. New mechanisms for laser cooling. *Phys. Today*, 43:33–40, 1990.

[84] J J McClelland, R E Scholten, E C Palm, and R J Celotta. Laser-focussed atomic deposition. *Science*, 262:877, 1993.

[85] C S Adams, M Sigel, and J Mlynek. Atom optics. *Phys. Rep.*, 240:143–210, 1994.

[86] V I Balukin and V S Letokhov. Laser optics of neutral atomic beams. *Phys. Today*, 42:23–28, 1989.

[87] R E Scholten, R Gupta, J J McClelland, R J Celotta, M S Levenson, and M G Vangel. Laser collimation of a chromium beam. *Phys. Rev. A*, 55(2):1331–1338, 1997.

[88] D Milic, M D Hoogerland, K G H Baldwin, and R E Scholten. Transverse laser cooling of a velocity-selected sodium atomic beam. *Quantum Semiclass. Opt.*, 8:629–640, 1996.

[89] M R Williams, M J Bellanca, L Liu, C Xie, W F Buell, T H Bergeman, and H J Metcalf. Atom cooling in one dimension with high-intensity laser light. *Phys. Rev. A*, 57(1):401–411, 1998.

[90] C Monroe, W Swann, H Robinson, and C Wieman. Very cold trapped atoms in a vapour cell. *Phys. Rev. Lett.*, 65(13):1571–1574, 1990.

[91] C S Adams and E Riis. Laser cooling and trapping of neutral atoms. *Prog. Quant. Electr.*, 21:1–79, 1997.

[92] H Metcalf and P van der Straten. Cooling and trapping of neutral atoms. *Phys. Rep.*, 244:203–286, 1994.

[93] P S Jessen, C Gerz, P D Lett, W D Phillips, S L Rolston, R J C Spreeuw, and C I Westbrook. Observation of quantized motion of Rb atoms in an optical field. *Phys. Rev. Lett.*, 69(1):49–52, 1992.

[94] G Baum, C D Caldwell, and W Schroeder. Dual-frequency optical pumping for spin-polarising a lithium atomic beam. *Appl. Phys.*, 21(2):121–126, 1980.

[95] V G Minogin and O T Serimaa. Resonant light pressure forces in a strong standing laser wave. *Opt. Comm.*, 30(3):373–379, 1979.

[96] Q Li, K G H Baldwin, H A Bachor, and D E McClelland. Variable focal-length lens for atoms. *J. Opt. Soc. Am. B*, 13(2).

[97] PV Wave version 6.21. Visual Numerics, Inc., 1998.

[98] M D Hoogerland. Private communication.

# Appendix A

## TEMPERATURE CONTROL CIRCUIT

A diagram of the circuit built to stabilise the temperature of the external cavity laser diode is given in figure A.1 over the page. This circuit is essentially just a power amplifier which drives Thermoelectric coolers (TECs) with a current proportional to the difference between a set and measured temperature.

An AD590 (situated in the laser mount) senses the temperature and produces a voltage proportional to it. This is then compared with the set point voltage (selected by a 10 kΩ potentiometer). Temperatures in the range of 0-50°Cmay be set. The difference of the two signals is sent to the gate of the two Darlington transistors which drive the cooling and heating of the Peltier devices (TECs). A rectified 20 A / 24 V transformer provides ample current to drive the Peltiers. On the other side of the TECs are high Wattage sense resistors and the voltage across these is fed back to the set/actual temperature comparitor.

There are two Light emitting diodes (LEDs) which indicate whether the actual temperature of the laser is below or above the set point. Both the set point and actual temperatures can be displayed on a 200 mV digital meter.
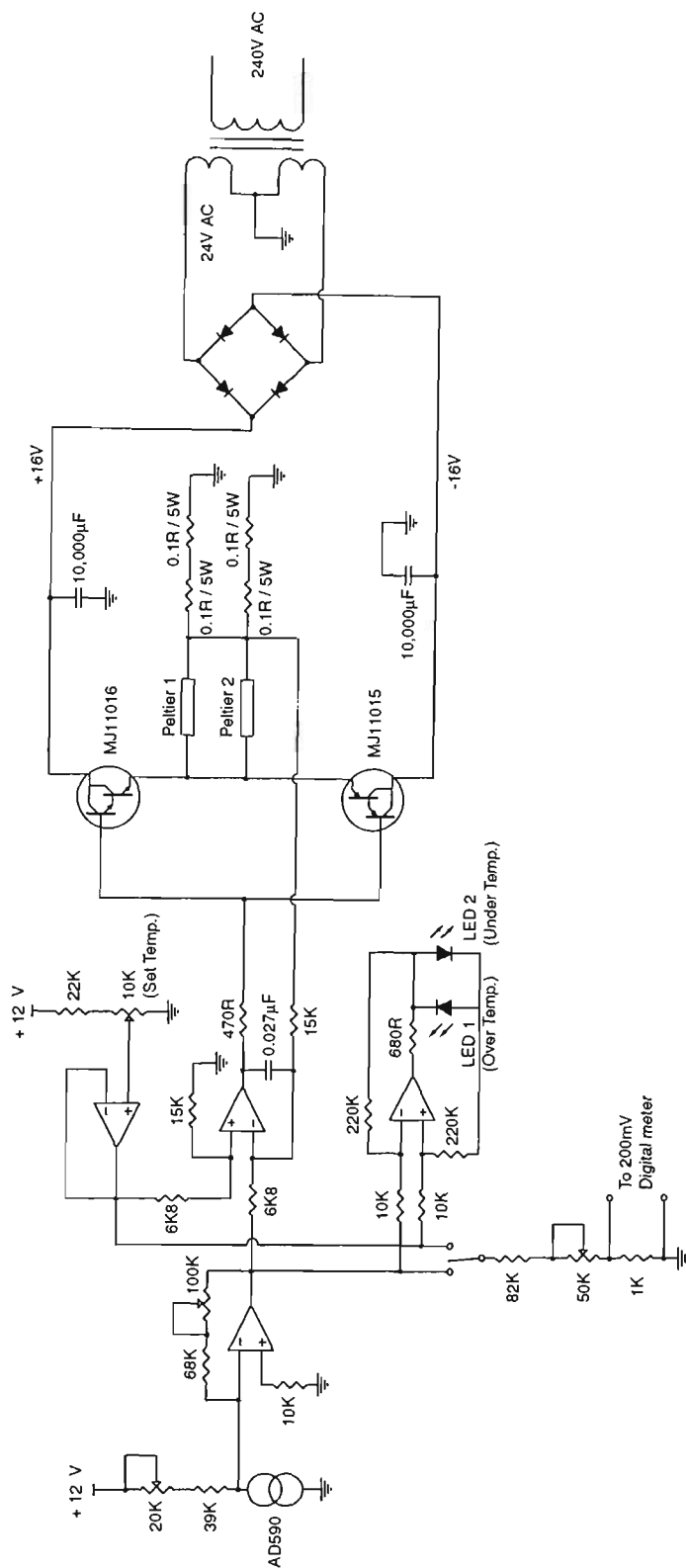
**Figure A.1**: Schematic of the ECLD temperature control circuit. Resistances are given in ohms. Operational amplifiers are all TL074 (or equivalent).

# Appendix B
## LASER LOCKING CIRCUIT

A diagram of the circuit built to lock the frequency of the external cavity laser diode to an atomic transition is given in figure B.1 over the page. This circuit allows for both the Zeeman and AC locking techniques to be implemented.

The circuit can be broken up into two arms which drive the fast and slow response wavelength selective elements of the laser. The gains of each stage can be adjusted independently and integration is only performed on the slow stage. The fast stage is AC coupled (by the $0.6\,\mu$F capacitor so that no large DC voltages are sent to the fast elements.

When the scan/lock switch is in the scan position the integrator is turned off (by connecting two $100\,\Omega$ resistors across the $1\,\mu$F capacitor), feedback to both the fast and slow stages are disconnected and the output of the slow gain stage is connected to a ramp signal. When the lock switch is on the feedback to both arms is connected and the $100\,\Omega$ resistors are removed to turn on the integration. It was important to zero the offset of the integrator by the balance adjustment to prevent large voltages building up on the integrator output. The polarity of the slow stage can be switched with respect to the fast stage to allow for different laser configurations.

When Zeeman locking is used the feedback is derived simply from the difference of the two photodiode signals (PD+ and PD-). No external modulation is applied to the circuit. The voltage taken from the referenced $\pm 6.95$ V supply is used to adjust the offset of the dispersion signal and hence the locking point of the laser.

AC locking requires a small modulation to be applied (via the mod. in connection) to the laser frequency so that the lock-in amplifier can produce a dispersion curve. Typically, the laser was modulated by a 24 kHz sine wave (24 kHz was chosen to avoid resonances in the PZT disc). This also limits the bandwidth of the lock to below 24 kHz.

144
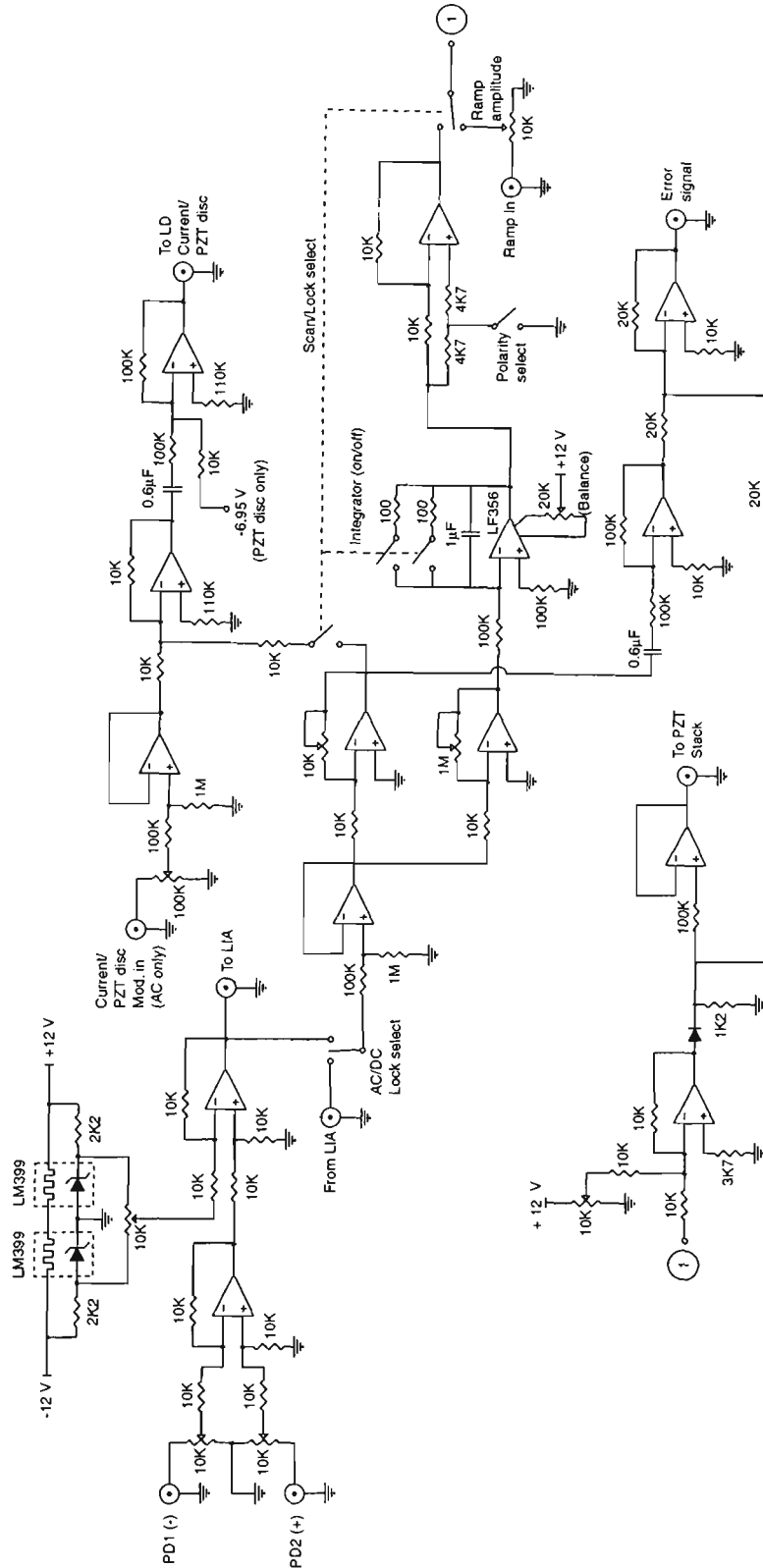
**Figure B.1**: Schematic of the ECLD locking circuit. Resistances are given in ohms. Operational amplifiers are TL074 (or equivalent) unless otherwise stated.

# Appendix C

# TIME EVOLUTION OF A $J = \frac{1}{2}$ STATE IN A MAGNETIC FIELD

Consider the system shown in figure C.1 below. This is a simplified version of our excitation and detection scheme for the Larmor experiment in which the $(\sigma^+)$ chopped laser pumps atoms into the $m_J = \frac{+1}{2}$ state of the $J = \frac{1}{2}$ ground state via the excitations shown to the $J = \frac{3}{2}$ excited state. The probe laser (also $\sigma^+$) is tuned to $J = \frac{1}{2}$ excited state so can only excite atoms from the $m_J = -\frac{1}{2}$ ground state sublevel.
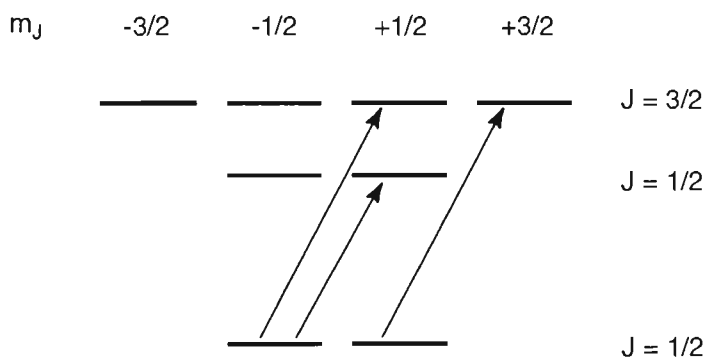


**Figure C.1**: Energy levels of the $J = \frac{1}{2}$ to $J = \frac{1}{2}$ and $J = \frac{3}{2}$ (s → p) system and the allowed transitions for $\sigma^+$ light.

We first assume that the chopped laser prepares all atoms into the $m_J = +\frac{1}{2}$ ground state. The atoms then travel between the two lasers under the influence of a magnetic field oriented along the $x$-direction. In the absence of any light, the Hamiltonian, $H_{\text{total}}$, for the atoms is given by,

$$H_{\text{total}} = H_{\text{atom}} + H_{\text{interaction}} \tag{C.1}$$

where $H_{\text{interaction}} = g_j \mu_B B J_x$, $g_j$ is the Landé factor, $\mu_B$ is the Bohr magneton, $B$ is the magnitude of the field and $J_x = \frac{1}{2} \begin{pmatrix} 0 & 1 \\ 1 & 0 \end{pmatrix}$ is the spin operator about $x$. Writing this out we have,

$$H_{\text{total}} = \hbar\omega_0 \begin{pmatrix} 1 & 0 \\ 0 & 1 \end{pmatrix} + g_j \mu_B B \frac{1}{2} \begin{pmatrix} 0 & 1 \\ 1 & 0 \end{pmatrix} \tag{C.2}$$

where $\omega_0$ is the resonance frequency of the atom. To determine the time evolution

of this system we use the Liouville equation,

$$i\hbar\dot{\rho} = [H_{\text{total}}, \rho] \tag{C.3}$$

where $\rho$ is the density matrix of the atom. The atomic part of the Hamiltonian, $H_{\text{atom}}$ is proportional to an identity matrix so this will commute with any $2 \times 2$ matrix. Thus C.3 reduces to,

$$i\hbar\dot{\rho} = [H_{\text{interaction}}, \rho] \tag{C.4}$$

Writing this in full we have,

$$i\hbar \begin{pmatrix} \dot{\rho}_{\frac{1}{2}\frac{1}{2}} & \dot{\rho}_{\frac{1}{2}-\frac{1}{2}} \\ \dot{\rho}_{-\frac{1}{2}\frac{1}{2}} & \dot{\rho}_{-\frac{1}{2}-\frac{1}{2}} \end{pmatrix} = \omega_{\text{L}} \frac{\hbar}{2} \left[ \begin{pmatrix} 0 & 1 \\ 1 & 0 \end{pmatrix} \begin{pmatrix} \rho_{\frac{1}{2}\frac{1}{2}} & \rho_{\frac{1}{2}-\frac{1}{2}} \\ \rho_{-\frac{1}{2}\frac{1}{2}} & \rho_{-\frac{1}{2}-\frac{1}{2}} \end{pmatrix} - \begin{pmatrix} \rho_{\frac{1}{2}\frac{1}{2}} & \rho_{\frac{1}{2}-\frac{1}{2}} \\ \rho_{-\frac{1}{2}\frac{1}{2}} & \rho_{-\frac{1}{2}-\frac{1}{2}} \end{pmatrix} \begin{pmatrix} 0 & 1 \\ 1 & 0 \end{pmatrix} \right] \tag{C.5}$$

where we have made the substitution, $\omega_{\text{L}} = \frac{g_j \mu_{\text{B}} B}{\hbar}$ (the Larmor frequency). Equation C.5 yields the following four differential equations.

$$\dot{\rho}_{\frac{1}{2}\frac{1}{2}} = \frac{i\omega_{\text{L}}}{2} \left( \rho_{\frac{1}{2}-\frac{1}{2}} - \rho_{-\frac{1}{2}\frac{1}{2}} \right) \tag{C.6}$$

$$\dot{\rho}_{\frac{1}{2}-\frac{1}{2}} = \frac{i\omega_{\text{L}}}{2} \left( \rho_{\frac{1}{2}\frac{1}{2}} - \rho_{-\frac{1}{2}-\frac{1}{2}} \right) \tag{C.7}$$

$$\dot{\rho}_{-\frac{1}{2}\frac{1}{2}} = \frac{i\omega_{\text{L}}}{2} \left( \rho_{-\frac{1}{2}-\frac{1}{2}} - \rho_{\frac{1}{2}\frac{1}{2}} \right) \tag{C.8}$$

$$\dot{\rho}_{-\frac{1}{2}-\frac{1}{2}} = \frac{i\omega_{\text{L}}}{2} \left( \rho_{-\frac{1}{2}\frac{1}{2}} - \rho_{\frac{1}{2}-\frac{1}{2}} \right) \tag{C.9}$$

Since $\rho$ is Hermitian and normalised we have $\rho_{\frac{1}{2}\frac{1}{2}} + \rho_{-\frac{1}{2}-\frac{1}{2}} = 1$, $\rho_{-\frac{1}{2}\frac{1}{2}} = \rho^*_{\frac{1}{2}-\frac{1}{2}} = u + iv$ (where $u + iv$ is an arbitrary complex number) and $\rho_{-\frac{1}{2}-\frac{1}{2}} = r$ (a real quantity). Substituting $\rho_{\frac{1}{2}\frac{1}{2}} = 1 - \rho_{-\frac{1}{2}-\frac{1}{2}}$ into C.7 we have,

$$\dot{\rho}_{\frac{1}{2}-\frac{1}{2}} = \dot{u} + i\dot{v} = i\frac{\omega_{\text{L}}}{2}(1 - 2r) \tag{C.10}$$

From this $\dot{u}$ must be zero and $u(0) = 0$ so $u = 0$. Thus C.10 becomes,

$$\dot{v} = \frac{\omega_{\text{L}}}{2}(1 - 2r) \tag{C.11}$$

Also, C.9 can be expressed in terms of $r$, $u$ and $v$ yielding

$$\dot{r} = \frac{i\omega_{\text{L}}}{2}(u - iv - u - iv)) = \omega_{\text{L}}v \tag{C.12}$$

Combining these gives the following differential equation for $r$,

$$\ddot{r} = \frac{\omega_{\text{L}}^2}{2}(1 - 2r) \tag{C.13}$$

It is easily shown that a solution to this is,

$$r(t) = \frac{1}{2} - \frac{1}{2}(\cos\omega_\mathrm{L} t) \qquad (\mathrm{C}.14)$$

where we have included our initial assumption that all atoms start in the $m_\mathrm{J} = +\frac{1}{2}$ state (i.e. $r(0) = 0$). This function starts at zero and cycles between zero and one following a cosine which oscillates at the Larmor frequency. We introduced $r$ as the real density matrix element $\rho_{-\frac{1}{2}-\frac{1}{2}}$ which tells us the population in the $m_\mathrm{J} = -\frac{1}{2}$ substate of the $J = \frac{1}{2}$ ground state. In the low excitation limit, the probe laser absorption will be proportional to the number of atoms in this state. This demonstrates (for the simple case of a $J = \frac{1}{2}$ ground state) how the cosine dependent absorption arises.

# Appendix D

## COMPUTER PROGRAM

This is the PV Wave code written to calculate the expected number of atoms in the vapour cell atomic beam as a function of cooling laser intensity and detuning. The laser parameters and atom ensemble have been chosen to best match the experimental conditions.

```
;This program calculates the expected lock-in signal ;detected in
the VCAB as a ;function of the cooling laser parameters for lasers
with gaussian ;profiles

;Main program

PRO BIABally, power, filename

    totalsignal = fltarr(7,41)    ;Array to hold the calculated signals
    totalsignal(*,*) = 0          ;Initialise this to zero
    signal = fltarr(41)           ;Array for temporary signal storage
    detMHz = findgen(41)          ;Array to hold the detunings
    detMHz = detMHz - 20          ;-20 to +20 MHz
    pi = 3.14159


                        ;These multiplicative constants (peak laser
                        ;intensitites) were calculated using Maple V

    Gocl = power * 9.6      ;Cooling laser peak intensity
    Goch = 0.046 * 121.9    ;Chopped laser peak intensity
    Gopr = 0.034 * 149.6    ;Probe laser peak intensity


    clyoffset = 0.0         ;Cooling laser y offset

    xradcl = 2.6        ;Radii of the laser beams in mm
    yradcl = 1.2
    radch = 1.08 / 2
    radpr = 0.975 / 2


                        ;Create x and y arrays between -1 and 1
    x = findgen( 101 )
    x = ( x - 50 ) / 50
    y = findgen( 101 )
    y = ( y - 50 ) / 50

                        ;x positions of each of the lasers in mm
    offsetcl = -12.4
    offsetch = -4.1
```

```
offsetpr = 0


                          ;x and y range of the gaussians for the lasers
                          ;+/- 2 1/e radii

xcl = 2 * xradcl * x + offsetcl
ycl = 2 * yradcl * y + clyoffset
ych = 2 * radch * y
xch = ych + offsetch
ypr = 2 * radpr * y
xpr = ypr + offsetpr


                          ;Calculate the gaussians over these ranges

gausscl = gauss1d( yradcl, ycl, Gocl, clyoffset )
gaussch = gauss1d( radch, ych, Goch, 0 )
gausspr = gauss1d( radpr, ypr, Gopr, 0 )


                              ;Create an array of angles

angles = findgen( 41 )
angles = ( angles - 20 ) * pi / 180      ;Convert to radians

                      ;These nested loops calculate the expected
                      ;signals for  different laser detunings
                      ;for trajectories with a range of angles
                      ;passing through at a range of y-heights

FOR d = 1,41 DO BEGIN    ;Loop over detunings (-20MHz to +20MHz)

   FOR i = 21,51,10 DO BEGIN     ;Loop over the different y positions

      signal = 0

      FOR a = 15,27,2 DO BEGIN    ;Loop over the different angles

                          ;Calculate the y-position of the atom
                          ;at the cooling and chopped lasers

         yatcool = -offsetcl * TAN(angles(a-1)) + ypr(i-1)
         yatchop = -offsetch * TAN(angles(a-1)) + ypr(i-1)


                          ;Find the intensity of the cooling laser
                          ;for the atom trajectory

         Gatcool = Gocl * EXP( -2 * (yatcool - clyoffset)^2 / yradcl^2 )


                          ;Find the weighting factors (absorption
                          ;in the chopped and probe lasers)
```

```
      chopweight = EXP( -2 * yatchop^2 / radch^2 )

      chopabs = 3.3 * ( EXP( -2 * yatchop^2 / radch^2 ) ) / ( 2 *
               ( 3.3 * EXP( -2 * yatchop^2 / radch^2 ) + 1 ) )

      chopS = chopweight * 3.3

      probeabs = 2.9 * EXP( -2 * (ypr(i-1))^2 / radpr^2 ) / ( 2 *
               ( 2.9 * EXP( -2 * (ypr(i-1))^2 / radpr^2 ) + 1 ) )


                              ;Calculate the contribution to
                              ;the total signal

      signal = signal + ( probeabs * chopabs * ( 1 +
               chopexc(detMHz(d-1), Gatcool, chopS ) ) )

    ENDFOR

                              ;The contribution of atoms passing
                              ;through the probe at a certain height

      totalsignal( (i-21)/10, d-1 ) = signal
      totalsignal( 6 - (i-21)/10, d-1 ) = signal

    ENDFOR

  ENDFOR


                              ;Add these contributions to the total signal

  totalarr = SUM( totalsignal, 0 )

  plot, detMHz, totalarr, psym = 4      ;Plot the signal vs. detuning

  OPENW, theor, filename, /get_lun      ;Write the data to a file
  printf, theor, totalarr
  free_lun, theor

  STOP
END                             ;End main program


;The rest of the program contains the functions used by the main
;program

;This function calculates and returns a 1D gaussian

FUNCTION gauss1d, yrad, y, Go, offset
   gauss = Go * exp( -2 * (y-offset)^2 / yrad^2 )
   RETURN, gauss
END
```

```
;This function calculates a gaussian in terms of angles relative
;to a y position on the probe laser axis

FUNCTION findangles, xoffset, rad, angles, yoffset, offset2
    y = xoffset * tan( angles ) - yoffset
    gss = exp( -2 * (y-offset2)^2 / rad^2 )
    RETURN, gss
END



;Calculate the detected velocity distributions after cooling

FUNCTION chopexc, detunMHz, Go, chopS
    vinit = findgen( 2001 )              ;Array of initial velocities
    vinit = ( vinit - 1000 ) / 20
    v = cooledv( detunMHz, Go, vinit )   ;Calculate cooled vel. distribution
    Nofv = fltarr(2001)
    Nofv(*) = 0
    Nofvinit = doppler( vinit )          ;Initial (Doppler) vel. distribution
    v = v * 20 + 1000
                                ;Bin the atoms into buckets 0.05 m/s wide
    FOR i = 1,2001 DO BEGIN
       IF (v(i-1) LE 2000) AND (v(i-1) GE 0) THEN BEGIN
          Nofv( FIX(v(i-1)) ) = Nofv( FIX(v(i-1)) ) + 1
       ENDIF
    ENDFOR

    Nofv = Nofv * doppler( vinit )       ;Doppler weight the binned distribution
    detvgrp = findvgrp( chopS )          ;What atoms do we detect?
    cooledsum = manualconv( Nofv, chopvgrp, vinit )   ;Convolute this with the
                                    ;weighted and binned distribution to find
                                    ;the number of excited atoms
    uncooledsum = manualconv( Nofvinit, detvgrp, vinit )
    difference = cooledsum - uncooledsum
    RETURN, difference / uncooledsum     ;Normalise the result
END



;Calculates the number of atoms as a function of v in a room temp
;Doppler distribution of rubidium for a given velocity range

FUNCTION doppler, v
    pi = 3.141592
    k = 2 * pi / 780e-9
    Nofv = exp( - ( k * v )^2 / ( 0.36 * ( 2 * pi * 505e6 )^2 ) )
    RETURN, Nofv
END



;Manually convolute and sum the elements of the detected velocity
;group array with the velocity distribution of the atoms

FUNCTION manualconv, Nofv, vgrp, v
    sum = 0
    FOR i = 1, 2001 DO BEGIN
```

```
         sum = sum + ( Nofv(i-1) * vgrp(i-1) )
    ENDFOR
    RETURN, sum
END


;Calculate the velocity group of atoms excited by a laser

FUNCTION findvgrp, S
    pi = 3.141592
    k = 2 * pi / 780e-9
    gamma = pi * 6e6
    vel = findgen( 2001 )
    vel = ( vel - 1000 ) / 20
    vgrp = 1 / ( ( k * vel )^2 + ( ( gamma )^2 * ( 1 + S ) ) )
    RETURN, vgrp
END


;Calculate the velocity of atoms after they pass through the
;cooling laser

FUNCTION cooledv, detunMHz, Go, vinit
    bmamount = 1.5
    maxt = 0.0052 * bmamount / 270    ;Time = distance/vel. (for 1.5*1/e^2 radii)
    t = 0
    dt = 2e-7                         ;Time interval in seconds
    m = 87 * 1.674e-27                ;Mass of 87Rb
    v = vinit
    WHILE (t LT maxt) DO BEGIN            ;For the time the atom is in the beam...
;        print, 'Time is ',t
        G = Go * exp( -2 * (t-maxt/2)^2 / (maxt/(2*bmamount))^2 )
        F = force( detunMHz, G, v )      ;Find the force
        F = FLOAT( F )                ;Ensure it is a real number
        dv = dt * F / m              ;Calculate the change in v
        v = v + dv                   ;Adjust the velocity
        t = t + dt                   ;Increment the time
    ENDWHILE
    RETURN, v
END


;Calculate the force given the cooling laser parameters

FUNCTION force, detunMHz, G, v
    pi = 3.141592
    hbar = 1.055e-34                 ;Planck's constant / 2 pi
    k = 2 * pi / 780e-9              ;Wavenumber
    gamma = pi * 6e6                 ;Gamma / 2
    detun = 2e6 * pi * detunMHz      ;Convert detuning into rad/s
    A = detun / complex ( gamma, k * v )
    Q = findQ( detun, G, v )
    A = A * Q
    REALQ = Q - complex ( 0, IMAGINARY ( Q ) )
    F  = -2 * hbar * k * gamma * IMAGINARY( A ) / ( 1 + 2 * REALQ )
```

```
    RETURN, F
END


;Calculate the continued fraction part of the force

FUNCTION findQ, detun, G, v
    pi = 3.141592
    k = 2 * pi / 780e-9
    gamma = pi * 6e6
    Q = complex ( 0, 0 )

    FOR n = 50,0,-1 DO BEGIN      ;Calculate to the 50th term in the
                                  ;continued fraction

        IF (n) THEN BEGIN         ;If n is odd then ...
            n1 = n
            n2 = n + 1
        ENDIF ELSE BEGIN          ;Otherwise, n is even ...
            n1 = n + 1
            n2 = n
        ENDELSE

        p = G * 2 * gamma^2 * complex ( gamma, n1 * k * v )
        p = p /   complex ( 2 * gamma, n2 * k * v )
        p = p / ( detun^2 + ( complex ( gamma, n1 * k * v ) )^2 )
        Q = p / ( 1 + Q )
    ENDFOR

    RETURN, Q
END
```